Multi-day Thermochemical Energy Storage

by

Rhushikesh Ghotkar

A Dissertation Presented in Partial Fulfillment
of the Requirements for the Degree
Doctor of Philosophy

Approved October 2023 by the
Graduate Supervisory Committee:

Ryan Milcarek, Chair
Ivan Ermanoski
Patrick Phelan
Liping Wang
Robert Wang

ARIZONA STATE UNIVERSITY
December 2023

ABSTRACT

Energy storage technologies are essential to overcome the temporal variability in renewable energy. The primary aim of this thesis is to develop reactor solutions to better analyze the potential of thermochemical energy storage (TCES) using non-stoichiometric metal oxides, for the multi-day energy storage application. A TCES system consists of a reduction reactor and an insulated MO_x storage bin. The reduction reactor heats (to ~ 1100 °C) and partially reduces the MO_x, thereby adding sensible and chemical energy (i.e., charging it) under reduced pO_2 environments (~10 Pa). Inert gas removes the oxygen generated during reduction. The storage bin holds the hot and partially reduced MO_x (typically particles) until it is used in an energy recovery device (i.e., discharge). Irrespective of the reactor heat source (here electrical), or the particle-inert gas flows (here countercurrent), the thermal reduction temperature and inert gas (here N_2) flow minimize when the process approaches reversibility, i.e., operates near equilibrium. This study specifically focuses on developing a reduction reactor based on the theoretical considerations for approaching reversibility along the reaction path. The proposed Zigzag flow reactor (ZFR) is capable of thermally reducing CAM28 particles at temperatures ~ 1000 °C under an O_2 partial pressure ~ 10 Pa. The associated analytical and numerical models analyze the reaction equilibrium under a real (discrete) reaction path and the mass transfer kinetic conditions necessary to approach equilibrium. The discrete equilibrium model minimizes the exergy destroyed in a practical reactor and identifies methods of maximizing the energy storage density (Ω) and the exergetic efficiency. The mass transfer model analyzes the O_2-N_2 concentration boundary layers to recommend sizing considerations to maximize the reactor power density. Two functional ZFR prototypes, the α-ZFR and the β-ZFR, establish the proof of concept and achieved a reduction extent, $\Delta\delta = 0.071$ with CAM28 at T~950 °C and $pO_2 = 10$ Pa, 7x higher than a previous attempt in the literature. The α-ZFR consistently achieved $\Omega > 100$ Wh/kg during >10 h. runtime and the β-ZFR displayed an improved $\Omega = 130$ Wh/kg during >5 h. operation with CAM28. A techno-economic model of a grid-scale ZFR with an associated storage bin analyzes the cost of scaling the ZFR for grid energy storage requirements. The scaled ZFR capital costs contribute < 1% to the levelized cost of thermochemical energy storage, which ranges from 5-20 ¢/kWh depending on the storage temperature and storage duration.

DEDICATION

Dedicated to my family for their unwavering support and love throughout my academic education. No effort on my part will ever be sufficient to thank you for the sacrifices you have made on my behalf. It would have been impossible for me to achieve my dream without you and your encouragement. I would also like to thank my friends for staying by my side through all the ups and downs.

ACKNOWLEDGEMENTS

This material is based on work supported by the U.S. Department of Energy's Office of Energy Efficiency and Renewable Energy (EERE) under the Solar Energy Technologies Office. This work is part of a much bigger study titled "Economic Weekly and Seasonal Thermochemical and Chemical Energy Storage for Advanced Power Cycles," Award #DE-EE0008991. I am grateful to the members of Lightworks® and Combustion and Electrochemical Power Systems Laboratory at Arizona State University for providing all the necessary resources to successfully complete my work. I would also like to thank my committee members for their guidance in my research and for taking the time to serve on my committee.

TABLE OF CONTENTS

Page

CHAPTER

CHAPTER Page

APPENDIX

LIST OF FIGURES

Figure Page

LIST OF TABLES

Table Page

NOMENCLATURE

a_{cell}	Unit cell side
a_{mesh}	Mesh opening size
A_R	Reactor transverse cross section
C_1	Channel material mass specific cost
$C_{1,chan}$	Single channel cost
C_{MW}	Unit cost of reactor power
C_{MWh}	Unit cost of stored energy
C_T	Total Costs
d_{FS}	Full scale reactor depth
D_h	Hydraulic diameter
f_{reac}	Reactive fraction
IP	Inclined plane
k_L	Labor cost multiplier
LCOS	Levelized cost of storage
m_1	Single channel material mass
$m_{ins,1}$	Single channel insulation mass
m_{ins,N_C}	Scaled insulation mass
$\dot{m}_{MO_x}$	MO_x mass flow rate
m_{OX}	Sample mass pre-reoxidation
m_R	Sample mass post-reoxidation
MO_x	Metal oxide
N_c	Number of channels
N_p	Number of identical particles per mesh
$\dot{n}_k$	Molar flow rate of species ‘k’

n_{MO_x}	Number of moles of MO_x
OFR	Obstructed flow reactor
P_{out}	Output power
pO_2	Oxygen partial pressure
pO_{2,N_2}	pO_2 in the N_2 stream
$pO_{2,s}$	pO_2 at particle surface
t_{BL}	Boundary layer thickness
T_{OX}	Initial MO_x temperature
T_R	Final MO_x temperature
$T_{R,max}$	Maximum reduction temperature
$T_{R,out}$	Reactor output temperature
TCES	Thermochemical energy storage
vN_2	N_2 velocity
v_T	Terminal velocity
V_{part}	Available mesh volume
w_{mesh}	Mesh width
ZFR	Zigzag flow reactor
δ	Reduction extent
δ_{OX}	Initial reduction extent
δ_R	Final reduction extent
$\Delta\delta$	Change in reduction extent
Δg	Reduction Gibbs' free energy change
Δh	Thermal reduction enthalpy
Δz_{part}	Particle bed thickness
Ω	Recoverable stored energy
λ	Sweep ratio

Π	Power density
ρ_{MO_x}	Metal oxide density
ρ_{N_2}	Nitrogen density
ψ	Total exergy destroyed
τ_{N_2}	N_2 intermesh travel time
τ_{diff}	O_2 diffusion time to the nearest unit cell side
τ_R	MO_x residence time

1. INTRODUCTION

1.1. Motivation

Global investment in clean energy has increased 75% from ~\$1 Trillion in 2015 to \$1.75 Trillion in 2023 [1] (Figure 1). The recovery from the Covid-19 pandemic and the political pressure to move away from fossil fuels is responsible for this major boost in clean energy investment [2–6]. According to the International Energy Agency (IEA), the updated pathway to achieve net zero emissions (NZE) by 2050, the largest growth in energy supply must come from solar and wind sources [1]. A majority of the solar projects under construction for the second half of 2020, incorporate some form of energy storage, e.g., molten salt or thermal energy storage [7–9], to account for the temporal mismatch between the supply of renewable energy and the electricity demand [10–13].

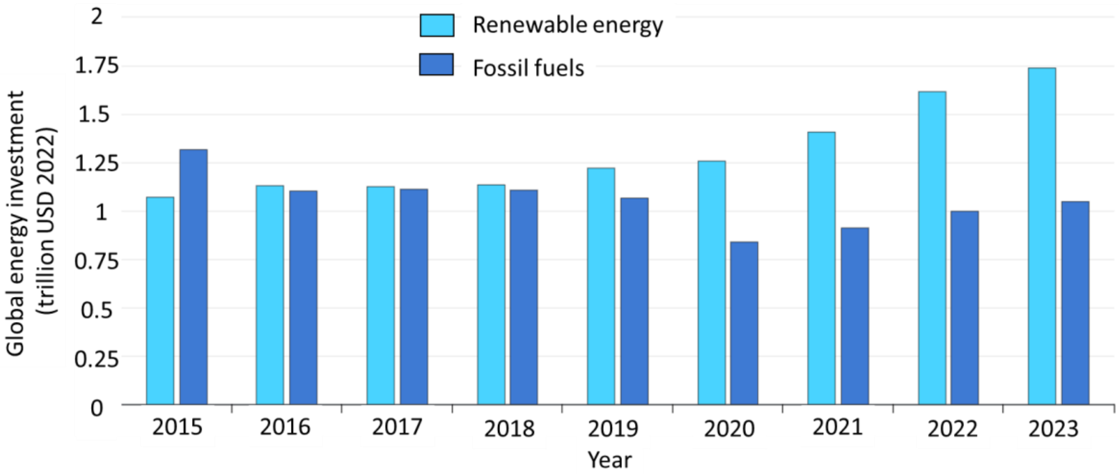

Figure 1- Year Over Year Change In the Global Energy Investment. Renewable Energy Investment Increased By 75% In the Previous 9 Years [1].

The availability of renewable energy varies throughout the day, week, and seasons of the year. This mismatch creates several challenges in managing the electrical grid and reduces reliability [14,15]. Adding avenues for storing energy when surplus is available is thus necessary for use during times of low energy availability. Li-ion batteries are economical only for low storage duration, high cycling applications [16]. Technologies that can store energy for several days and for seasonal variations will be necessary to provide reliable year-round dispatch [17,18]. Technologies that enable dispatchability in a grid that has a large penetration of intermittent renewables is well beyond the current state-of-the-art.

The levelized cost of storage (LCOS) assesses the total lifetime cost of an energy storage technology relative to the electricity it delivers [16]. LCOS enables a comprehensive comparison of ownership and operating costs for different storage assets [19–21]. In Figure 2, LCOS is presented for various energy storage technologies based on their storage duration and power capacity. These technologies include lithium-ion (Li-ion) batteries (specifically, lithium iron phosphate (LFP) [22,23] and lithium nickel manganese cobalt (NMC) variants [24,25]), lead-acid batteries [26,27], vanadium redox flow batteries (RFBs) [28,29], diabatic compressed-air energy storage (CAES) [30,31], pumped storage hydropower (PSH) [32,33], bidirectional hydrogen energy storage systems (HESS) [34,35], zinc-based batteries [36,37], gravity energy storage [38,39], and thermal energy storage [40,41]. Figure 2 reveals that as the storage duration increases, LCOS decreases until reaching a minimum at 10 h., followed by an increase at longer durations. This increase occurs because the annual discharge energy throughput is limited by the number of cycles these technologies can perform in a year, particularly at durations of 24 and 100 h. Notably, for technologies with lower LCOS, such as CAES, PSH, hydrogen, and thermal storage, the LCOS increase at longer durations is less significant compared to batteries, which have a higher unit energy cost. In the case of a 100 h. duration, where calendar life is the limiting factor, choosing lead-acid batteries with lower cycle life and capital cost is expected to lower LCOS at extended durations.

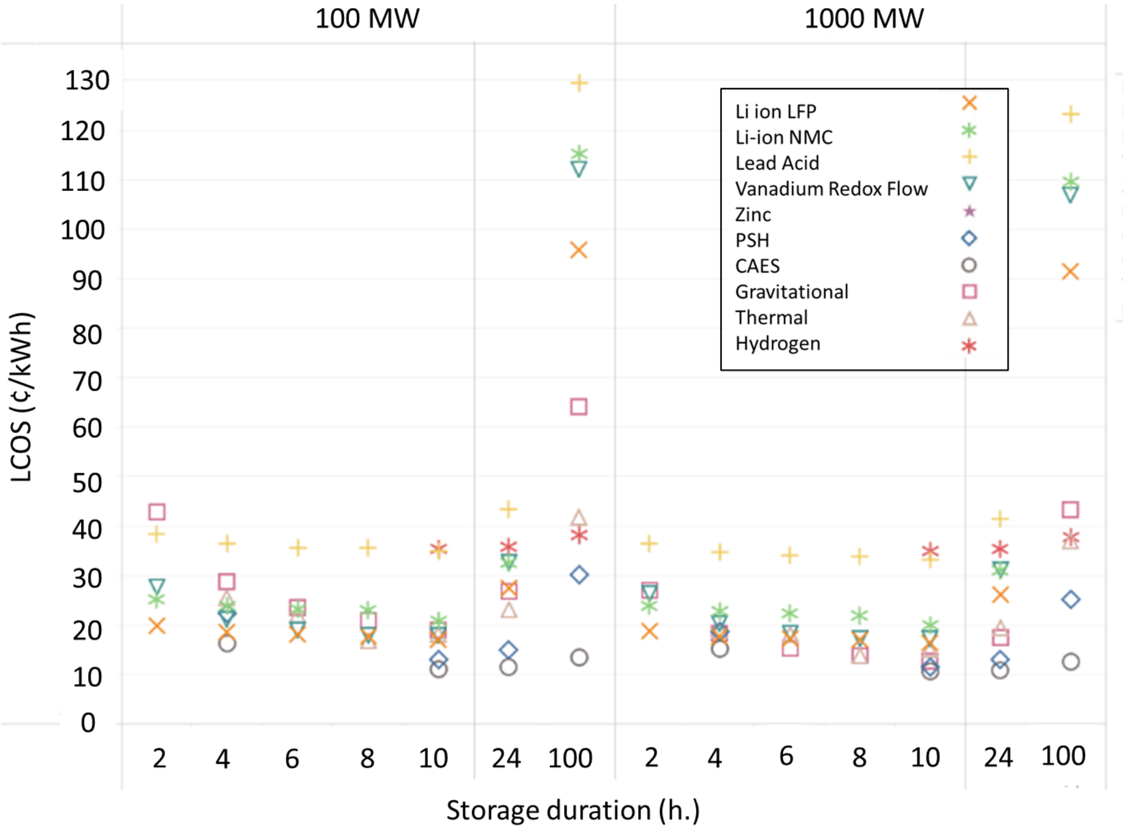

Figure 2- Comparison Of LCOS By Technology, Duration, and Power Capacity (¢/kwh). The LCOS Measures The Price That a Unit Of Energy Output From the Storage Asset Would Need To Be Sold At, To Cover All Project Costs Inclusive Of Taxes, Financing Costs, Operations And Maintenance, And Others [19].

At 10 h. duration, CAES is the lowest cost storage technology at ~10 ¢/kWh, followed by PSH (~15 ¢/kWh). Thermal and hydrogen storage also offer competitive pricing. In larger installations (1000 MW), CAES remains the most cost-effective option, with thermal and gravitational storage moving up in the ranking. Especially at 10 h. durations, PSH is on par with CAES, followed by gravitational storage. In the 100 h. duration category, CAES retains the lowest cost position, closely followed by PSH, with thermal and hydrogen following, and batteries trailing behind.

For extended-duration storage applications (over 10 h.), innovation is critical. In September 2021, the US Department of Energy (DOE) initiated the "Long-Duration Storage Shot" program, aiming to reduce costs by 90% for systems delivering more than

10 h. of storage duration within a decade. Traditional technologies like PSH and CAES have limitations in terms of their size and location [42]. Hydrogen is a promising candidate for long duration applications in the future, particularly "green" hydrogen created using renewable sources and carbon capture and storage, although this work is still restricted to the laboratory stage [43–45]. Efforts have been made to use concentrated solar power for water splitting to generate emission-free hydrogen, but the high temperature requirement (>1500 °C) poses a challenge for scalability and testing [46,47]. Therefore, exploring alternatives to hydrogen is vital for the development of a reliable energy storage infrastructure especially in the multi-day (10-200 h) storage mode [48].

1.2. Promise Of Thermochemical Energy Storage

Thermochemical energy storage offers the benefits of providing power, peak power support and off-sun power for utility-scale generation in locations of abundant solar radiation [49–53]. In TCES, the hot and reduced product of a thermochemical reduction reaction is utilized as energy storage media. Over the past few years, TCES has been a subject of particular interest due to its nearly lossless way of storing energy when the chemical reaction products are stored separately [51,54,55]. This can potentially lead to significant improvement in the volumetric density of energy storage over thermal energy storage. Several TCES systems with different storage capacities have been proposed in the literature [56–59]. These systems are usually designed to serve concentrated solar power (CSP) applications [49,60]. Solar energy is used to heat the particles to their thermal reduction temperature for TCES and the particles are stored hot to conserve sensible energy along with the chemical energy.

The promise of TCES is exemplified in the study by Gorman et al. [49] which provides a techno-economic model for a 111.7 MWe CSP system with a redox-active metal oxide (MO_x) acting as both the heat transfer fluid and storage media. In their system model, concentrated solar power provides the thermal energy for particle reduction after which the particles are stored in a storage chamber. The reoxidation reactor then supplements the power plant output, driving a Brayton cycle turbine. One important result from their study is the levelized cost of electricity of the modeled CSP plant with TCES for two cases, (i) 6 h. of storage with a solar multiple = 1.8 and (ii) 12 h. of storage with solar multiple = 2.4 [49]. Solar multiple is defined as the ratio between the thermal power produced by the solar field and the thermal power required by the power block under nominal conditions. Gorman et al. predicted an LCOE = 5-6 ¢/kWh depending on weather conditions and ~8% of the total costs attributed to the reduction reactor (Figure 3) [49]. The estimated LCOE of CSP with TCES is ~20% higher than the DOE 2030 target for baseload CSP with >12 h. storage (5 ¢/kWh) [7].

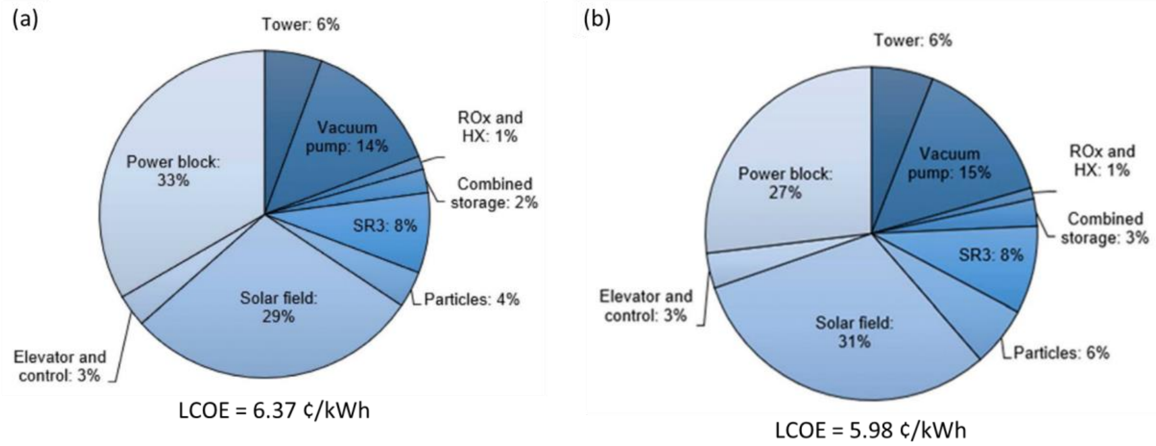

Figure 3- (a) Cost Breakdown and LCOE For Baseline System With 6 h. Of Storage And Solar Multiple=1.8, And (b) Lower LCOE Case With 12 h. Of Storage And Solar Multiple = 2.4 [49]. LCOE Is the Ratio Of the Sum Of the Total Capital Costs, the Annual Operation And Maintenance Cost And the Annual Replacement Costs, and the Total Annual Discharged Electricity

1.3. Reactive Metal Oxides For Thermochemical Energy Storage

Though the thermochemistry of sulfur [61] and ammonia [62] based systems have shown potential for TCES applications, metal oxide (MO_x) based cycles account for the majority of recent works [49,51,60,63]. The first type of MO_x-based systems utilize the stoichiometric oxides (e.g., $Co_3O_4 \rightarrow CoO$) [53,64] where the reaction occurs at a single temperature and pressure, and results in a crystalline phase change from reactants to products. Table 1 shows important stoichiometric metal oxides studied in the literature, their reaction temperatures and enthalpies (Δh), and the main issues observed during the reaction [65]. The cobalt-oxygen system has one of the highest reduction enthalpies among all stoichiometric oxides, but issues of cycling and formation of a CoO surface passivation layer prevents further reduction [65]. Similar issues are observed in the barium-oxygen system [65]. The Fe_2O_3 reduction occurs at 1400 °C limiting the choice of materials for reactor fabrication as well as the generation of high transformational stress on the crystal structure that can cause cracking [65].

Table 1- Examples Of Stoichiometric Oxide Systems And Their TCES Applicability [65]

Reactions	Reduction Temperature (°C)	Δh (kJ/mol_{oxide})	Issues observed	References
$Co_3O_4 \leftrightarrow CoO$	890	234	Cycling, passive layer	[53,64–68]
$PbO_2 \leftrightarrow PbO$	405	72	Intermediate phases	[54,65]
$BaO \leftrightarrow BaO_2$	885	131	BaO_2 passive layer	[65,69,70]
$CuO \leftrightarrow Cu_2O$	1120	225	Reaction temperature ≅ melting point	[54,65,71,72]
$Fe_2O_3 \leftrightarrow Fe_3O_4$	1400	137	High transformational stress	[65,68,73]

The second type of MO_x thermochemistry, and the focus of this study, are the non-stoichiometric oxides which exhibit continuous reduction states without crystallographic change depending on the local temperature and oxygen partial pressure

(pO_2). Non-stoichiometric MO_x, especially those with perovskite structure (Figure 4), typically contain mixed ionic electronic conductors (MIEC) which enable reaction and oxygen transport throughout the bulk. Perovskite refers to a class of materials with a crystal structure similar to $CaTiO_3$ [63]. These materials have been researched extensively but their use for energy storage is a much more recent venture. The most important characteristic of the perovskite structure is a transition metal lattice bounded on all sides by oxygen.

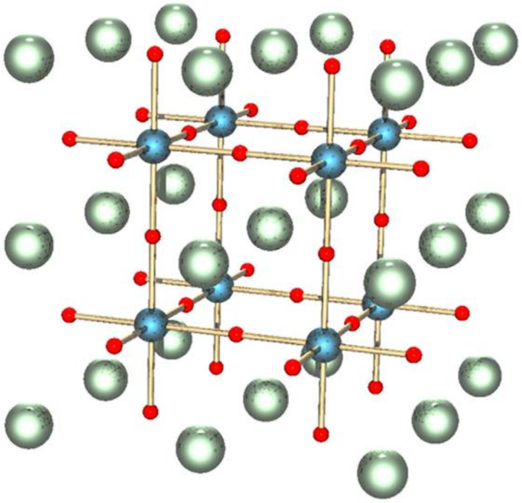

Figure 4- Structure Of a Typical ABO_3 Perovskite Structure [50], Red- Oxygen, Green- A-Site Cation, Blue- B-Site Cation. Careful Selection Of A And B Site Cations Can Lead To a Wide Range Of Thermochemical Properties Of the Structure.

A unique aspect of the perovskite structure is that the transition metal cations are easily replaced by similar materials, allowing the thermal and chemical properties to be tuned without changing the crystal structure [74,75]. The perovskite reaction uniformity and the structural porosity increase the lattice oxygen mobility during thermal reduction-oxidation (redox) cycles. The basic structure has an almost hexagonal packed layer of oxygen atoms containing alternating octahedral layers of the two atoms, A and B. The two metal atoms have different bond lengths with oxygen and different degrees of distortion [76]. The type and amount of distortion depends on the temperature, pressure, and the atomic composition of the material. This bond length and distortion determine the chemical and thermodynamic properties of the material [76]. Several studies have been performed to identify the suitability of various perovskite oxides for TCES [69,70,85–88,77–84].

The MO_x used in this study is $CaAl_{0.2}Mn_{0.8}O_3$ (CAM28), a MIEC perovskite and a promising candidate for TCES. In CAM28, aluminum is doped in a primary MO_x crystal of calcium manganite ($CaMnO_3$) and replaces 20% of Mn cations [89]. Calcium-containing perovskites are of special interest due to their low cost. The addition of difficult-to-reduce cations like Al^{3+} or Ti^{4+} leads to an increase in the M-O bond length and the reduction enthalpy. These dopants have also been hypothesized to stabilize the $CaMnO_{3-\delta}$ structure, which otherwise decomposes at temperatures around 1000 °C and a $pO_2 < 1000$ Pa. The thermal reduction reaction of CAM28 from an inlet temperature (T_{OX}) and extent of reduction (δ_{OX}) to an outlet temperature (T_R) and reduction extent (δ_R), with the addition of heat 'q' is shown in Eq. 1.

$$CaAl_{0.2}Mn_{0.8}O_{3-\delta_{OX}} \overset{q}{\leftrightarrow} CaAl_{0.2}Mn_{0.8}O_{3-\delta_R} + \frac{\Delta\delta}{2}O_2 \qquad \text{Eq. 1}$$

CAM28 has a significantly higher δ-specific reduction enthalpy compared to other potential materials like $La_{0.3}Sr_{0.7}Co_{0.9}Mn_{0.1}O_{3-\delta}$ (LSCM) (Figure 5) [90]. According to the literature, CAM28 and $CaTi_{0.2}Mn_{0.8}O_{3-\delta}$ (CTM28) outperform any oxide that has been previously explored for TCES [89]. Fully oxidized CAM28 reduces around temperatures of 900-1100 °C in a low pO_2 environment. The recoverable stored energy per kg MO_x (Ω) contains sensible energy, via the MO_x molar specific heat, c_{p,MO_x}, and chemical energy characterized by $\Delta\delta$ and Δh, where M_{MO_x} is the MO_x molar mass.

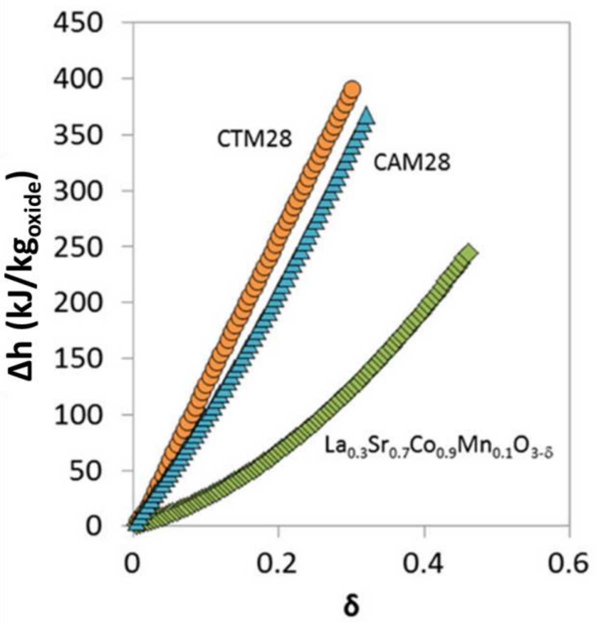

Figure 5- Reduction Enthalpies Of CAM And CTM Compared To LSCM [89]

$$\Omega = \frac{c_{p,MO_x}(T_R - T_{OX}) + \Delta\delta\Delta h}{M_{MO_x}} \quad \text{Eq. 2}$$

The TCES potential of CAM28 is primarily based on TGA data. TGA does not account for the reaction kinetics and therefore is an unreliable estimate of the energy storage potential under a reduction reactor environment. A reduction reactor that is designed with consideration of the reaction kinetics will fill this gap and help better understand CAM28, or any other MO_x's, TCES suitability.

1.4. Outline Of The Study

This work is framed within the development of a TCES system (Figure 6) to support a renewable energy-based electrical grid, where electricity prices exhibit significant variability. Though the MO_x form factor does not directly change the reduction reaction, particles are preferred here due to their larger surface area, over engineered monoliths. In this TCES system, a reduction reactor (the aim of this study) uses off-peak electricity to thermally reduce "cold" $MO_{x-\delta_{OX}}$ particles (stored at T_{OX} ~ 550 °C). The hot (~ 1100 °C) reduced particles ($MO_{x-\delta_R}$) serve as multi-day storage media [62]. In discharge, an energy recovery reactor (ERR) reoxidizes stored $MO_{x-\delta_R}$ particles, to supply the recovered heat for power generation. Oxidized $MO_{x-\delta_{OX}}$ particles return to the 550 °C storage bin. Typically, pO_2 below ambient and T ~ 1100 °C lead to a satisfactory $\Delta\delta$ [59]. Low pO_2 along the reaction path is typically achieved via vacuum pumping [91,92] or inert gas sweeping (here, N_2) [93–96].

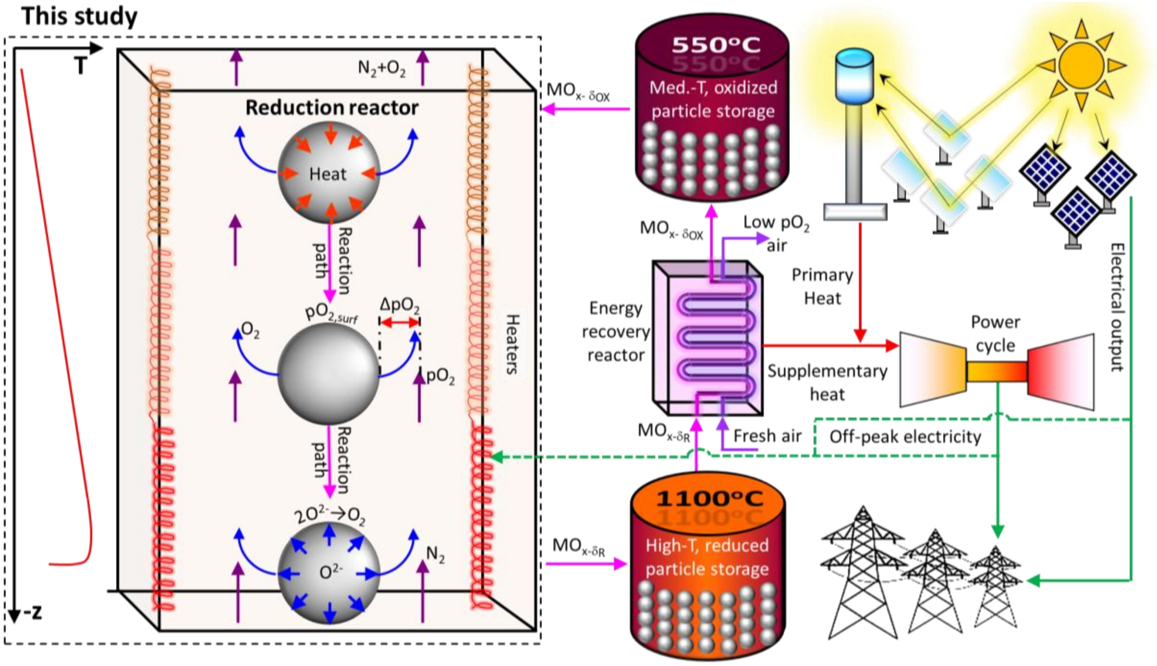

Figure 6. Schematic Of TCES Supporting a Renewables-Based Grid. During Storage Charging, the Reduction Reactor Heats and Reduces Particles From the "Cold" Oxidized Particle Storage (550 °C), Using Off-Peak Electricity, And Stores Them In the “Hot” Reduced Particle Storage (1100 °C). Factors For Maximizing MO_x Reduction Are Highlighted: (i) MO_x-Specific Temperature [97] (ii) Internal Heat Transfer, (iii) O^{2-} Ion Mobility, (iv) Surface Reactions, and (v) O_2-N_2 Mixing. During Discharge, the Energy Recovery Reactor Re-Oxidizes Particles From Hot Storage For Supplementary Heat.

1.5. Reactors Developed For Thermochemical Energy Storage

The reactor geometry houses two main components, (i) the particle flow mechanism and (ii) the O_2 removal mechanism. Though few reactor designs exist in TCES literature, the related fields of thermal energy storage and two-step water shift reactors (W-S) offer interesting candidate designs. In the common gravity-driven particle flow scheme, mechanical obstructions and flow along an inclined plane are examples of approaches to control τ_R [98,99]. Fluidized beds are also possible, though scaling and parasitic power requirements remain challenging [100,101]. Packed bed and the rotary kiln designs provide arbitrarily high τ_R [102], though their dense particle beds offer significant resistance to gas flow, sometimes reducing reaction rates by an order of magnitude [58,103,104].

A previously developed TCES reactor, the inclined plane scheme from Schrader et al., i.e., STInGR [96] (Figure 7), a.k.a. SR3 from Figure 3, is one of the few examples of TCES reactors in the literature. In the setup particles are irradiated using a radiation window before storage. The concept served as the reduction reactor model for Gorman et al.'s cost calculations, but the irradiation window incorporated in STInGR led to limited control on the reaction kinetics, causing low $\Delta\delta = 0.01$ at $T \sim 850$ °C in their study. Gorman et al. model assumes that the chosen reduction reactor can achieve a significant $\Delta\delta$ and storage densities.

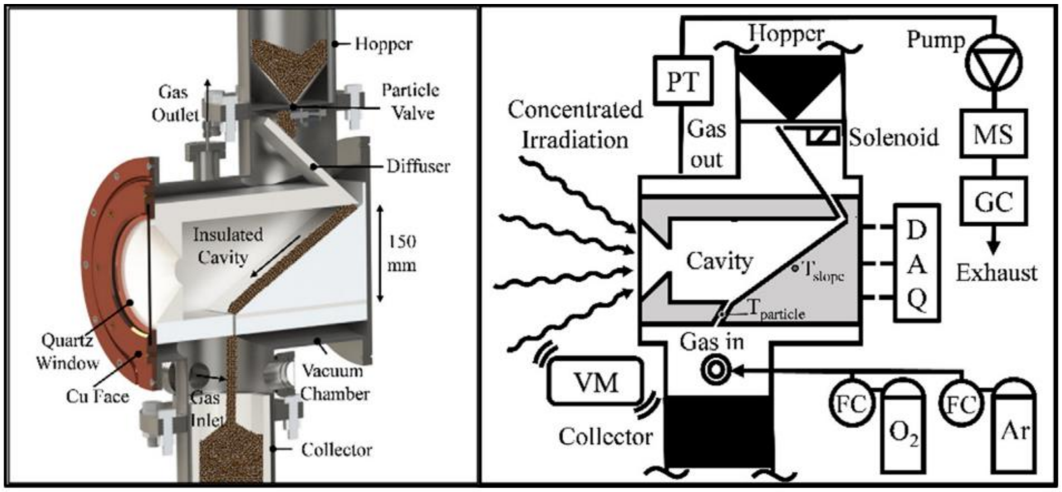

Figure 7- Left- CAD Model Of the STInGR System; Right- Process Flow Diagram Of the STInGR[96]

Significant reduction extent in CAM28 has only been observed in a TGA, which is only possible under specific temperature and pO_2 conditions that were not considered while designing STInGR [97]. An inert-swept thermochemical reactor can maximize $\Delta\delta$ and the sweep gas utilization, if the MO_x reaction path approaches reversibility. According to the reversible reactor described in de la Calle et al., a reversible reaction path requires:

i. Countercurrent flow between the MO_x and the inert gas: Analogous to a countercurrent flow heat exchanger, countercurrent flow helps maintain a constant reaction potential ($\Delta\mu$) between the MO_x and the inert gas for maximum oxygen extraction.

ii. Infinitesimal reaction step: A reaction step is defined as the reactor location with a uniform measurable change in δ. Infinitesimal step ensures the reversibility of the reaction path.

iii. Chemical equilibrium at each reaction step: Chemical equilibrium ensures $\Delta\delta$ maximization for a given temperature and pO_2. To approach chemical equilibrium, the MO_x must approach thermal equilibrium with its surroundings via a sufficiently small Biot number for rapid internal heat transfer [105]. Surface reaction kinetics and O^{2-} ion mobility primarily depend on temperature and therefore primarily depend on approaching thermal equilibrium. One measure of the proximity to chemical equilibrium is the $\Delta pO_2 = pO_{2,surf} - pO_2$ between the particle surface and the surrounding sweep gas (Figure 6), where $\Delta pO_2 = 0$ indicates equilibrium. Sufficient gas phase mass transfer kinetics are therefore also a critical design consideration.

iv. Complete O_2-N_2 homogenization before MO_x interaction: Complete O_2-N_2 homogenization ensures that the entire MO_x interacts with an inert gas with uniform

pO_2 to ensure reaction consistency at each step i.e., if N_2 flows in +z direction, then $\frac{dpO_2}{dx}, \frac{dpO_2}{dy}=0$ (Figure 6).

v. A mass balance dependent temperature profile: The work by de la Calle et al. showed that a reversible countercurrent flow reactor can only exist under a unique temperature profile, dependent on the mass balance line, which relates pO_2 with δ. This reversible temperature profile increases from the MO_x inlet/sweep gas outlet until a maximum temperature, followed by a decrease until the MO_x outlet/ sweep gas inlet. (Figure 6) [97].

In practice, these kinetic considerations imply the need for a sufficient MO_x particle residence time (τ_R) and sufficiently slow inert gas flow velocity. With these requirements in mind Table 2 summarizes the benefits and challenges with several reactor concepts analyzed for application with concentrated solar power (CSP). For example, the free-falling receivers have the capability of reaching high temperatures, but the thermal efficiencies are much lower than the obstructed flow designs. While efficiency gains can be achieved in the obstructed flow concepts, adding obstructions increases the reactor mass, complexity, and costs. Mechanized particle flow control designs, like the rotary kiln and fluidized bed concepts, offer more control over τ_R compared to gravity-driven particle flow, like free falling and obstructed flow designs. However, the addition of external particle flow control adds significant parasitic power decreasing the thermal efficiency, most prominent in fluidized beds. Also, scaling up the particle flow rates is a significant challenge with external flow control designs.

Table 2- Summary Of Reactor Concepts For Particle Heating With CSP [65]

Receiver design	Outlet	Benefits	Challenges	References

	temperatures/ thermal efficiencies			
Direct particle receivers- free-falling	> 700 °C/ ~ 50-80%	High temperature capability, and direct irradiance minimizes the heat flux required.	Radiative and convective heat losses, particle attrition, low τ_R, low effective particle/fluid heat transfer	[101,106–111]
Obstructed flow	> 700 °C/ 60-90%	High temperature capability, increased τ_R, flow stability and lower particle loss compared to free falling	Hot spots, requirement of cooling to avoid deterioration, higher cost of obstructions	[101,110,112,113]
Rotating kiln/centrifugal	900 °C/75%	High temperature capability, control of τ_R	Scaling up of flow rates, parasitic energy requirements, reliability issues with large rotating system	[114–117]
Fluidized bed	> 1000 °C/ 20-40%	High particle-gas heat transfer due to increased τ_R	Scaling up of flow rates, parasitic energy requirements for fluidization	[114,118–120]
Indirect particle receivers- gravity-driven flow in enclosures	N/A	High temperature capability, no particle loss	Hot spots can cause failure if mass flow and cooling not maintained, additional heat transfer resistance from walls to particles	[100,121]
Fluidized flow in tubes	750 °C/ N/A	Increased wall-to-particle heat transfer due to fluidization, no particle loss	Parasitic energy requirements for fluidization, scaling up of flow rate, hot spots require constant mass flux and cooling	[122,123]

1.6. Research Gap

Upon reviewing the literature a few of the main limitations of TCES are summarized in the form of the following research gaps and related research questions:

i. Can a practical reduction reactor approach the theoretical TCES capabilities of the redox materials?

In this study, this question is answered by providing an analytical model for approaching equilibrium along a discrete reaction path. Approaching equilibrium is essential to maximize the available redox capacity and the storage densities. This analytical model, a successor to the de la Calle's work [97], is an important step forward in understanding the physics of the reduction reaction.

ii. What process parameters are vital to the success of achieving low-cost grid-scale thermochemical energy storage with "ideal" materials?

The answer to this question reflects the main objective of the study: to develop reduction reactor solutions to maximize the energy storage density per unit MO_x, given a MO_x of known and suitable thermodynamic properties. The broader objective is to find pathways to minimize overall TCES costs at scale, to improve significantly on the state-of-the-art. This work builds on existing reactor designs to propose a novel thermochemical reduction reactor called the Zigzag Flow Reactor (ZFR). Several aspects of the ZFR are modeled such as the mass transfer and techno-economics under equilibrium operation. These models shed light on the critical process parameters for TCES success.

iii. What is the impact of repeated thermal and redox cycling on the storage density of materials with known properties, and what are the effects on the reactor?

This question is answered in two parts: (i) the ZFR concept is first proved using two laboratory scale prototypes, the α-ZFR and the β-ZFR, respectively. The performance observed in the α-ZFR provided valuable understanding of the reaction process leading to several diagnostic upgrades being added to the β-ZFR. (ii) the CAM28 storage density degradation with repeated thermal and redox cycles is monitored using independent δ

measurements after every run. The effect on the crystalline structure is analyzed using the X-Ray diffraction (XRD). Other non-destructive tests like scanning electron microscopy (SEM) and Electron dispersive spectroscopy (EDS) help track the degradation effects on the particle morphology and composition.

In this study, Chapter 1 establishes the problem statement and identifies the key research questions for this project. Following the considerations outlined in Chapter 1, Chapter 2 provides more details about the metal oxides and reactor concepts previously investigated for TCES. Chapter 2 also describes the relationship between δ, temperature and pO_2 and the relationship between δ and the reduction enthalpy. The information provided in Chapter 2 establishes a theoretical understanding of the MO_x reduction, enables comparison between previous studies in the thermochemistry field and helps identify the key factors impacting the design and performance of the reduction reactor. Chapter 3 then provides a method to model chemical equilibrium along a discrete (real) reaction path and identifies the consequences of operating away from equilibrium. An important factor for the success of a TCES reactor is the O_2-N_2 mass transfer, analyzed using an analytical model in Chapter 4. After modeling the equilibrium and diffusion kinetics along a discrete reaction path, Chapter 5 details important selection criteria for a reactor concept and the two prototypes developed to demonstrate the ZFR concept. In Chapter 6, a model for the scaled ZFR is utilized to estimate the levelized cost of thermochemical energy storage.

2. LITERATURE REVIEW

This chapter expands on the literature review presented in Chapter 1. First, the chapter provides more details about the different oxides investigated for TCES. This is followed by a detailed discussion about the factors that affect the reduction extent and the relationship between reduction extent and stored energy. Finally, more examples of thermochemical reactors from the TCES literature are described.

2.1. Metal Oxides for Thermochemical Energy Storage

Though several thermochemical cycles are potentially viable for TCES, in this study, MO_x are considered most viable due to their high temperature stability and availability in particle form. Many of these MO_x's have high phase transition temperatures and a stable phase at temperatures > 700 °C. High temperature phase transition is an important factor for efficient TCES. Below 250 °C the redox reaction kinetics are generally slow and heat recovery is inefficient. Thus, MO_x with high reduction temperature and stable phases at high temperature are important for efficient TCES. The listed oxides contain examples of stoichiometric oxides (similar to Table 1) and non-stoichiometric oxides.

2.1.1.Manganese Oxide

Manganese oxygen redox system displays an array of stable oxides: $MnO_2 \leftrightarrow Mn_2O_3 \leftrightarrow Mn_3O_4 \leftrightarrow MnO$, each of which has advantages and disadvantages. Notably, the redox equilibrium temperature for the $Mn_3O_4 \leftrightarrow MnO$ transformation is quite high, reaching 1700 °C [65]. Reoxidizing Mn_2O_3 to MnO_2, as suggested by existing literature, presents a formidable challenge, often requiring pure oxygen at a staggering 3×10^8 Pa pressure [65]. During the $MnO_2 \leftrightarrow Mn_2O_3$ decomposition, researchers have observed the emergence of various intermediate oxide phases. These intermediates could be the reason for the difficulty achieving the $Mn_2O_3 \leftrightarrow MnO_2$ reoxidation process. In stark contrast, the reduction and reoxidation processes for $Mn_2O_3 \leftrightarrow Mn_3O_4$ and $Mn_3O_4 \leftrightarrow MnO$ have been successfully demonstrated under ambient pressure conditions. A factor influencing these processes is the particle size of the manganese oxide. High surface area, i.e., fine grain size, reduces the re- oxidation temperature of Mn_3O_4 [65]. Given these promising characteristics, manganese oxide systems hold tremendous potential for applications in TCES [50,53,65,68,124].

2.1.2.Cobalt Oxide

The cobalt oxide redox system primarily undergoes a single phase transition, occurring at temperatures of approximately 890°C and above when exposed to air, involving the transformation of Co_3O_4 (spinel) to CoO [66]. This redox reaction exhibits remarkable reversibility, making it particularly appealing for various applications. The kinetics of this reaction are predominantly influenced by heat transfer and diffusion processes, which significantly enhance the potential utility of Co_3O_4 in TCES [65]. However, it is worth noting that larger CoO particles have previously encountered challenges during re-oxidation at lower temperatures. This difficulty arises from the presence of a passivation surface layer of Co_3O_4 [65]. Therefore, addressing this issue is crucial for optimizing the performance of cobalt oxide in long-term TCES operations. Additionally, it's important to acknowledge that the redox performance of cobalt oxide can degrade with repeated cycling [65]. This underscores the need for careful management and maintenance in long-term applications [53,64–68].

2.1.3. Iron Oxide

Iron oxide compounds, specifically Fe_2O_3 (hematite) and Fe_3O_4 (magnetite), are abundant and extensively documented in the literature for their transition characteristics. In the iron-oxygen system, two principal redox transitions are recognized: the conversion of $Fe_2O_3 \leftrightarrow Fe_3O_4$ and the transition from $Fe_3O_4 \leftrightarrow FeO$. The decomposition of Fe_3O_4 into FeO in an air environment necessitates high temperatures, exceeding 2000°C, rendering it impractical for laboratory-scale testing. The reduction of $Fe_2O_3 \leftrightarrow Fe_3O_4$ initiates at temperatures exceeding 1200°C, although it is noteworthy that a high moisture content in the atmosphere can decelerate the typically rapid re-oxidation rate. During these transitions, the generation of transformation stress may lead to the formation of porosity and cracks, particularly during the reduction step. As a result, these characteristics render the system unsuitable for application in TCES [65,68,73].

2.1.4. Lead Oxide

Lead oxide redox system has emerged as a promising candidate for TCES, primarily due to its cost-effectiveness [54]. Within the literature, two stable phases of lead oxide have been identified: $PbO_2 \leftrightarrow PbO$ [54]. However, the presence of intermediate Pb-O phases, along with the lattice strain they induce, results in the formation of various intermediary lead oxides [54]. These intermediate phases lead to the release of reduction enthalpy across a broad spectrum of temperatures as lead undergoes transitions between different oxidation states. This temperature-dependent enthalpy release poses a significant challenge when attempting to design a system that effectively harnesses the TCES potential of lead oxides. Ideally, for efficient TCES applications, a suitable material should release its reduction enthalpy within a narrow and well-defined temperature range.

2.1.5. Antimony Oxide

In the antimony-oxygen redox system, literature reports only one well-documented oxide transition: $Sb_2O_5 \leftrightarrow Sb_2O_4$. However, a metastable phase that frequently appears in the literature is Sb_2O_3 [65]. The transitions between Sb_2O_3, Sb_2O_4 and Sb_2O_5 are relatively intricate due to the thermal instability of Sb_2O_5 and the volatility of Sb_2O_3. While the decomposition of $Sb_2O_5 \leftrightarrow Sb_2O_4$ has been experimentally demonstrated, the re-oxidation of Sb_2O_4 in an air environment remains unverified. Consequently, there is limited research available to conclusively assess the TCES potential of the antimony oxide system [65].

2.1.6. Vanadium Oxide

The vanadium-oxygen redox system has shown various oxide transitions like $V_2O_5 \leftrightarrow V_2O_4$ and additional higher temperature transition between $VO_2 \leftrightarrow V_2O_3$ [65,125]. A number of other intermediate phases like V_3O_5, V_4O_7 and V_6O_{13} have been observed repeatedly in experiments [65]. Experiments indicate the lethargic kinetics of $V_2O_5 \leftrightarrow V_2O_3$ reduction in an inert gas environment while exposure of V_2O_3 to air has been shown to promote oxidation, but the temperature range for re-oxidation and the kinetics are not described in literature reviewed [65]. The presence of intermediate phases, like the lead oxide system, makes vanadium oxide unsuitable for TCES [65].

2.1.7. Barium Oxide

The barium-oxygen redox system displays only one oxide transition system: $BaO \leftrightarrow BaO_2$. Previously, the $BaO \leftrightarrow BaO_2$ redox system has been studied for chemical heat storage [65,69,70]. These redox transitions have been shown to be reversible but additional cycling led to a decrease in the conversion fraction. This happens due to the formation of a passive BaO_2 surface layer on the BaO particles during re-oxidation, similar to cobalt oxide [65]. This layer prevents the diffusion of oxygen into the BaO particles and thus reduces their re-oxidation. Additional research in ensuring high diffusion of oxygen to the particles is required for the barium oxide system to be considered viable for TCES.

2.1.8.Copper Oxide

Only the CuO ↔ Cu_2O transition is known in the copper oxygen redox system. The reduction of CuO in air takes place at temperatures around 1000 °C [54,65,71,72]. Since the melting point of Cu_2O is 1232 °C, the proximity of reduction and melting temperatures leads to challenges in designing a reactor around it. There is a lot of grain coarsening that takes place near these temperatures which further leads to problems in the reactor design [65]. However, previous literature has shown re-oxidation of Cu_2O at a temperature significantly lower than the equilibrium transition temperature [65]. This provides a unique advantage for reactors designed around it. Thus, in spite of its problems, copper oxide is potentially a good candidate for TCES [65].

2.1.9.Mixed Metal Oxides

There are two main types of mixed metal oxide redox reactions: (i) solid-solid $(\mathrm{Mn_2O_3} + 2\mathrm{Fe_2O_3} \rightarrow 2\mathrm{MnFe_2O_4} + \mathrm{O_2})$ and (ii) solid-solution $\left(\mathrm{Co_2NiO_4} \rightarrow \mathrm{Co_2NiO_3} + \frac{1}{2}\mathrm{O_2}\right)$ [65]. In solid-solid type, the two oxides form a single phase oxide after the reaction. Thermal cycling caused material attrition limits the TCES applicability of these systems [65]. The second type of system is the solid-solution type in which the cations take up different lattice sites in an oxide matrix. Such an oxide undergoes a redox reaction similar to a pure oxide.

With proper selection of the secondary cation in the primary oxide matrix, solid-solution systems are good candidates for TCES [55,58–60,89,126–129]. The secondary cation replaces the primary metal cation at several lattice points in these materials. The replacement of the primary cation can be stoichiometric, e.g., substitution of Co by Ni in Co_3O_4 leads to the formation of Co_2NiO_4, or only partial, e.g., doping of Co_3O_4 with Fe_2O_3. It has been shown that $FeNiCoO_4$ does not decompose as compared to Co_2NiO_4 [65]. This stability comes from the location of cations in the spinel structure of Co_3O_4. The original substitution of Co with Ni leads to local charge imbalance due to high affinity of both Co^{3+} and Ni^{2+} to the octahedral sites in the spinel structure. Thus, when Ni^{2+} replaces Co^{3+} in the structure the resulting $Co^{3+}[Ni^{2+}Co^{3+}]O_4$ has one unallocated positive charge. This leads to creation of oxygen imbalance vacancies which leads to an increase in reduction kinetics. On the other hand, replacement of Fe^{3+} replaces Co^{3+} in the tetrahedral site leads to neutral lattice and slow kinetics [65].

Such a secondary cation doping decreases the phase transition temperatures if the dopant is chosen carefully. Several examples of this practice have been demonstrated in the literature, e.g. Co_3O_4 doping into Mn_3O_4 and Mn_2O_3 doping into Fe_2O_3 etc. [50,65] . The doping leads to an increase in the creation of oxygen vacancies that function as active centers during the oxygen chemisorption and re-oxidation process. The effectiveness of these materials depends upon the valance state and ionic radii of the secondary cations. These dopants have been shown to increase the reactivity of CoO with oxygen and help in the decomposition of Co_3O_4 by reducing the reaction temperature. This method has also been shown to increase the reactivity of lead and vanadium oxides [65]. Thus, doping of materials is an effective way of increasing the viability of several pure oxides for TCES.

2.2. Reduction Extent

With an understanding of the different TCES oxide systems, the next few sections detail the factors influencing the reduction extent and its relationship with the reduction reaction enthalpy.

2.2.1. Factors Influencing the Reduction Extent

Babiniec et al. [9] conducted a study to investigate the parameters that influence the amount of oxygen removed during reduction and thus the value of δ. Their study characterized the δ behavior of several compositions of MO_x like $La_xSr_{1-x}Co_yFe_{1-y}O_{3-\delta}$ (LSCF) and $La_xSr_{1-x}Co_yMn_{1-y}O_{3-\delta}$ (LSCM) compounds [127]. In their study, Babiniec et al. [9] subjected the MO_x particles to controlled atmospheres and heated them from 200 °C to 1250 °C using a thermogravimetric analyzer (TGA). The changes in δ during this temperature increase were denoted as $\Delta\delta_1$ (in air atmosphere) and $\Delta\delta_2$ (in argon atmosphere). Subsequently, the particles were cooled from 1250 °C to 200 °C in air, and the change in δ during this cooling phase was referred to as $\Delta\delta_3$. All of these Δδ values were calculated using Eq. 3.

$$\Delta\delta = \left(\frac{\Delta m}{m_{in}}\right) \left(\frac{MW_{MO_x}}{MW_O}\right) \qquad \text{Eq. 3}$$

Eq. 3 relates δ to the measured mass change (Δm) using TGA where m_{in} is the initial mass, MW_{MO_x} is the molecular weight of the fully oxidized MO_x, and MW_O is the molecular weight of monoatomic oxygen. Figure 8 depicts the δ dependence on temperature and gas environment, analyzed based on material weight changes.

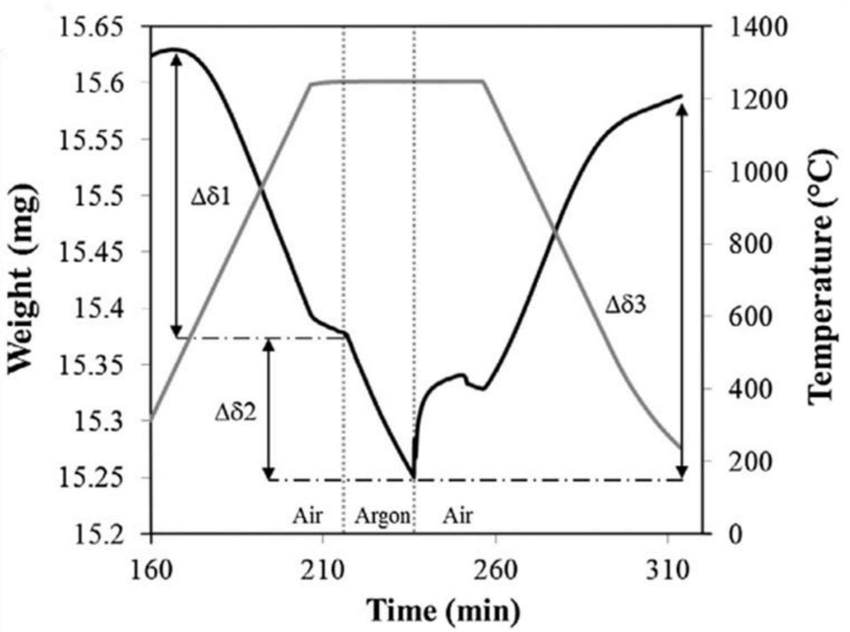

Figure 8. TGA Analysis Showing the Changes In Oxygen Non-Stoichiometry With Temperature [127].

Figure 8 illustrates the weight reduction of the sample as temperature increases, followed by a further decrease when argon replaces air. Reoxidation by introducing air results in an increase in sample weight due to the addition of oxygen. The temperature and gas variations can be inferred from Figure 8 to determine the changes in $\Delta\delta_1$, $\Delta\delta_2$ and $\Delta\delta_3$. Table 3 provides the variations of $\Delta\delta_1$, $\Delta\delta_2$ and $\Delta\delta_3$ for different LSCM and LSCF compositions under the same operating conditions.

Table 3. Crystallography and Pre-Screen Redox Properties Of Several $La_xSr_{1-x}Co_yMn_{1-Y}O_{3-\delta}$ and $La_xSr_{1-x}Co_yfe_{1-Y}O_{3-\delta}$ Compounds [127]

Nominal Composition	> 95% single phase?	Crystal structure	Δδ1	Δδ2	Δδ3
LSCM1991	Yes	Tetragonal	0.25	0.12	0.32
LSCM1982	Yes	Tetragonal	0.2	0.12	0.31
LSCM1973	Yes	Tetragonal	0.21	0.11	0.28
LSCM2891	Yes	Tetragonal	0.25	0.11	0.33
LSCM2882	No	Tetragonal	0.21	0.11	0.28
LSCM2873	Yes	Tetragonal	0.23	0.12	0.31
LSCM3791	No	Cubic	0.31	0.12	0.39
LSCM3782	Yes	Cubic	0.28	0.12	0.36
LSCM3773	Yes	Cubic	0.23	0.12	0.3
LSCM4664	Yes	Cubic	0.17	0.11	0.24
LSCM7337	Yes	Rhombohedral	0.03	0.07	0.01
LSCM8228	Yes	Rhombohedral	0.02	0.05	-0.007

LSCM8237	Yes	Rhombohedral	0.02	0.05	-0.003
LSCM9119	Yes	Orthorhombic	0.04	0.06	0.02
LSCM9128	Yes	Orthorhombic	0.02	0.05	-0.002
LSCM9137	Yes	Orthorhombic	0.03	0.06	-0.005
LSCF1991	Yes	Cubic	0.23	0.09	0.31
LSCF1982	Yes	Cubic	0.30	0.11	0.37
LSCF1973	Yes	Cubic	0.29	0.1	0.36
LSCF2891	Yes	Cubic	0.31	0.11	0.38
LSCF2882	Yes	Cubic	0.32	0.11	0.38
LSCF2873	No	Cubic	0.3	0.11	0.38
LSCF2828	Yes	Cubic	0.3	0.09	0.35
LSCF3791	Yes	Cubic	0.3	0.12	0.38
LSCF3773	Yes	Cubic	0.32	0.11	0.40
LSCF4691	Yes	Cubic	0.27	0.12	0.35
LSCF4682	Yes	Cubic	0.28	0.12	0.36
LSCF4673	Yes	Cubic	0.26	0.11	0.35
LSCF4646	Yes	Cubic	0.25	0.1	0.3
LSCF4664	Yes	Rhombohedral	0.26	0.11	0.32
LSCF5555	Yes	Rhombohedral	0.22	0.11	0.29
LSCF6446	Yes	Rhombohedral	0.17	0.11	0.22
LSCF7337	Yes	Rhombohedral	0.1	0.1	0.19
LSCF8228	Yes	Rhombohedral	0.06	0.09	0.06
LSCF8237	Yes	Rhombohedral	0.07	0.1	0.08
LSCF9128	Yes	Rhombohedral	0.03	0.07	0.01
LSCF9137	Yes	Rhombohedral	0.04	0.08	0.03

Table 3 shows the material's composition impacts the extent of reduction. $La_{0.3}Sr_{0.7}Co_{0.9}Mn_{0.1}$ ($\Delta\delta_3 = 0.39$) and $La_{0.3}Sr_{0.7}Co_{0.7}Mn_{0.3}$ ($\Delta\delta_3 = 0.40$) exhibit the highest redox capacity. $\Delta\delta_{1\text{-}3}$ values remain relatively constant at low La concentrations, peak at La content of 0.3, and decline sharply with higher La concentration.

It is also important to understand how the reduction extent changes with temperature and oxygen partial pressure (pO_2) in the atmosphere. Figure 9 shows the dependence of δ on the temperature and pO_2 for the material LSCF3773. The δ for LSCF3773 increases with a decrease in pO_2 and increases with increase in temperature at constant pO_2. To summarize, δ depends upon (i) the temperature (ii) the pO_2 and (iii) the material composition.

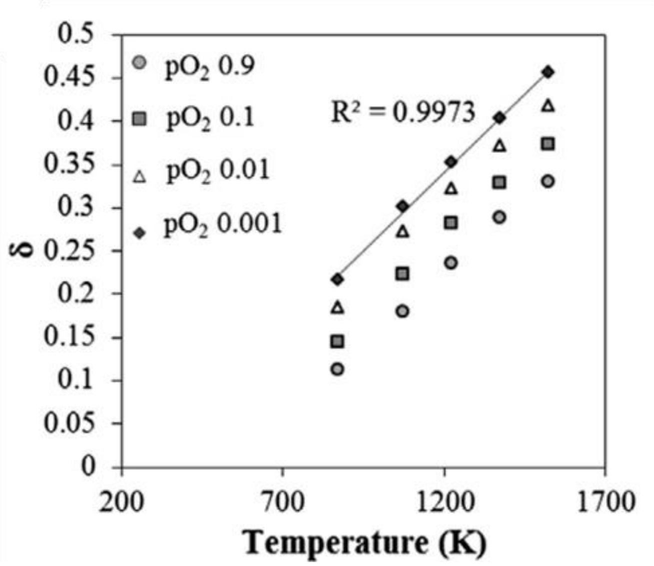

Figure 9. Changes In the Extent Of Reduction Of LSCF 3773 As a Function Of Temperature and pO_2 [127]

2.2.2. Relation Between Reduction Extent and Reduction Enthalpy

The linear fits observed in Figure 9 can be transformed to Van’t Hoff form to calculate the enthalpy of reduction reaction [127]. Each enthalpy point represents a mole of oxygen being removed from the lattice at a specific δ. Therefore, a series of points in a Van't Hoff analysis represents a continuous reduction process occurring at different compositions. The enthalpy required to remove all oxygen atoms, as calculated from the Van't Hoff analysis for a particular δ, is referred to as the reduction enthalpy and can be expressed using Eq. 4 [127].

$$\Delta \mathrm{h}\left[\frac{\mathrm{kJ}}{\mathrm{mol\ perov}}\right] = \int_{\delta_1}^{\delta_2} \Delta \mathrm{h}\left[\frac{\mathrm{kJ}}{\mathrm{mol\ O_2}}\right].\,\delta\left[\frac{\mathrm{mol\ O}}{\mathrm{mol\ perov}}\right].\,\frac{1}{2}\left[\frac{\mathrm{mol\ O_2}}{\mathrm{mol\ O}}\right] \qquad \text{Eq. 4}$$

Figure 10 shows the resulting dependence of the reduction enthalpy on Δδ. It is important to note that the reduction enthalpy increases with an increase in δ. This is because it becomes progressively more challenging to create new oxygen vacancies as the number of vacancies increases. LSCF exhibits easier reduction at lower δ values, resulting in lower energy storage capacity. However, as δ values increase, the potential for energy storage also increases. On the other hand, LSCM compounds have the ability to store a larger amount of energy at lower δ values, making them more suitable for energy storage applications at lower extents of reduction.

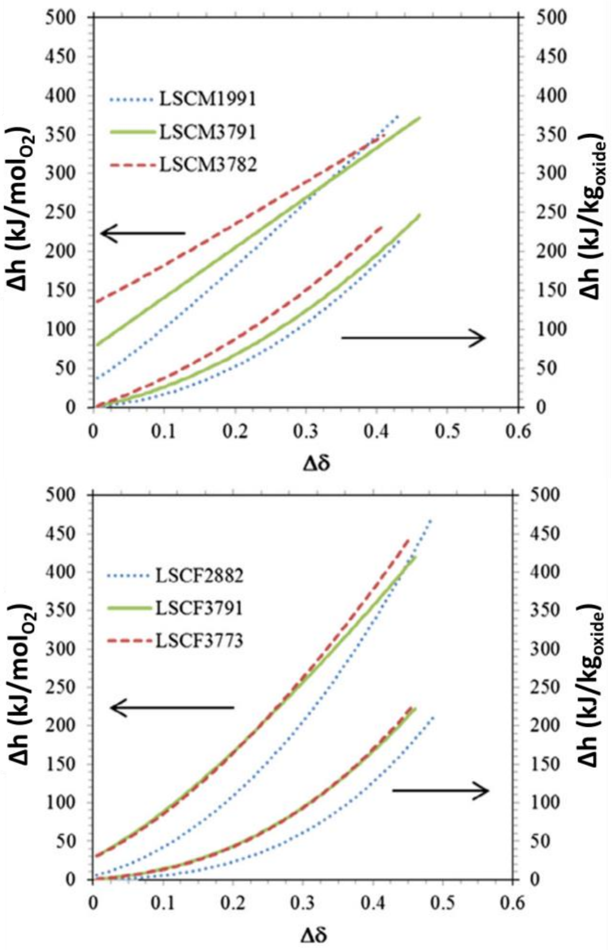

Figure 10. Reduction Enthalpy As a Function Of Reduction Extent [127] For LSCM (Top) And LSCF (Bottom) [127]

The total energy stored in the material is a combination of thermal and chemical stored energy. The thermal energy stored does not vary significantly with changes in the composition of LSCF and LSCM compounds. Therefore, the chemical energy stored serves as a good indicator for differentiating the stored energy in the system. Among all the candidate materials in the study, LSCM3791 exhibits the highest weight-specific enthalpy of 250 kJ/kg MO_x, highlighting its superior energy storage capacity.

2.2.3. Relation Between Temperature, Oxygen Partial Pressure and Reduction Extent

A relationship between the operational variables temperature, pO_2 and δ, called T-pO_2-δ relationships, are needed to develop reactors that maximize the energy storage. A model for predicting the performance of MO_x for reduction and oxidation in oxygen environments is given by Bulfin et al. [130]. This model is used to predict the equilibrium composition and reaction kinetics to estimate the performance of the material. This model is based primarily on the Arrhenius equation for kinetics. At equilibrium, both reduction and oxidation of metal oxides (MO_x) occur at the same time (Eq. 5) [130].

$$\mathrm{MO_x} \leftrightarrows \mathrm{MO_{x-\delta}} + \frac{\delta}{2}\mathrm{O_2} \qquad \text{Eq. 5}$$

The analysis assumes that phase decomposition does not take place in this reaction. Removing too much oxygen from the metal oxide can lead to phase change, thereby changing the fundamental properties and reaction kinetics. Thus, it is appropriate to assume that the reaction proceeds only to a maximum value of δ, say δ_m. Eq. 5 thus in limiting case leads to Eq. 6 [130].

$$\mathrm{MO_x} \leftrightarrows \mathrm{MO_{x-\delta_m}} + \frac{\delta_m}{2}\mathrm{O_2} \qquad \text{Eq. 6}$$

The reduction reaction is primarily dependent upon the removal of O from the MO_x [O_{MOx}], whereas the oxidation reaction depends upon the concentration of O vacancies [O_{vac}] and the concentration of O_2 gas in the environment [O_{gas}]. Thus, the rate of formation of O vacancies is the rate at which O leaves the oxide (reduction) minus the rate at which the recombination occurs (oxidation). In Eq. 7, k_r and k_{ox} are the rate constants for reduction and oxidation reactions, respectively.

$$\frac{d[O_{vac}]}{dt} = k_r[O_{MOx}] - k_{ox}[O_{vac}][O_{gas}]^n \qquad \text{Eq. 7}$$

These rate constants can be calculated using the Arrhenius equation as shown in Eq. 8.

$$k_i = A_i \exp\left(\frac{-E_a}{RT}\right) \qquad \text{Eq. 8}$$

Dividing Eq. 7 by concentration of metal oxide [MO$_x$] leads to Eq. 9,

$$\frac{1}{[MO_x]}\frac{d[O_{vac}]}{dt} = \frac{[O_{MOx}]}{[MO_x]}k_r - \frac{[O_{vac}]}{[MO_x]}[O_{gas}]^n k_{ox} \qquad \text{Eq. 9}$$

The rate of the reaction can now be defined in terms of stoichiometric parameters like δ and δ_m since both $[O_{MOx}]/[MO_x]$ and $[O_{vac}]/[MO_x]$ are unitless as shown in Eq. 10

$$\frac{[O_{MOx}]}{[MO_x]} = \delta_m - \delta \quad \text{and} \quad \frac{[O_{vac}]}{[MO_x]} = \delta \qquad \text{Eq. 10}$$

Using the fact that (i) [O$_{gas}$] is directly proportional to pO$_2$ (assuming ideal gas) and (ii) the rate of reaction at equilibrium is 0, Eq. 8, Eq. 9 and Eq. 10 can be used to derive the following equilibrium condition in Eq. 11 where coefficients 'r' and 'ox' stand for reduction and oxidation respectively.

$$(\delta_m - \delta)A_r\left(\frac{-E_r}{RT}\right) - \delta pO_2^n A_{ox}\left(\frac{-E_{ox}}{RT}\right) = 0 \qquad \text{Eq. 11}$$

Rearranging the terms, Eq. 12 shows the [O$_{vac}$] in terms of temperature and pO$_2$. In Eq. 12, E_a is the activation energy of the reduction reaction (E_r - E_{ox}).

$$\left(\frac{\delta}{\delta_m - \delta}\right) = \frac{A_r}{A_{ox}} pO_2^{-n} \exp\left(\frac{-E_a}{RT}\right) \qquad \text{Eq. 12}$$

Note that [O$_{vac}$] is equivalent to the concentration of oxygen removed during the reduction reaction. The values of n and δ_m are calculated by optimizing Eq. 12 to fit previously published experimental results. Figure 11 shows the estimated variation of δ with temperature and pO_2 for ceria reduction ($CeO_2 \leftrightharpoons CeO_{2-\delta} + \delta/2\ O_2$). It is apparent that δ increases with an increase in temperature at constant pO_2 and with a decrease in pO_2 at constant temperature, confirming earlier results from LSCF and LSCM studies. Figure 11 is an example of T-pO_2-δ relationships for one material. These relationships are unique to a specific material (CeO_2 in case of Figure 11).

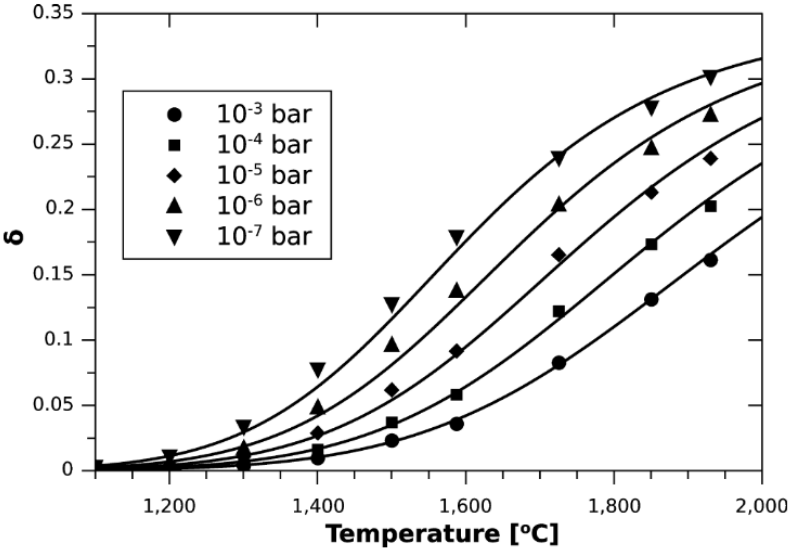

Figure 11. Dependence Of δ On pO_2 and Temperature For CeO_2 [130]

2.3. Previous Receiver/Reactor Designs

The next few sections contain descriptions of several different reactor concepts from the literature. Understanding their benefits will help narrow down the best features that contribute to uniform and continuous particle heating and reduction. Several of these reactor designs have been used for TES with particle heating and not reduction (receivers). The receiver designs, with small modifications, can be employed for TCES applications. For this study, the primary parameter for selection of reactor design is good control of particle residence time (τ_R) with a scalable design.

2.3.1. Free Falling Receivers

A basic form of a direct particle heating receiver contains particles falling through a channel receiver while being irradiated by concentrated solar power (CSP). Figure 12 shows the particles fall from the hopper on top of the reactor in the form of a curtain or thin sheet.

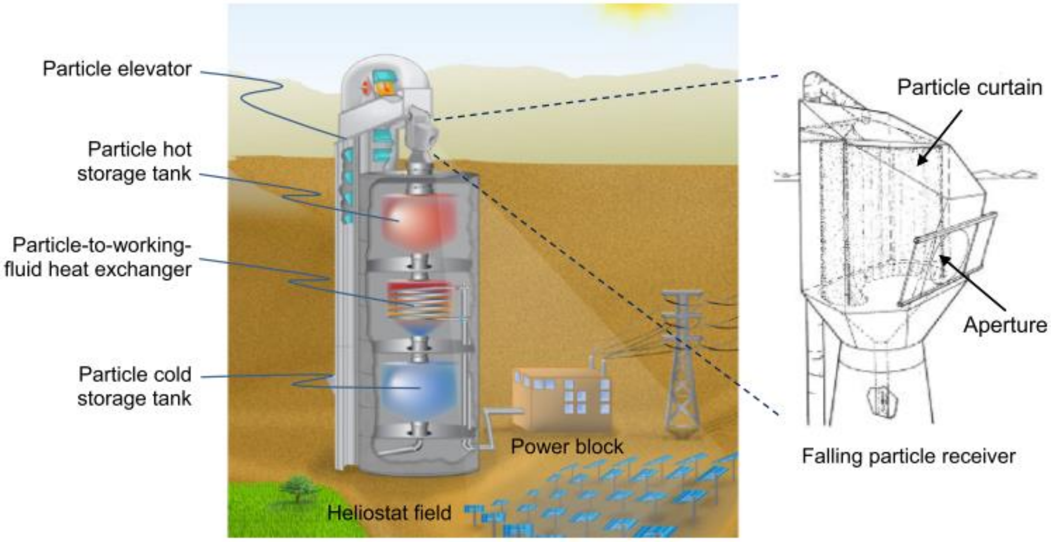

Figure 12. Falling Particle Receiver Concept With Integrated Storage and Internal Heat Exchange[131]

Literature contains several previous studies that have been performed on direct free-falling particle receivers [106–109,111,132]. The majority of the studies focus on modeling the hydraulics of particles and the irradiation heat transfer to the falling particles. One common design concept deals with a north-south facing channel that gets heated by a surrounding heliostat field [132]. One of the first on-sun tests (in batch mode) of a simple-free falling particle receiver was performed by Siegal et al. [109]. These tests achieved a maximum thermal efficiency of ~ 50% and a maximum temperature rise of 250 °C. Ho et al. also performed on-sun tests of a 1 MW_{th} continuously recirculating particle receiver with a bulk outlet temperature of the particles over 700 °C. The thermal efficiency of this reactor varied from 50% to 80% [133]. Results show that the thermal efficiency increases with an increase in the particle flow rate, but the temperature rise decreases. This occurs with an increase in particle flow because the opacity of the particle curtain increases thereby intercepting more heat from the heliostat. Thus, heat is absorbed by the particle at a higher thermal efficiency. On the other hand, increase in flow rate decreases the temperature rise due to shading of the particles in the layers facing away from the sun. The main problems that were identified included non-uniform irradiance distribution on the particle curtain, variable mass flow rates, impact of wind, loss of particles through the aperture and thermal wear of the reactor walls due to high temperature and direct irradiance [133].

The heating and the exit temperature of the particles depend on τ_R in the channel. Increasing this τ_R is an important factor in achieving high particle temperatures. To increase the τ_R, one proposed method is recirculation of particles through the channel, successively increasing the particle temperature [101,132].

2.3.2.Obstructed Flow Receivers

One method to increase the τ_R is to obstruct the flow of the particles by passing them through porous structures or an array of mechanical obstacles. These particles are heated in the channel while undergoing heating through concentrated solar power. Early concepts of an obstructed flow receiver were introduced by Sandia National Laboratories in early 1980s by using ceramic structures suspended from the receiver wall to impede the flow of the particles [101]. The STInGR described earlier, is a form of an obstructed flow reactor, where the free fall of particle is passively controlled using an inclined plane.

Additional studies used staggered array of porous mesh structures to impede the flow and to increase the τ_R of particles[101]. Ho et al. used staggered chevron shaped stainless steel mesh structures and performed on-sun tests to characterize the performance of the particle receiver [110]. The staggered chevron shaped mesh structure is shown in Figure 13. The maximum temperature reached by the particles is 700 °C near the center of the receiver, but the particle temperature rise per meter of drop length is lower towards the end of the receiver due to non-uniform irradiance. The height specific temperature rise in the early part of the vertical particle fall, i.e., near the top of the receiver, is half of that achieved at the receiver center because the irradiance doubles from the top going towards the center. The thermal efficiency of the receiver increases from ~ 60% to ~ 65% from the receiver top to the center [110]. This particle receiver reduces the impact of wind compared to free falling receivers, improving particle heating, and reduces the loss of particles through the aperture for irradiation. Direct irradiance causes problems for the stainless steel meshes due to degradation and oxidation. New materials and operational strategies to counter the mesh deterioration are the main requirement for this design.

Figure 13. Flow Of Particles Over Staggered Chevron Shaped Mesh Structures [110]

Another obstructed flow design employs a spiral lamp along which the particles flow under gravity and the flow rate is controlled using vibration [134]. This receiver concept reaches a maximum particle temperature of 650 °C at the outlet after 30 min of 5 kW heating at the aperture. The maximum thermal efficiency of this receiver is ~ 60%. The main problems with this receiver include the complications of beam down optics and scaling up of the particle flow rate [134].

2.3.3.Rotary Kiln/Centrifugal Receivers

Rotary kilns were proposed in the early 1980s for solar particle heating applications [101]. In this receiver, particles are fed through a rotary kiln/receiver with an aperture for solar irradiance. The centrifugal force of the rotating receiver makes the particles move along the walls where they are heated with CSP. These reactors have accurate control of the τ_R. Early tests indicate a very high thermal absorption efficiency of 90-100% but very low thermal efficiency of 10-30% for heating $CaCO_3$ at a flow rate of 1 g/s [101]. A schematic of the rotary kiln/receiver proposed by Wu et al. is shown in Figure 14 [115–117]. Bauxite ceramic particles of ~ 1 mm diameter were sent to the rotary kiln at a flow rate of ~ 3-10 g/s. The particles were irradiated with a 15 kW_{th} solar simulator at an irradiance of ~ 300-700 kW/m^2. For a face down receiver inclination and incident irradiance of 670 kW/m^2, this study reported a particle outlet temperature of 900 °C and a receiver efficiency of ~ 75% [101]. The main challenges include scaling up the flow rate of particles, parasitic energy requirements and reliability issues with a large rotating kiln [101].

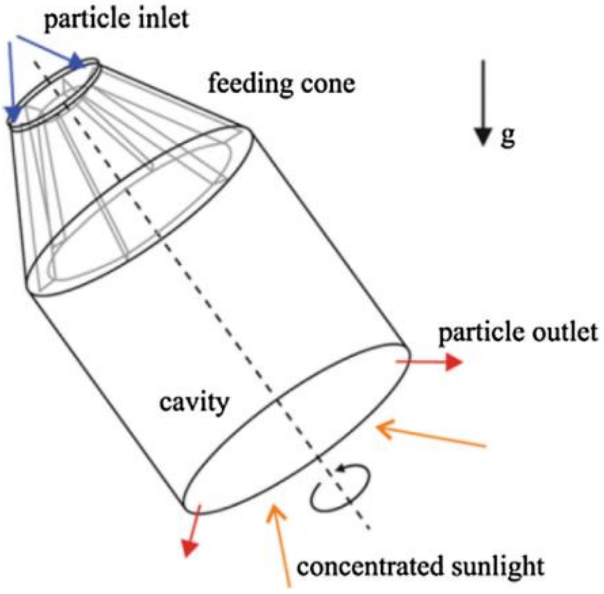

Figure 14. Schematic Of the Rotary Kiln/Centrifugal Receiver [116]

2.3.4. Fluidized Bed Receivers

Fluidization of particles for solar receivers has been proposed for several decades. It began in late 1970s and early 1980s when Flamant et al. and others tested a fluidized-bed receiver for heating and thermochemical processes [114]. These receivers can accurately control the τ_R where the particles are fluidized from the bottom with compressed air and heated at the top. Particles that were tested in this study include zirconia, silica sand, silicon carbide and chamotte [114]. For a mean flux density of 500 kW/m^2, the measured equilibrium temperature of the particles ranged from ~ 1200 °C for sand to > 1400 °C for silicon carbide. Thermal efficiencies of 20-40% were reported from these experiments [114]. The main challenge for this design is scaling up the flow rate.

Researchers at the Chinese Academy of Sciences conducted numerical and experimental studies on the thermal performance of the quartz tube receiver with silicon carbide particles [118–120]. This setup is shown in Figure 15 in which a 10 kW$_{th}$ furnace is used to irradiate the receiver with concentrated sunlight. Compressed air is sent from the bottom to fluidize the particles. Results from these experiments showed a maximum air temperature of 600 °C with <10 °C difference between the air and particle temperatures. This indicates good heat transfer from air to particles. These receivers suffer from low scalability and reliability concerns with the flow control mechanisms.

Figure 15. On Sun Testing Of a Quartz-Tube Particle Air Receiver [118]

2.3.5.Indirect Heating Receivers

There are two main types of indirect particle heating receivers, (i) gravity driven particle flow through enclosures and (ii) fluidized particle flow through tubes. The concept of ‘gravity driven particle flow through enclosures was proposed by Ma et al. [121]. Figure 16 shows the particles flow downward under gravity around a staggered array of tubes which are heated by solar irradiation [100,121]. Small scale tests indicate limited heat transfer around the tubular surfaces where the particles lose contact with the heated wall. Efficiency data and temperature rise data are not available. The main concerns for this design include scaling up of the flow rate and obtaining significant and uniform heat flux inside the tube banks. The main benefits include no loss of particles through the aperture and reduction in parasitic heat losses through the open channel [101].

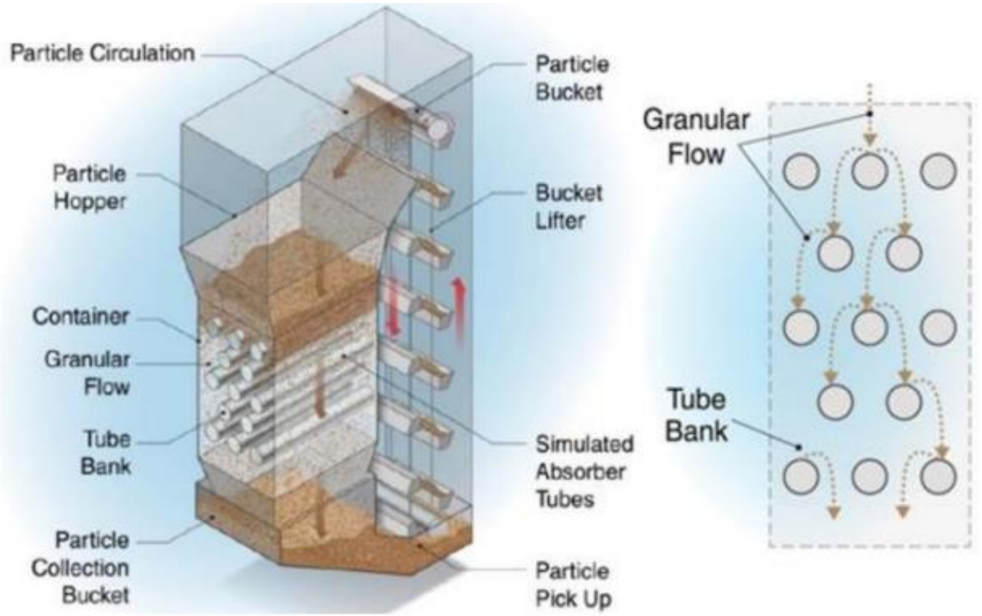

Figure 16. Schematic Of the Gravity-Driven Flow Through Enclosures Type Indirect Particle Heating Receiver Proposed By Ma Et Al. [121].

The second type of indirect particle heating receiver, i.e., fluidized bed flow through tubes, was proposed by Flamant et al. [122,123]. In the design shown in Figure 17, the particles are fluidized and forced upwards through an irradiated channel. The fluidization increases the heat transfer from the walls. A particle temperature rise of 200 °C is reported in a 50 cm long stainless-steel tube with irradiations ranging from 200-400 kW/m^2. Suspended particle temperature at the outlet reached 750 °C at a wall-to-particle heat transfer coefficient of 420-1100 W/m^2.K and particle mass fluxes of 10-45 kg/m^2.s. The main challenges with this design include scaling up of the mass flux, parasitic power requirements for particle fluidization and avoiding local hotspots in the reactor [121].

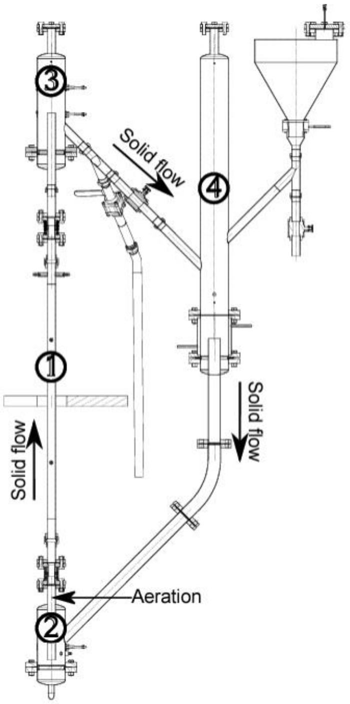

Figure 17. Schematic Of The Indirect Particle Heating Receiver (1)Solar Absorber Metallic Tube; (2) Particle Suspension Dispenser; (3) Receiving Fluidized Bed; (4) Suspension Return [121]

2.4. TCES Compatible Construction Materials

Identifying reactor materials that are compatible with common TCES materials is vital for a successful reduction reactor design. The compatibility of common high-temperature materials was investigated with common TCES materials, like manganese-iron systems and cobalt-aluminum mixed oxide systems, using thermal cycling tests [65]. Wong et al. observed the interaction between coupons of selected high-temperature construction materials with 2 selected oxides for 500 thermal cycles [65]. Four different types of coupon-oxide interactions were observed in these experiments: (i) reactions resulting in dissolution, spalling, or an extremely rough coupon surface causing cracks, (ii) reaction induced rough surfaces causing cracks in the material, (iii) surface roughening, but no cracks and (iv) minor interaction effecting the surface roughness but showed no signs of cracking. In all cases, only Inconel 625 is fully compatible. Table 4 shows the performance of various construction materials for TCES with manganese and cobalt oxides.

Table 4- Construction Material Compatibility With Manganese and Cobalt Oxide TCES [65]

Alloy	MnO_2+10%Fe_2O_3	Co_3O_4+ 5%Al_2O_3
SS 321	Fair	Poor
SS 309	Fair	Poor
SS 4340	Poor	-
253 MA	Poor	Fair
Inconel 718	Fair	Fair
9Cr-1Mo	Poor	Poor
800H	Fair	Fair
Inconel 600	Fair	Fair
Inconel 625	Excellent	Good
Hastelloy B3	Good	Poor
Hastelloy C276	Good	Poor

3. EXERGY ANALYSIS OF THE REDUCTION REACTOR

Lack of research in TCES reactors makes it difficult to choose a specific reactor concept from the literature, since each comes with their respective benefits and deficiencies. The work by de la Calle et al. [97] describes a reversible reaction path with chemical equilibrium at each infinitesimal reaction step via sufficient kinetics. A reversible reactor does not destroy exergy, which therefore is not applicable in a practical reduction reactor. Therefore, a physical reactor model that can demonstrate an approach to reversibility with a discrete reaction path, i.e., finite exergy destruction at each step, is needed.

3.1. Limitations of the Reversible Path

de la Calle et al. modeled a continuous counter-current reactor with particles entering one end and gas entering the other [97]. At each discrete point along the length of the reactor the particles and gas entering from opposite directions are infinitesimally out of equilibrium. However, it is assumed that reaction occurs to bring them into equilibrium at any given point. For the reduction reaction to occur spontaneously at a given temperature and pO_2, the Gibbs' free energy change, $dg \leq 0$, where $dg = f(T, pO_2, \delta)$. That is, in a reversible reactor., chemical equilibrium exists at each infinitesimal δ step, i.e., the Gibbs free energy change of the redox reaction Δg is infinitesimal. Since dg depends on temperature, pO_2 and δ, at chemical equilibrium, knowledge of any two of these three variables determines the third [97]. Therefore, MO_x operating under the reversible temperature profile along with sufficiently fast kinetics, maximizes $\Delta\delta$ for a given δ_{OX}, $pO_{2,in}$, maximum reduction temperature ($T_{R,max}$) and sweep ratio, $\lambda = \frac{\dot{n}N_2}{2\Delta\dot{n}O_2}$ [97], where $\dot{n}N_2$ is the inert gas molar flow rate (here N_2) and $\Delta\dot{n}O_2$ is the O_2 molar flow rate added via particle reduction.

Designing a reactor that replicates this infinitesimally changing profile would require the control of the temperature and pO_2 of infinitely many points along the reaction path. Therefore, a discrete reaction path is essential to design a practical reactor.

3.2. Discrete Reaction Path

3.2.1. Discrete Reactor Model

A discrete reaction path is one where the reaction moves from δ_{OX} to δ_R in a finite number of discrete, i.e., irreversible steps. Consider a discrete countercurrent flow reactor with n steps (Figure 18a). In Figure 18a, MO_x enters with the reduction extent $\delta_0 = \delta_{OX}$ and temperature T_{OX}. The temperature of the remaining steps is T_i (i = 1 to n). Also shown is the evolution of pO_2 and the δ change, as a result of the reduction reaction at the respective step. The main assumptions of this model are:

i. Each step is isothermal with a constant pO_2 - Ensures that the entire MO_x mass is exposed to the same environmental conditions at every step.

ii. Negligible pressure drop - Ensures that $\dot{n}N_2$ is constant at every step.

iii. The solid experiences the gas composition entering each step, i.e., there is no back diffusion or dispersion.

iv. Between each step the gas is perfectly mixed to become uniform spatially and temporally before passing on to the next step, i.e., the gas can be thought of as being fed through a perfectly stirred tank between each step.

v. No reaction between steps - Ensures that all reduction occurs at the reaction step.

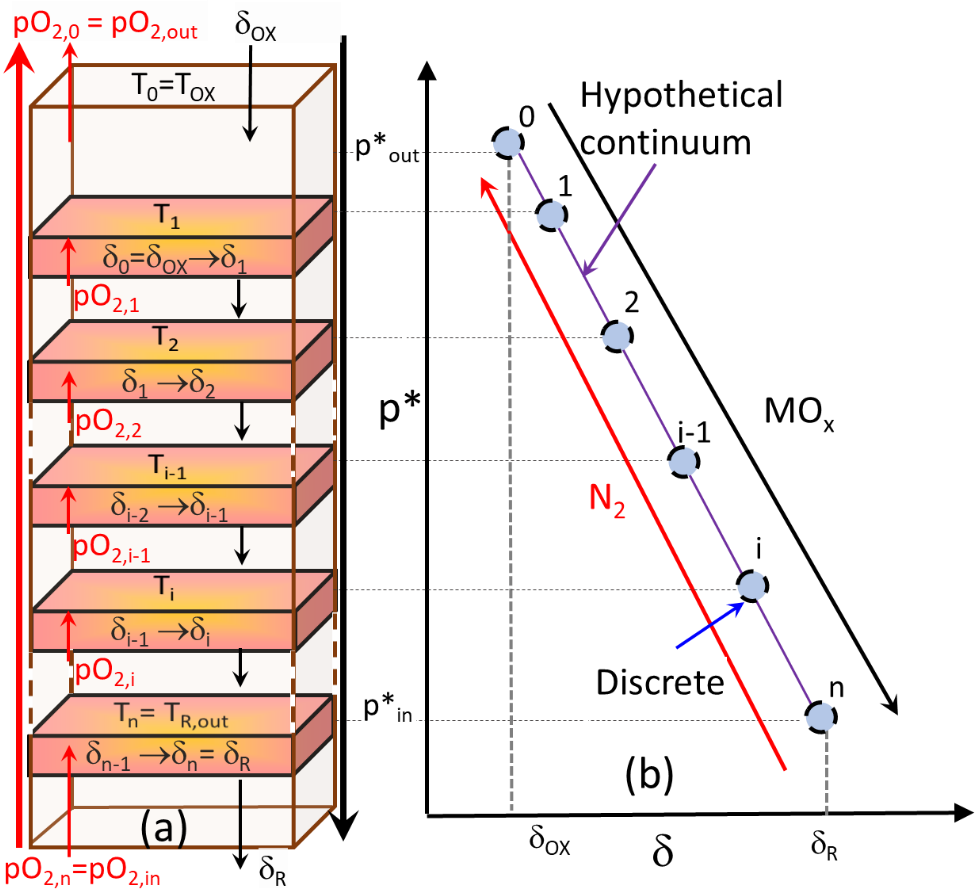

Figure 18. (a) The Discrete Countercurrent Reaction Path With N Steps, Showing the Directions Of pO_2 and δ Increase (Red And Black Arrows, Respectively). (b) Countercurrent Flow Mass Balance Representation On p*-δ Coordinate

3.2.2. Mass Conservation

Along this discrete reaction path, fixing $pO_{2,in}$, $T_{R,max}$, and δ_{OX} determines T_{OX}, $T_{R,out}$ and δ_R assuming chemical equilibrium. To determine the remaining step properties, consider the mass conservation in the discrete reactor. Assuming MO_x and the sweep gas impurity are the only O_2 sources, oxygen mass conservation at the i^{th} step is:

$$\Delta\dot{n}O_{2,i} = -\frac{1}{2}\dot{n}MO_x\Delta\delta_i \qquad \text{Eq. 13}$$

where $\dot{n}O_2$ is the O_2 molar flow rate $(\Delta\dot{n}O_{2,i} = \dot{n}O_{2,i} - \dot{n}O_{2,i-1})$. Assuming transverse O_2-N_2 homogenization and rewriting oxygen mass conservation to determine the pressure ratio $\left({p^*}_i = \frac{\dot{n}O_{2,i}}{\dot{n}N_2}\right)$ [97], gives:

$$\Delta {p^*}_i = -\frac{1}{2}\frac{\dot{n}MO_x}{\dot{n}N_2}\Delta\delta_i \qquad \text{Eq. 14}$$

Since $\dot{n}N_2$ and $\dot{n}MO_x$ remain constant along the reaction path all reaction steps exist on a hypothetical straight line (Figure 18b) with slope $-\frac{1}{2}\frac{\dot{n}MO_x}{\dot{n}N_2}$. The resulting pO_2 at the ith step is then:

$$pO_{2,i} = p_{ref}\frac{{p^*}_i}{(1+{p^*}_i)} \qquad \text{Eq. 15}$$

3.2.3.Exergy Destruction and Exergetic Efficiency

The process occurring at the ith reaction step leads to a change in Moving from the i-1th step to the ith step, the temperature and the inlet pO_2 change from T_{i-1}, $pO_{2,i-1}$ to T_i, $pO_{2,i}$. The exergy balance considering the incoming (ψ_{in}) and outgoing MO_x (solid) exergy (ψ_{out}) per mol of metal oxide is:

$$.\psi_{in,i} - \psi_{out,i} - \psi_{D,i}$$

$$= \left(dh_{MO_x}|_{T_{i-1},\delta_{i-1}} - T_{i-1}ds_{MO_x}|_{T_{i-1},\delta_{i-1}} - dh_{MO_x}|_{T_i,\delta_i} + T_i ds_{MO_x}|_{T_i,\delta_i} - T_i s_{gen}\right)\Delta\delta_i \qquad \text{Eq. 16}$$

where dh_{MO_x} and ds_{MO_x} are the specific enthalpy and specific entropy of MO_x at the given T and δ, s_{gen} is the entropy generated during MO_x heating and the reduction reaction. Eq. 16 can be rewritten as Eq. 17, since dg = dh-Tds, where dg is the change in Gibbs' free energy of MO_x at the given T and δ.

$$\psi_{in,i} - \psi_{out,i} - \psi_{D,i} = \left(dg_{MO_x}|_{T_{i-1},\delta_{i-1}} - dg_{MO_x}|_{T_i,\delta_i} - T_i s_{gen}\right)\Delta\delta_i \quad \text{Eq. 17}$$

The reaction approaching chemical equilibrium at the ith step implies that the difference between the Gibbs' free energy of the surrounding gas and MO_x $(dg_{N_2}|_{T_i,pO_{2,i}}$-$dg_{MO_x}|_{T_i,\delta_i} \rightarrow 0)$. Therefore, assuming chemical equilibrium at the ith step, the Gibbs' free energy change of the reaction at the ith step is then Δg_i=$dg_{N_2}|_{T_i,pO_{2,i}}$-$dg_{MO_x}|_{T_{i-1},\delta_{i-1}}$. Eq. 17 can now be rewritten as:

$$\psi_{in,i} - \psi_{out,i} - \psi_{D,i} = (\Delta g_i - T_i s_{gen})\Delta\delta_i \quad \text{Eq. 18}$$

Since there are no other sources of exergy apart from MO_x, the left hand side of Eq. 18 is zero. Therefore $\psi_{D,i} = T_i s_{gen}\Delta\delta_i = \Delta g_i\Delta\delta$. The total exergy destroyed due to the MO_x heating from the MO_x inlet to outlet per mole of MO_x (ψ_D) is the sum of the exergy destroyed at each step:

$$\psi_D = \sum_i^n \Delta g_i \Delta\delta_i \quad \text{Eq. 19}$$

No exergy is destroyed along an reversible path $\left(\lim_{\Delta\delta_i \to 0} \psi_{D,i} = 0\right)$. Since the MO_x enters the reaction step in a non-equilibrium state, $\Delta\delta$ will maximize if the reaction path approaches the reversible reaction path i.e., if ψ_D is minimized with respect to $\Delta\delta$. Since $\psi_{D,i}$ is equal at each step, the properties ith step can be calculated as $\psi_{D,i}$ distance away from the i-1th step on the ψ_D coordinate with respect to δ. For an integer value of n, a unique solution exists for T_i, $pO_{2,i}$ and δ_i, i =1 to n.

The total chemical exergy stored per mole of MO_x (Ω_{chem}) is:

$$\Omega_{Chem} = \sum_{i}^{n} \Delta h_i \Delta \delta_i \qquad \text{Eq. 20}$$

The total exergetic efficiency of this reactor (η_{Ex}) is then (Eq. 21)

$$\eta_{Ex} = \frac{\Omega_{Chem}}{\psi_D + \Omega_{Chem}} \qquad \text{Eq. 21}$$

where $\Omega_{chem}+\psi_D$ represents the total exergy input to the reactor.

3.3. Maximizing The Energy Storage Density With Parameter Optimization

This study analyzes the main process parameters that drive TCES costs from a reactor point of view. The parameters are: λ and $pO_{2,in}$ (which are the drivers of the N_2-associated costs), $T_{R,max}$ (which is the driver of the reactor material costs), $T_{R,out}$ and δ_R (which are the drivers of the storage container costs) and Ω (which is the driver of the MO_x costs). Analyzing their interplay can point towards several cost relevant tradeoffs. The objective here is to arrive at a recommendable set of operating conditions for the reversible path that incorporates the identified tradeoffs.

The analysis described here uses the reactor model described in section 3.2 to generate the T and pO_2 profiles. The Gibbs free energy model, presented by Miller et al., is used to determines g_{CAM28} as a function of T and δ [90,135] and the Coolprop library provides g_{O_2} as a function of T and pO_2 [136]. For all the results in this study, T_{OX} = 550 °C, resulting from reduction reactor's intended application of being in thermal equilibrium with the inlet of an sCO_2 power cycle where pre-compression sCO_2 temperature = 550 °C [137]).

3.3.1. Effect Of Inlet pO_2

First consider the effect of $pO_{2,in}$ on reversible T and mass balance profiles, as a function of δ reaction coordinate, for a fixed $T_{R,max}$ = 1100 °C (fabrication material limit) and $\lambda = 1.5$ (Figure 19 a, b, c, d). Here, the use of an infinitesimal step to ensures reversibility of the reaction path. The Reversible T increases as MO_x moves along the reaction coordinate before reaching a maximum ($T_{R,max}$), followed by a sharp decrease till $T_{R,out}$ ($T_{R,out} = T_{R,max}$ for $pO_{2,in}$ = 10 kPa). The pO_2 and δ have an almost linear relationship (log y-axis), since according to mass balance, p^* is strictly linear with δ, and not pO_2. Note that the displayed coordinates do not have any relationship with the spatial coordinates. According to Figure 19 a, b, c, and d, δ_R increases by 22% from $pO_{2,in}$ = 10 kPa to 1 kPa and 3.3% from $pO_{2,in}$ = 1 kPa to 10 Pa. Simultaneously, $T_{R,out}$ decreases by 1.2% from $pO_{2,in}$ = 10 kPa to 1 kPa and 16.72% from $pO_{2,in}$ = 1 kPa to 10 Pa. The opposing behavior of δ_R and $T_{R,out}$ with increasing $pO_{2,in}$ points towards a tradeoff between sensible and chemical energy stored to maximize Ω.

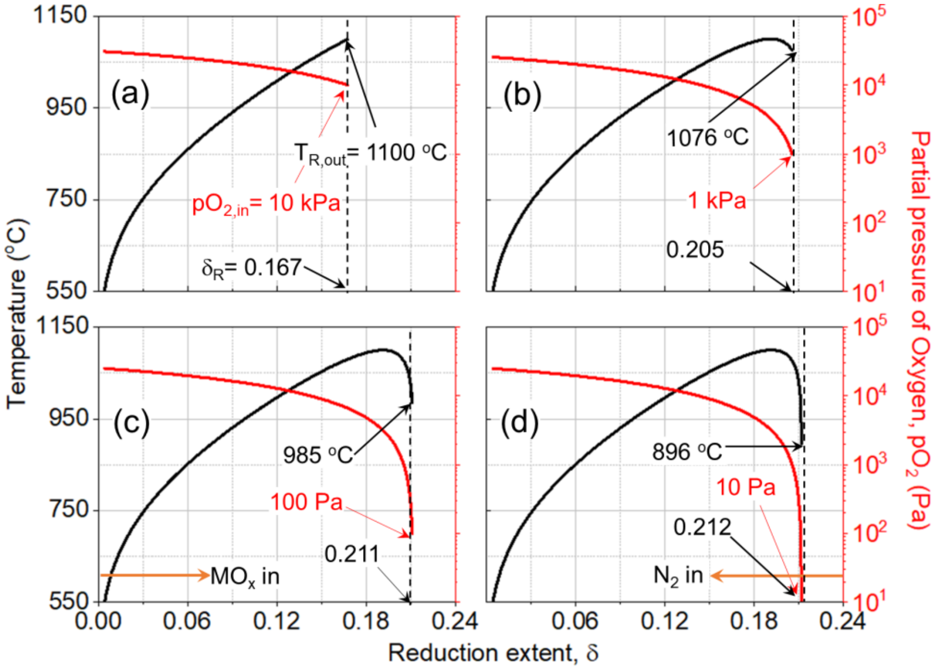

Figure 19. Reversible T and Mass Balance Profiles As a Function Of δ Reaction Coordinate, For $pO_{2,in}$ = (a) 10 Kpa, (b) 1 Kpa, (c) 100 Pa, (d) 10 Pa. T_{OX}=550 °C, $T_{R,Max}$=1100 °C and λ = 1.5.

To better illustrate this tradeoff, Figure 20 shows Ω, Ω_{chem}, and $T_{R,out}$ as a function of $pO_{2,in}$ and $T_{R,max}$, at λ=1.5. According to Figure 20, the sensible energy (total − chemical) increases with increase in $pO_{2,in}$, faster than the drop in chemical energy, causing Ω to peak when $T_{R,out} = T_{R,max}$ (Ω_{peak}). Once sensible energy peaks, Ω decreases with increase in $pO_{2,in}$ as chemical energy (δ_R) continues to decrease. For example, for $T_{R,max}$ = 1100 °C, Ω increases from 160 Wh/kg at $pO_{2,in}$ = 10 Pa to 203 Wh/kg at 3.24 kPa, followed by a decrease to 194 Wh/kg at 10 kPa.

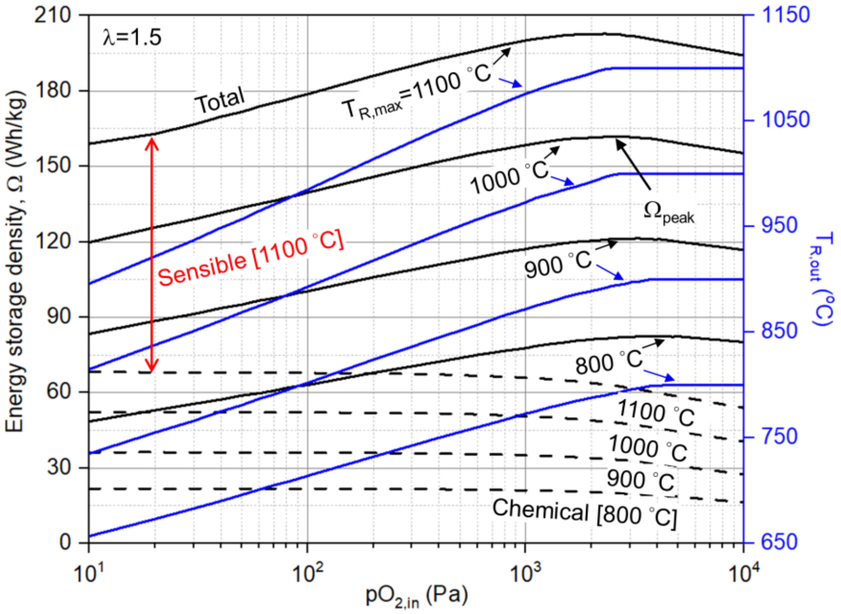

Figure 20. Ω, Ω_{Chem} And $T_{R,out}$ As a Function Of $pO_{2,in}$ and $T_{R,max}$ For $\lambda = 1.5$.

3.3.2. Effect Of Maximum Reduction Temperature and Sweep Ratio

Figure 21 shows Ω_{peak} ($T_{R,out} = T_{R,max}$) and the corresponding $pO_{2,in}$ and δ_R as a function of $T_{R,max}$ and λ. Consider the case of $\lambda = 1.5$ from $T_{R,max}$ =800 °C to 1100 °C. $T_{R,max}$ has a strong influence on Ω_{peak}, 150% increase, and the corresponding δ_R, 333% increase, and a weaker influence on the corresponding $pO_{2,in}$, 40% decrease. Now consider the case of $T_{R,max}$ = 1100 °C for λ = 1.5, 15 and 150. The selected λ range marginally overshoots the recommended range in de la Calle et al. [97] (2 to 100). Contrary to $T_{R,max}$, λ only weakly impacts Ω_{peak} (15% increase) with much stronger impacts observed on the corresponding δ_R (52% increase) and $pO_{2,in}$ (94% decrease). More constraints on λ will come from O_2-N_2 diffusion as λ determines the total O_2 that diffused out of the reactor.

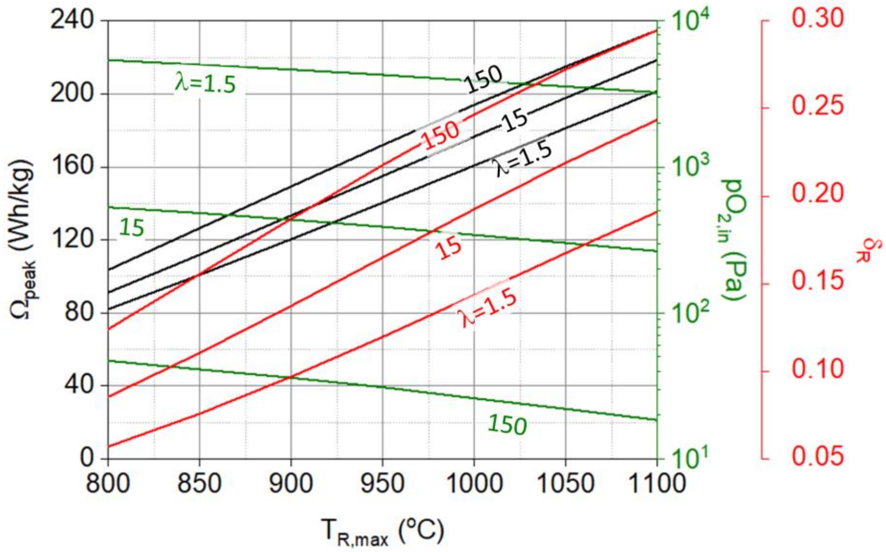

Figure 21. Ω_{Peak}, Corresponding $pO_{2,in}$ and δ_R As a function Of $T_{R,max}$ For λ = 1.5, 15, 150.

Operating near Ω_{peak} proximity has the obvious cost benefit of maximizing Ω for a given MO_x along a reaction path with a given $T_{R,max}$, T_{OX} and λ. For $\lambda = 1.5$, $pO_{2,in}$ corresponding to Ω_{peak} implies more cost benefits. For example, Ω remains within 5% of Ω_{peak} from $pO_{2,in}$ ~500 Pa to $pO_{2,in}$ = 10 kPa for the selected $T_{R,max}$ range, enabling more economical N_2 (lower purity) than typically used in previous TCES cost models [49]. Though Ω_{peak} enables multiple reactor cost benefits, it increases $T_{R,out}$ compared to lower pO_2 cases, making the storage more expensive. This tradeoff between reactor and storage costs should be incorporated while designing the TCES system.

Summarizing, the recommended operating conditions for the Reversible countercurrent flow reactor are T_{OX} = 550 °C, $T_{R,max}$ = 1100 °C, λ = 1.5 and $pO_{2,in}$ = 3.24 kPa, resulting in $T_{R,out}$ = 1100 °C, δ_R = 0.191 and $\Omega = \Omega_{peak}$ = 203 Wh/ kg.

3.3.3.Discretization Of the Equilibrium Curve

Here, the objective is to arrive at a range of n that ensures the applicability of the previous conclusions to the discrete reactor. As a sub-objective this analysis seeks further cost relevant tradeoffs from applying ψ_D minimization, along with chemical equilibrium and mass balance.

Figure 22a shows the desired Reversible path and the corresponding eleven step discretization, obtained by minimizing ψ_D. The eleven step discrete path is able to preserve all the fixed boundary conditions in the Reversible curve ($T_{R,max}$, T_{OX}, λ and $pO_{2,in}$). Therefore, all conclusions obtained in preceding sections also apply here. $|\Delta g_i|$ is maximum at $i = 1$ (16.7 kJ/mol) and decreases as MO_x traverses along the discretized reaction path, minimizing at the last step (5.9 kJ/mol at $i = 11$) (Figure 22b).

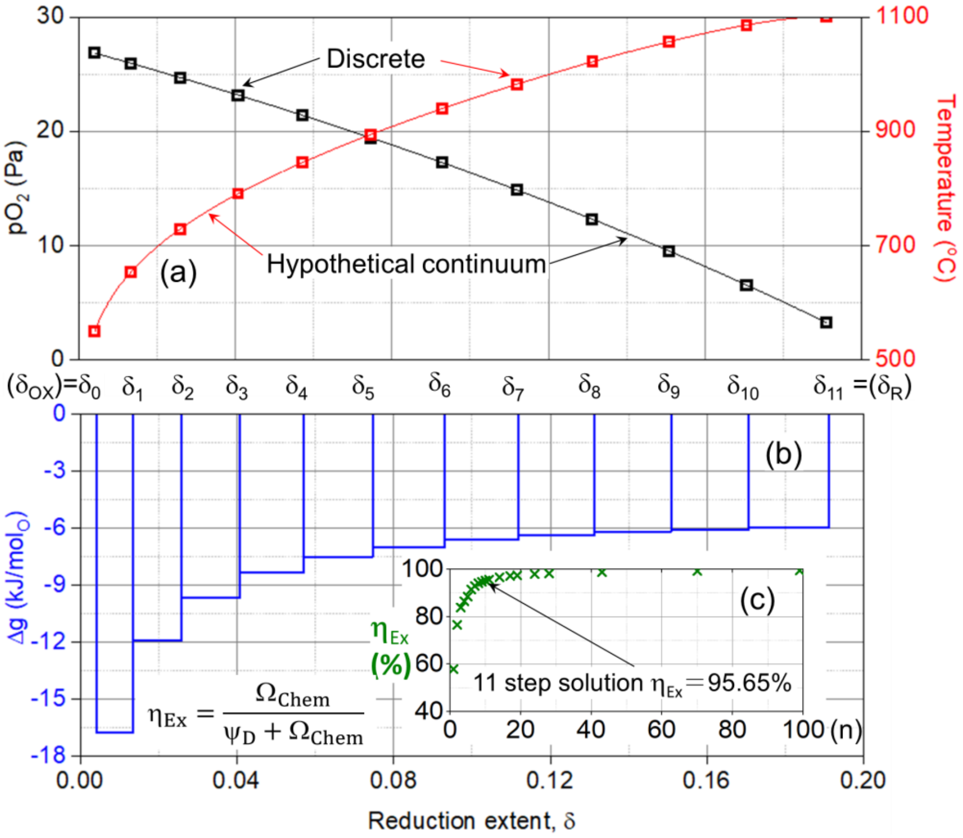

Figure 22. (a) Discretized And Reversible T And pO$_2$ Profiles As a Function Of δ For, λ = 1.5, $pO_{2,in}$ = 3.24 Kpa, $T_{R,max}$ = $T_{R,out}$ = 1100 °C And T_{OX} = 550 °C. (B) Δg As a Function Of δ Along The Discretized Reaction Path Obtained By Minimizing Q, (C) Exergetic Efficiency (η) As a Function Of Number Of Steps (N)

Along the reaction path, ψ_D quantifies the proximity of the chemical reaction to the reversible process with ψ_D ~0 being preferrable. The finite ψ_D in a discrete reactor increases the input exergy compared to the Reversible reaction path for a constant Ω_{chem}. For n = 1 and n = 2, η_{Ex} = 58% and 76%, respectively. In these cases, a significant portion of supplied exergy is destroyed in the process. Due to the large exergy destruction, reversibility (η_{Ex} = 100%) is not an appropriate assumption for cases with a small number of steps. The U.S. DOE's target for η_{Ex} = 95% for thermal energy storage systems set under the Energy storage grand challenge [138]. According to Figure 22c, n should be maximized to maximize η_{Ex} and improve equilibrium proximity, but adding more steps increases reactor mass and complexity. Considering this tradeoff between η_{Ex} and reactor mass/complexity, n = 10 (η_{Ex} = 95.2%) to 20 (η_{Ex} = 97.6%) appears reasonable, though more could be added depending on the requirement and capabilities. η_{Ex} = 95.4% for the 11-step discretization of the chosen Reversible path.

3.3.4. Identification Of System-Level Parameter Tradeoffs

In this study, Ω is modeled with the goal of minimizing the levelized costs of TCES. The most relevant metric for any energy storage technology aiming to be deployed widely and at scale is cost. Some of the important TCES cost parameters are Ω (MO_x costs), λ and $pO_{2,in}$ (via N_2 costs), $T_{R,max}$ (via reactor material costs), and $T_{R,out}$ and δ_R (via MO_x and storage container costs). The expected relationships between the chosen factors and the ZFR costs are:

i. Material costs for reactor and storage increase with $T_{R,max}$ and $T_{R,out}$.

ii. Higher inert sweep (N_2) purity increases cost.

iii. An increase in δ_{out} (chemical storage) decreases the need for a high $T_{R,out}$ (sensible storage), which decreases the storage costs, for a constant target Ω.

iv. Material throughput, reactor size and cost decrease with increasing Ω.

A reduction reactor is typically designed with consideration of the associated storage container, with known $T_{R,out}$ (output/storage temperature) and Ω. Consider Figure 23 showing several cost parameters (Ω, $T_{R,max}$ and δ_R) as a function of $T_{R,out}$ and $pO_{2,in}$. For example, $T_{R,out}$ = 800 °C and $pO_{2,in}$ = 10 Pa yield $\delta_R = 0.154$, Ω = 115 Wh/kg and $T_{R,max}$ = 980 °C. To envision the reactor-storage system tradeoffs, Table 5 shows four intersection points of Ω = 155 Wh/kg (blue) line with δ_R vs. $T_{R,out}$ (black) lines. The $pO_{2,in}$ = 10 Pa case results in the lowest $T_{R,out}$ and highest δ_R, implying more economical storage, but has higher $T_{R,max}$ and N_2 purity, pointing toward higher reactor and N_2 costs. In contrast, the $pO_{2,in}$ = 10 kPa case with $T_{R,out} = T_{R,max}$, economizes the reactor and N_2 but requires a more expensive storage bin. Among the selected options, $pO_{2,in}$ = 1 kPa case shows the highest potential for N_2 cost savings, while requiring a moderately expensive reactor and storage.

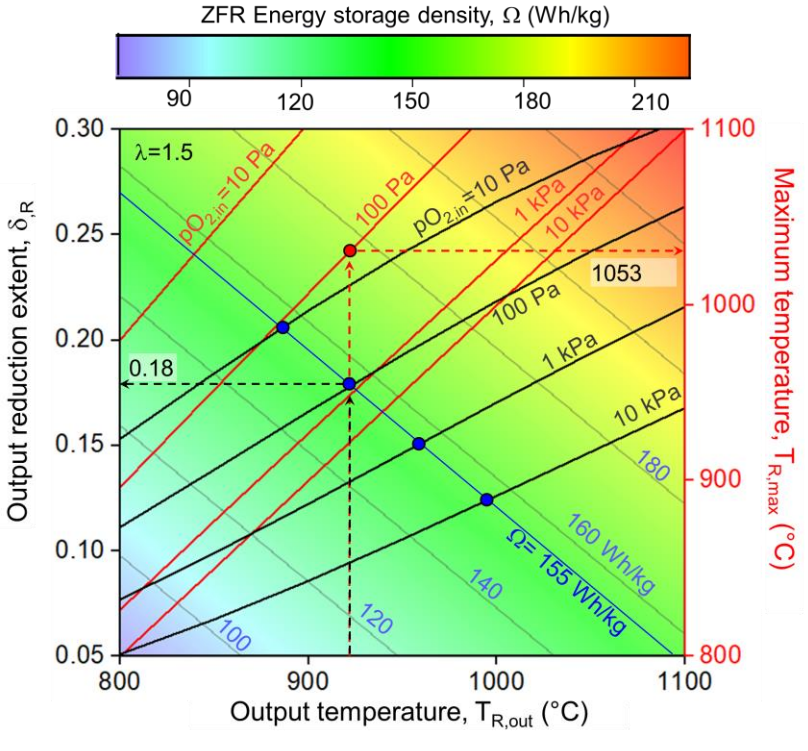

Figure 23. Dependence Of δ_R And $T_{R,max}$ On $T_{R,out}$ At Varying Values Of $pO_{2,in}$ For $\lambda = 1.5$. Contours Represent The Output Energy Storage

Table 5- Four Combinations Of Reactor Parameters That Achieve 155 Wh/Kg.

$pO_{2,in}$ (Pa)	$T_{R,out}$ (°C)	δ_{out}	$T_{R,max}$ (°C)
10	890	0.21	1,092

100	926	0.18	1,053
1k	960	0.15	986
10k	995	0.12	995

The $pO_{2,in}$ = 1 kPa case brings the reduction reactor in the temperature range of common stainless steel grades, e.g., 309 or 310. These grades are significantly less costly (retail price: \$3-\$9/kg) than SS330 or Inconel 625 (retail price \$23-\$43/kg) required for operation near ~ 1100 °C. Storage costs on the other hand do not change much, going from the best case i.e., $T_{R,out}$ = 890 °C, to this case, 960 °C where SS309 and 310 are still applicable. Finally, the δ_{out} for 1 kPa case (0.15), though lower than the best case (0.21), still meets the target W, thus not being as important as $T_{R,out}$ in overall costs. The above results offer an alternative to the commonly held assumption in the thermochemical community that N_2 purity, reaction temperatures, and $\Delta\delta$ must all be maximized in thermochemical energy storage.

4. REDUCTION REACTOR MASS TRANSFER

The equilibrium model is independent of any specific reactor and is only an analysis of the reaction path. The reactor size is primarily dependent on the O_2-N_2 diffusion parameters and scaling costs. Therefore, this chapter provides two analytical models: (i) Model to characterize the O_2-N_2 diffusion at the particle-scale and its effect on the reactor size and power density (ii) Numerical model verification of the mass transfer model trends.

4.1. Mass Transfer Model Description

4.1.1. Local Particle Environment

After understanding the physical requirements to approach chemical equilibrium along a discrete reaction path, this section provides a mass transfer model to estimate the O_2-N_2 diffusion characteristics at a reactor location where the particles and gas interact. Interestingly, ΔpO_2 between the particle surface and its surroundings ($pO_{2,surf} - pO_2$) is a measure of O_2 - N_2 mixing. $\Delta pO_2 = 0$ indicates transverse gas homogeneity. The following analysis models the dependence of O_2-N_2 mass transfer parameters on the reactor and particle dimensions. Reactor dimensions also determine the reactor power density (Π), a key cost relevant parameter.

Figure 24 shows the local particle environment as a small unit cell, assuming equal volumetric division among identical cubic particles. This analysis assumes that all O_2 evolves perpendicular to the N_2 flow. Multiple layers of particles create a particle bed of thickness Δz_{part}.

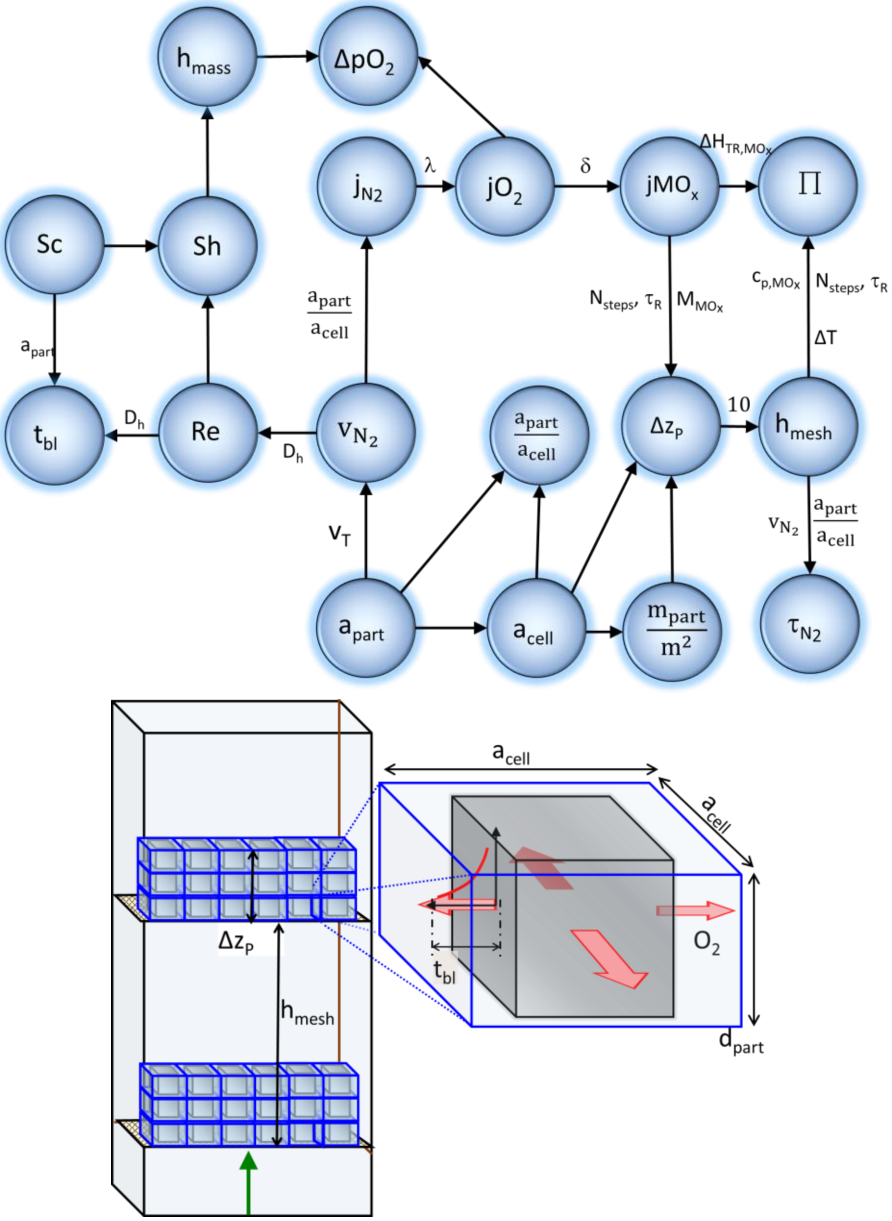

Figure 24. (Top) Mass Transfer Model Property Relationships, (Bottom) Schematic Of O_2-N_2 Laminar Diffusion In the ZFR and 3D View Of The Particle Unit Cell.

4.1.2.Model Formulation

The O_2 evolved from one particle at the reaction, where $n_{MO_x,P}$ is the number of moles of MO_x per particle is:

$$\dot{n}_{O_2,P} = n_{MO_x,P}\frac{\Delta\delta}{2\tau_R} \qquad \text{Eq. 22}$$

The resulting concentration boundary layer thickness (t_{BL}) at an entry length (L_e) is

$$t_{BL} = \left(\frac{4.91L_e}{\frac{\sqrt{2 \times Re_z}}{Sc^{\frac{1}{3}}}} \right)^{2/3} \qquad \text{Eq. 23}$$

where Sc is the Schmidt number. The resulting Sherwood number for the particle (Sh) is

$$Sh = 0.664Re_z^{\frac{1}{2}}Sc^{\frac{1}{3}} \qquad \text{Eq. 24}$$

The particle mass transfer coefficient (h_{mass}) then results from Sh, the O_2-N_2 diffusivity ($D_{O_2-N_2}$) and the particle charactersitic length (L_C),

$$h_{mass} = \frac{ShD_{O_2-N_2}}{L_C} \qquad \text{Eq. 25}$$

The ΔpO_2 required to enable this mass transfer to occur is then,

$$\Delta pO_2 = \frac{j_{O_2}}{h_{mass}RT} \qquad \text{Eq. 26}$$

where j_{O_2} is the O_2 molar flux. The number of such particles that can exist in one layer of a reactor of hydraulic diameter (D_h) is:

$$N_{P,layer} = \pi \frac{{D_h}^2}{A_{cell}} \qquad \text{Eq. 27}$$

where A_{cell} is the area of the unit cell, normal to the N_2 flow, such that $a_{cell} = 2t_{BL}+d_{part}$ and $A_{cell} = a_{cell}^2$. The pO_2 of the N_2 stream after the reaction step then becomes

$$pO_{2,out} = pO_{2,in} + \frac{P_{ref}j_{O_2}}{j_{N_2} + j_{O_2}}N_{layer} \qquad \text{Eq. 28}$$

where j_{N_2} is the N_2 molar flux and N_{layer} is the number of particle layers on the reaction step. The thickness of such a particle bed is then

$$\Delta z_P = \frac{{D_h}^2}{d_p N_{P,layer}} \qquad \text{Eq. 29}$$

Assuming that the distance between two successive steps, $h_{mesh} = 10\Delta z_P$ to allow further gas mixing and homogenization. The power density of this reactor (Π) is then:

$$\Pi = \frac{j_{MO_x}\left(c_{P,MO_x}\Delta T + \Delta\delta\Delta h\right)}{h_{mesh}} \qquad \text{Eq. 30}$$

4.2. Results

4.2.1. Analysis Of the Difference In Oxygen Partial Pressure Between the Particle Surface and Its Surroundings

This section elucidates the important results of the analytical mass transfer model. The objective here is to identify cost tradeoffs similar to the equilibrium model. Inert gas velocity (vN_2) is a vital parameter for reactor design since it determines the required N_2 volume and cost. Here, important parameters include CAM28 as the metal oxide of choice, D_h=0.01m, d_{part} = 200 μm, τ_R = 1.5 s and T = 1000 °C and $\Delta\delta$ = 0.02. According to Figure 25, ΔpO_2 decreases with increase in inert gas velocity because h_{mass} increases. With an increase in vN_2, the Reynolds number increases which increases h_{mass} and therefore, the same amount of evolved O_2 can diffuse through the N_2 stream with a much lower ΔpO_2. The vN_2 is restricted by the terminal velocity (v_T) of the respective particles. In Figure 25, h_{mass} is independent of d_{part} since the Reynold's number increases with increase in d_{part} thereby nullifying the effect of d_{part} increase. At a constant d_{part}, h_{mass} increases with vN_2 because of the increase in Reynold's number.

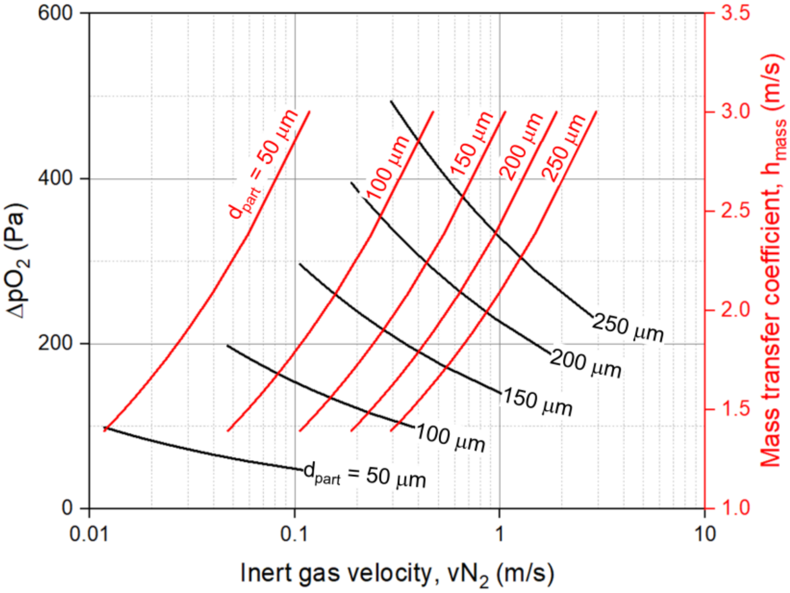

Figure 25. Dependence Of ΔpO_2 And the Mass Transfer Coefficient, h_{mass} On the Inert Gas Velocity (vN_2) At Different Particle Diameters (d_{part})

For this next part of the analysis, $L_e = d_{part}$. According to Figure 26, $pO_{2,out}$ drops off by 1-2 orders of magnitude with tenfold increase in vN_2 at a constant d_{part}. All curves are cutoff when $vN_2 = v_T$. At a constant vN_2, $pO_{2,out}$ does not depend on d_{part} since increasing vN_2 increases the N_2 molar flow rate while keeping the amount of evolved O_2 constant. At the same time, t_{BL} also decreases with increasing vN_2 at a constant d_{part}. This analysis is conducted for a single reaction step. By Adding the oxygen for all the steps and fixing λ a unique solution results for vN_2.

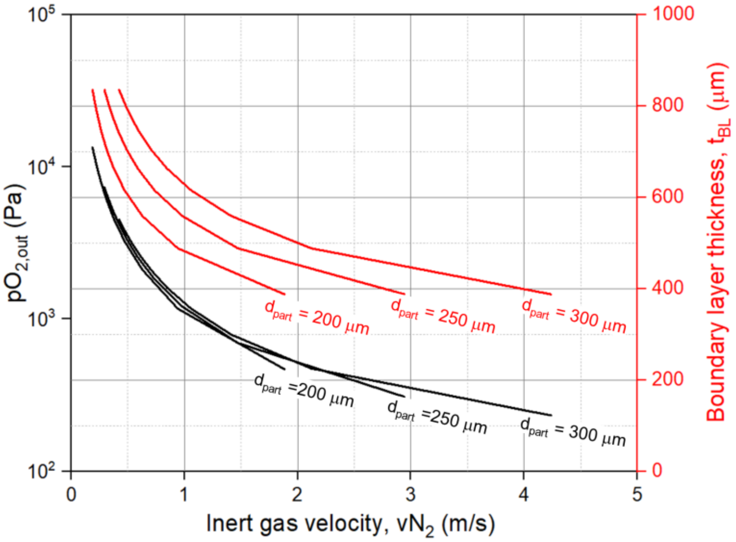

Figure 26. Dependence of $pO_{2,out}$ and boundary layer thickness, t_{BL} on the inert gas velocity, vN_2.

To understand the cost tradeoffs from Figure 25 and Figure 26, consider the case of d_{part} = 250 μm. An increase in vN_2 from $v_T/10$ to v_T, increases h_{mass} and helps improve the mass transfer The parameter ΔpO_2 represents the pO_2 invested at the reaction step to enable the mass transfer. Adding the constraint $\Delta pO_2/pO_{2,out} < 1$ yields Figure 27. The peculiar peaks occurring when $0.6<\Delta pO_2/pO_{2,out} <1$, as observed in Figure 27, are only because of the constraint that $\Delta pO_2/pO_{2,out} < 1$. All results with $\Delta pO_2/pO_{2,out} \geq 1$ have been removed. Decreasing d_{part} and vN_2 decreases $\Delta pO_2/pO_{2,out}$, thereby improving the reaction's proximity to diffusion equilibrium. Therefore, one can infer a tradeoff between h_{mass} and $\Delta pO_2/pO_{2,out}$ with respect to vN_2.

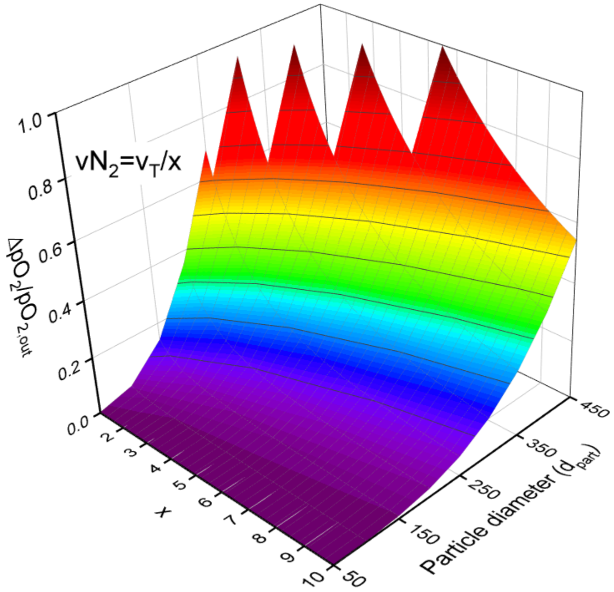

Figure 27. Dependence Of $\Delta pO_2/pO_{2,out}$ On the Inert Gas Velocity, vN_2 and Particle Diameter (d_{part}).

4.2.2. Reactor Sizing and Power Density

The next two crucial parameters under investigation in this study are as follows:

(i) Δz_p, which holds significance as it determines the spacing between consecutive steps, is related to the spacing through the relation, $h_{mesh} = 10\Delta z_p$. This value enables the estimation of the reactor power density and (ii) the packing fraction, represented as $f_p = d_{part}/a_{cell}$, another key parameter of interest. f_p determines $N_{P,layer}$, thus shedding light on the particle conveyance capabilities during the reaction step.

As illustrated in Figure 28, Δz_p exhibits a decreasing trend with an increase in d_{part}, especially when $vN_2 = v_T/2$. This phenomenon occurs because $n_{MO_x,P}$ increases with increasing d_{part}, reducing the number of particle layers required to maintain the same MO_x flow rate. Moreover, Figure 28 also indicates that f_p experiences an increase with the augmentation of d_{part}. This behavior is attributed to the fact that t_{BL} is constant as d_{part} increases when $vN_2 = v_T/2$, as evident from Figure 26. For example, in Figure 26 for

d_{part} = 200 $vN_2 = v_T/2 \sim 0.9$ m/s and for d_{part} = 300 μm $vN_2 = v_T/2 \sim 2.1$ m/s, t_{BL} = 445 μm. Since t_{BL} remains constant but d_{part} increases, f_p increases with increase in d_{part} in Figure 28. An important conclusion from Figure 28 is that to ensure sufficient mass transfer kinetics, the cross sectional area of the particle covered portion must be small compared to the x-y cross sectional area, i.e., the reactor must have low cross sectional particle density in the x-y plane.

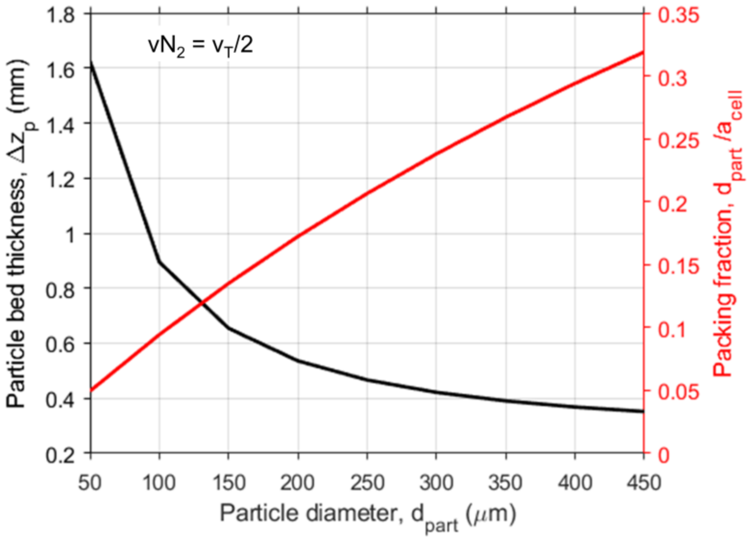

Figure 28. Particle Bed Thickness Δz_p and Packing Fraction, d_{part}/a_{cell} As a Function Of Particle Diameter, d_{part}

Finally, Figure 29 shows the reactor power density (Π) as a function of d_{part} and $x = v_T/vN_2$, where x ranges from 1 to 10. According to Figure 29, Π increases with increase in d_{part} as well as vN_2. Expectedly then, in the selected parameter range, Π maximizes at ~8.9 MW/m^3 for d_{part} = 300 μm and x = 1.4, i.e., vN_2 = 3.025 m/s. Therefore, there exists a tradeoff maintaining a small $\Delta pO_2/pO_{2,out}$ which improves equilibrium proximity and increasing Π which reduces the reactor size to minimize overall costs.

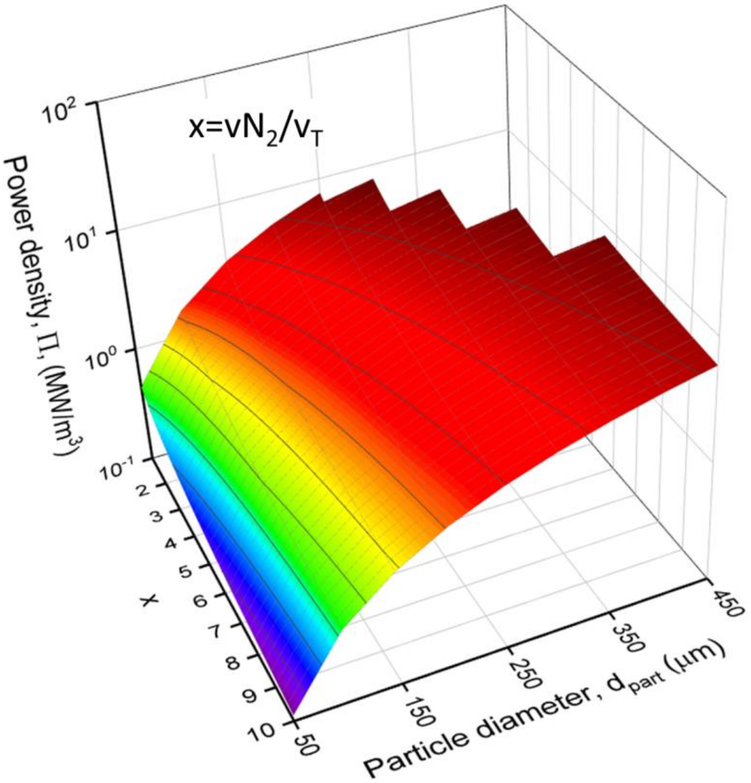

Figure 29. Dependence Of Power Density (Π) On the Particle Diameter And the $x = vN_2/v_T$

The provided mass transfer model provides important insights into the requirement for designing a reactor which can support rapid O_2-N_2 homogenization. The analysis performed identifies the reactor sizing requirements like f_p and Π for a wide range of particle diameters and gas velocities. Considering these requirements, the next chapter identifies the potential candidates that are suitable for designing a reduction reactor which approaches reversibility.

5. REACTOR DESIGN EVOLUTION

This chapter describes how the design of the reactor evolved over the course of this study and the considerations that were made to arrive at the design of the two prototypes, the α-ZFR and the β-ZFR, developed to prove the ZFR concept. Furthermore, this section describes the operation, performance, and degradation of the prototype materials and the MO_x, i.e., CAM28, particles.

5.1. Conceptual Reactor Designs

To design a thermochemical energy storage-reduction reactor (TCES-RR), it is important to start by understanding the conceptual reactor design. This helps narrow down the focus on the parts most relevant to the success of the design. Figure 30 shows the conceptual design of the TCES-RR. The different subsystem required to build a laboratory TCES-RR prototype are:

i. The hopper

ii. The particle metering mechanism

iii. The thermal reduction chamber

iv. The particle collection chamber

Each of these systems are described in the following sections

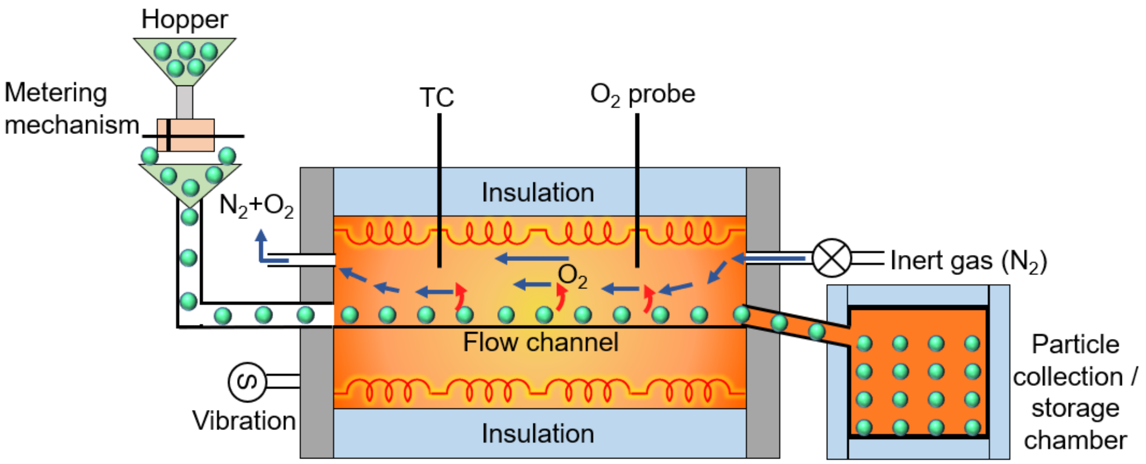

Figure 30. Conceptual Design Of the Thermochemical Energy Storage- Reduction Reactor

5.1.1.Hopper and Particle Collection Chamber

The hopper is used to store oxidized MO_x particles to be sent to the reactor for reduction. It is normally a container which may or may not contain particle preheating mechanisms. In the continuous operating system the particle collection chamber collects and temporarily stores the particles exiting the TCES-RR. At laboratory scale, it is not necessary to maintain extensive storage due to limited availability of MO_x particles. The hopper and particle collection chamber are made out of stainless steel.

5.1.2.Metering Mechanism

The metering mechanism controls the MO_x particle input flow rate to the thermal reduction (TR) chamber. The particles stored in the hopper are sent to the metering mechanism for flow control. This system should be tolerant to the moderate temperatures (< 500 °C) in its vicinity and should be simple in operation. The metering mechanism needs to be able to provide 0.1-0.4 g/s of continuous particle flow. At this flow rate, the particle density in the reactor remains low consistent with the outcomes of the mass transfer model. This value is much smaller than some of the previous studies conducted at the laboratory scale [115–117], and is required to decrease the particle-particle interactions and allow for maximum MO_x-Inert gas mixing in the TR chamber.

In the schematic of the metering mechanism shown in Figure 31, a loose fitting piston rod sweeps the particles coming from hopper into two inlets to the TR chamber. This loose-fitting piston is controlled by a computer via a reciprocating linear actuator to provide sinusoidally uniform particle flow to the TR chamber. The dimensions of the piston and channel are optimized to meet the flow rate requirements. Figure 31 also shows the rectangular piston used in the α-ZFR and the trapezoidal piston used in the β-ZFR.

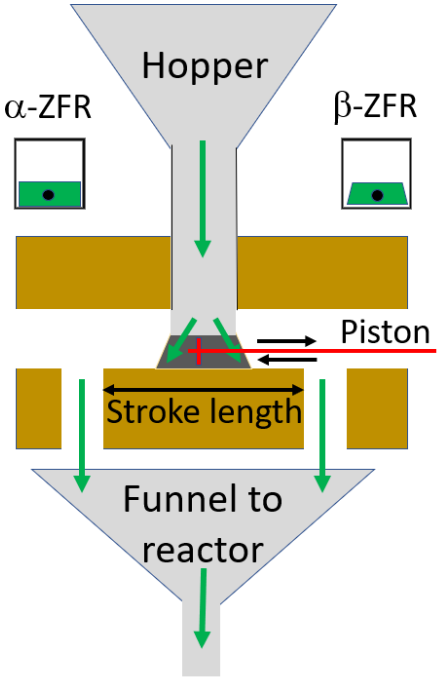

Figure 31. Schematic Of the Hopper Attached To the Metering Mechanism, Which Is An Automated Piston Cylinder That Provides Periodic Mass Input To the Reactor

Figure 32 shows the metering mechanism CAM28 supply rate for the α-ZFR and the β-ZFR Due to the oscillating piston, the output flow is sinusoidal, and the mean CAM28 supply rate depends on the round trip cycle time. The trapezoidal piston in the β-ZFR improves the output flow uniformity compared the rectangular piston by enabling shorter cycle times (Figure 32).

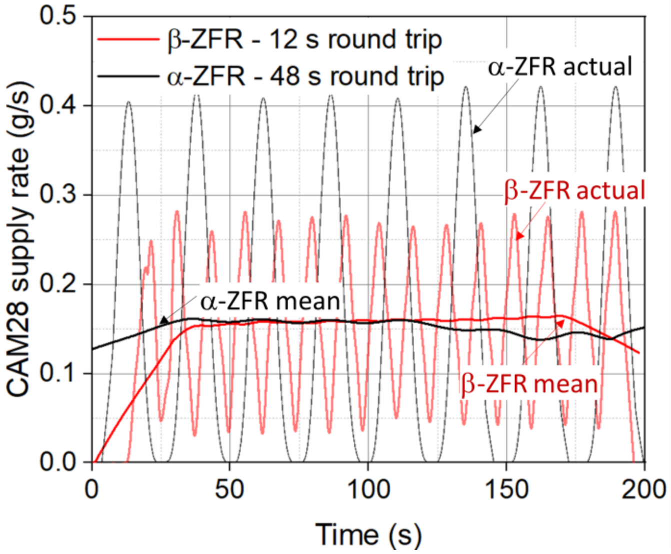

Figure 32. Comparison Of the CAM28 Supply Rate From the Two Versions Of the Metering Mechanism Used In the Two ZFR Prototypes, i.e., the α-ZFR. and the β-ZFR

5.1.3.Thermal Reduction Chamber

The TR chamber, which stands for Thermochemical Reduction chamber, is a complex system comprised of two key subsystems: the particle flow channel and the inert gas system. This chamber is designed for a specific purpose, which is to facilitate thermochemical reduction processes. Here is a breakdown of the components and processes involved:

i. Particle Flow Channel: This part of the chamber serves as a conduit for the particles undergoing thermochemical reduction. It is typically made of insulated metal to maintain a controlled temperature environment. The primary function of this channel is to expose the particles to the necessary conditions for reduction.

ii. Thermochemical Reduction: Within the particle flow channel, thermochemical reduction occurs. This process involves subjecting the particles to elevated temperatures, which leads to chemical reactions.

iii. Evolved O_2 Gas Removal: As part of the thermochemical reduction, oxygen gas is released. To prevent interference with the reduction process, the O_2 gas is carried away from the chamber using an inert carrier gas.

iv. Countercurrent Inert Gas Flow: To maximize the rate at which O_2 carried away in the inert gas and the reduction efficiency, it is essential to establish a countercurrent flow of inert gas. In other words, the inert carrier gas is introduced in a direction opposite to the flow of particles. This helps ensure efficient removal of O_2 gas and effective reduction of the particles.

v. Inert Gas Selection: The choice of inert gas is crucial. It must be non-reactive with any material present in the reactor to prevent any unintended reactions or contamination of the product. Common inert gases used in such processes include N_2 and argon (Ar). N_2 was selected as the inert sweep gas for this study.

vi. Integration of Electrical Heating: The design of the reactor is a critical consideration. Given the reported problems with using Concentrated Solar Power (CSP) for particle heating, such as hot spots and non-uniform heating, the chosen reactor design should be capable of electrical heating [110]. This allows for precise control of the temperature, which is essential for thermochemical reduction processes. However, the design should also retain the potential for CSP integration, indicating flexibility in heating methods.

In summary, the TR chamber is a specialized system for conducting thermochemical reduction processes on particles. It relies on two essential subsystems: the particle flow channel and the inert gas system, with specific design considerations to ensure efficient and controlled reduction while minimizing unwanted reactions and maintaining the potential for various heating methods, including electrical and CSP integration.

5.1.4.Selection of Reactor Concepts

The selection process for a reactor concept involves several key steps and criteria:

i. Scalability: The chosen reactor concept should demonstrate high potential for scalability, meaning it can be effectively adapted for larger-scale applications.

ii. High MO_x-N_2 mixing: A key criterion for reactor selection is the presence of MO_x-N_2 mixing. This interaction is crucial to maximize the O_2-N_2 homogenization and ensuring sufficient gas diffusion kinetics and determined using numerical/CFD models.

iii. Prototype Testing: If numerical models indicate favorable O_2-N_2 homogenization, a simplified representative prototype of the candidate reactor design is constructed using steel or other suitable materials. This representative prototype is then tested to assess its τ_R characteristics.

iv. Tunable τ_R Capability: The reactor design should preferably offer a tunable τ_R capability. This means that the time constant, which can be related to the rate of chemical reactions or other important processes, can be adjusted, or controlled to meet specific requirements.

v. Vibration Control: Vibration is used to actively enable particle flow and control τ_R in the reactor. This dynamic control is essential for maintaining the desired reduction performance of the particles.

vi. Subsystem Integration: The chosen reactor design should have the flexibility to incorporate additional subsystems beyond the particle flow channel and the inert gas system without requiring significant modifications. This adaptability is important for accommodating various process requirements and evolving needs.

Reactor selection is based on a combination of factors, including efficient particle-gas interaction, the ability to control τ_R, and the adaptability of the design to accommodate different subsystems. These criteria are essential for achieving the desired reduction performance in thermochemical processes.

5.2. Oxygen Nitrogen Homogenization

This section details a CFD model to analyze the O_2-N_2 homogenization that can aid in selecting a reactor design concept. This model is further used to verify a trend from the analytical mass transfer model to gain more confidence in the results. Literature shows that too much control over τ_R, e.g., rotary kilns or fluidized bed reactors, significantly affect the reactor scalability [101]. The obstructed flow reactor and its different iterations offer the most interesting possibilities for controlling τ_R by engineering the obstructions, while maintaining the gravity driven particle flow of the free falling reactor. Thus, in this study three reactors that impede the free fall of particles using mechanical obstructions, the inclined plane concept used in STInGR [59] (IP), the obstructed flow reactor (OFR) from Sandlin et al. [139], and the novel concept proposed in this study, i.e., the Zigzag flow reactor (ZFR), are analyzed to narrow down the concept most suitable for this application. An important reason for including the IP in this analysis is its utilization in the most recent attempt at designing a TCES reactor, i.e., STInGR. While the OFR and the ZFR offer the opportunity for uniform cross-sectional particle distribution, the IP does not. This helps to highlight the importance of uniform cross-sectional particle distribution, an assumption in the analytical diffusion model, and high MO_x-N_2 mixing.

5.2.1. Numerical model formulation

This section evaluates the effect of MO_x-N_2 mixing using 2-D CFD models of the candidate reactor geometries. High MO_x-N_2 mixing is essential for rapid O_2-N_2 homogenization. In this model, 2-D simulated particles release O_2 into flowing N_2, inside geometries representing the inclined plane scheme (IP) [59], the obstructed flow reactor (OFR) [101] and the ZFR. Figure 33a shows the geometry and boundary conditions for the CFD models of the IP, the OFR and the ZFR. The flow channel for all three cases is 300 mm x 25 mm. N_2 enters with a velocity of 2 cm/s with a pO_2 of 10 Pa and exits at the pressure outlet. The model considers particles ($d_{part} = 500\ \mu m$), spaced by 1 mm, as stationary oxygen concentration sources. For the IP (due to the absence of discrete steps like the OFR and the ZFR), the model assumes a group of twelve consecutive particles have the same O_2 source concentration. In the OFR and the ZFR, constant O_2 source concentration particles are located at each mesh location. The angle of incline for the ZFR meshes is 5°. The mass balance line equation illustrates an inversely proportional relationship between the $pO_{2,surf}$ and the reaction coordinate in a countercurrent flow reactor [97]. To simulate the increasing reaction coordinate, and therefore how the O_2 is released in the reactor, this model assumes static particles with fixed δ and $pO_{2,surf}$, which represents steady state particle flow. The static particles are grouped in 8 longitudinal sections which share the same reaction coordinates ($pO_{2,surf,i} = 2 \cdot 10^i$ Pa, i = 8 to 1). The position of these groups of particles in the channel for both reactors can be seen in Figure 33.

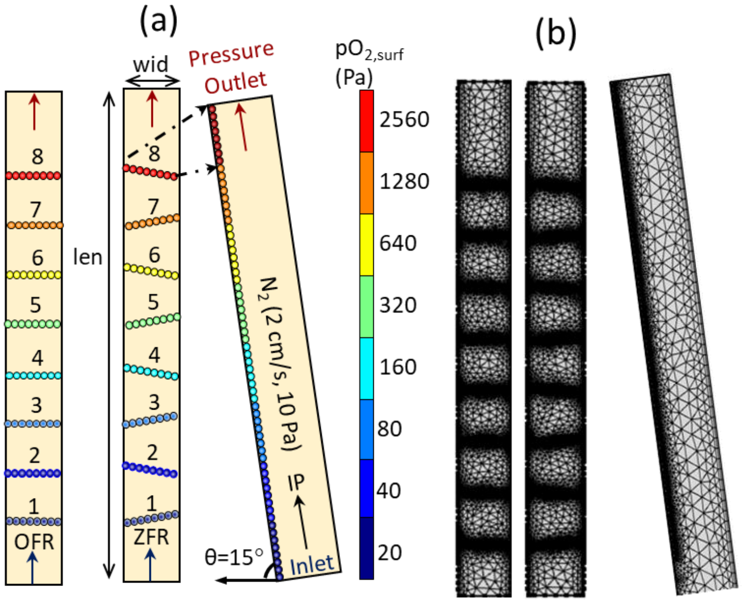

Figure 33. Geometry, Initial Conditions, Boundary Conditions and Computational Mesh For pO_2 distribution Modeling Of the IPR (θ Not Representative, ~15°), the OFR and the ZFR

The model evaluates steady state pO_2 throughout each of the reactor domains. The target is to identify a reactor design which maximizes the oxygen homogenization along the reactor cross section to prevent inconsistent $\Delta\delta$. Figure 33b shows a computational mesh for the IP, the OFR and the ZFR and Table 6 shows the corresponding computational mesh statistics. The computational mesh is refined in a way to populate more elements closer to the particles.

Table 6- Computational Mesh Statistics For The IP, OFR And The ZFR

ID	Number of elements	Average element quality
IP	11,369	0.74
ZFR	17,491	0.76
OFR	18,044	0.76

5.2.2. Analyzing the O_2-N_2 Homogenization

Now to evaluate O_2-N_2 homogenization in the ZFR in comparison to the IP scheme and the OFR, Figure 34 shows the steady state pO_2 distribution resulting from static O_2 sources and N_2 flow. It is evident that the counterflow-crossflow interaction in the ZFR and the OFR creates significant MO_x-N_2 mixing, resulting in rapid transverse O_2

homogenization. Conversely in the IP scheme, poor MO_x-N_2 mixing leads to O_2 accumulation over the particles and hinders particle reduction. The resulting transverse O_2 inhomogeneity decreases N_2 utilization. This result illustrates the difficulties in achieving diffusion equilibrium in the IP scheme, including satisfactory δ and sweep gas utilization without sufficient MO_x-N_2 mixing. Figure 34 shows that both the OFR and the ZFR enable sufficient O_2-N_2 homogenization to meet the gas homogenization requirements of the equilibrium model.

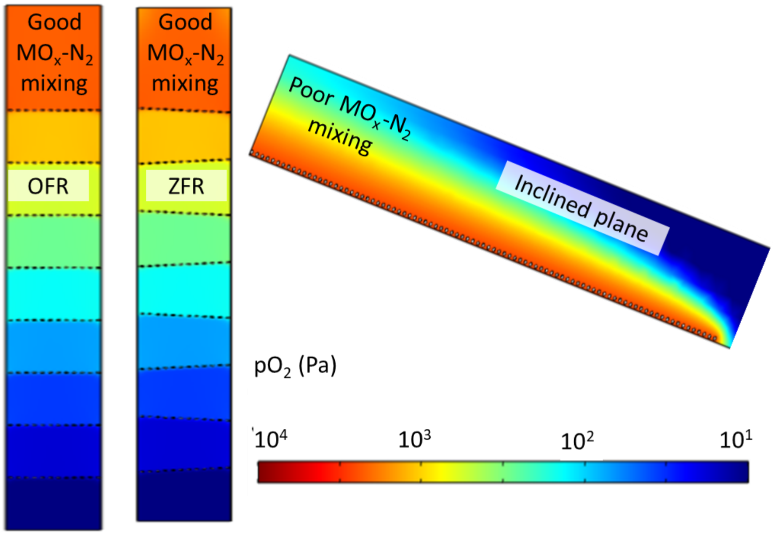

Figure 34. Comparison Of Steady State pO_2 Distribution In the OFR, the ZFR and the IP Scheme. the Poor Particle-Gas Mixing In the IP Scheme Causes O_2 Accumulation Above the Particles And the High Particle-Gas Mixing In the ZFR and the OFR Causes Rapid Transverse O_2 Homogenization Perpendicular To N_2

5.3. Reactor Residence Time

This section details the experiments conducted to analyze the residence time (τ_R) in the OFR and the ZFR according to flow channel requirements. Both these reactors (not IP) offer sufficient MO_x-N_2 mixing to satisfy the requirements of the equilibrium model (Figure 34). The selection process between the Open Flow Reactor (OFR) and the Zero Flow Reactor (ZFR) was based on experiments measuring the characteristic time constant, represented as τ_R. The objective of these experiments was to identify which of these two reactor geometries offers a sufficiently high τ_R while also ensuring effective particle-gas mixing. The primary goal of these experiments was to determine which reactor geometry, OFR or ZFR, provides a τ_R that allows enough time for the sand particles to equilibrate with the surrounding temperature and oxygen partial pressure (pO_2). Equilibrium in these conditions is important for thermochemical reduction processes. The experiments used 5 g of sand particles with a particle size distribution in the range of 50 μm to 200 μm. The sand particles were instantaneously added to a hopper located at the top of each of the reactor prototypes. A load cell placed at the exit of each prototype recorded the mass accumulation of particles as they passed through the reactor.

i. OFR Prototype: In the OFR prototype (Figure 35a), particles flowed through a vertical channel that was 300 mm long. Eight vertically stacked horizontal metal meshes (with a mesh size of 300 μm and a 53% open area) obstructed the free fall of particles. The channel was suspended from metal wires connected to a fixed support.

ii. ZFR Prototype: In the ZFR prototype (Figure 35b), particles also flowed through a vertical channel, but it was 304.8 mm long. Eight vertically stacked slightly inclined (~15°) particle-opaque metal meshes (with a mesh size of 50 μm and a 43% open area) were used to influence particle flow. A vibration motor was employed to facilitate particle flow in this reactor.

In both the OFR and ZFR prototypes, the same vibration motor was located at the same relative flow channel location. Vibration is a method used for actively controlling τ_R in the reactor, as mentioned earlier. The parameter $\tau_{R,unit}$ was used to characterize τ_R. It represents the time taken by the first particles to exit the reactor per unit reactor height. To ensure the reliability of the results, five separate experiments were conducted, and the reported results represent the average of these experiments.

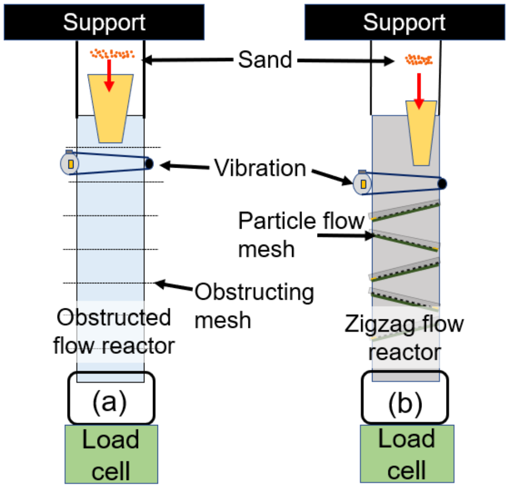

Figure 35. Schematics Of the (a) Obstructed Flow Reactor (OFR) (b) Zigzag Flow Reactor (ZFR) Prototypes Used For the τ_R Experiments

Figure 36 illustrates the characteristic time constant per unit reactor height, τR,unit, in both the Zero Flow Reactor (ZFR) and the Open Flow Reactor (OFR). The ZFR exhibits the highest $\tau_{R,unit}$. This is primarily because of the significantly increased path length created by the vertically stacked, particle-opaque, inclined mesh setup. The longer path in the ZFR results in a $\tau_{R,unit}$ that is fifteen times greater compared to a free-fall reactor. This extended residence time is crucial for achieving the desired thermochemical reactions within the reactor. The significantly higher $\tau_{R,unit}$ in the ZFR, compared to free-fall conditions, justifies the cost of adding obstructions in the form of stacked inclined meshes. These obstructions increase the residence time, allowing particles to interact with the gas phase for a more extended period. In contrast to the ZFR, the OFR has a $\tau_{R,unit}$ that is approximately half of that in the ZFR. This is due to the fact that particles smaller than the mesh opening size in the OFR experience little obstruction to free fall, resulting in shorter residence times. The ZFR not only provides high $\tau_{R,unit}$ but also offers simplified control over $\tau_{R,unit}$. This control can be achieved by changing the number of meshes or by adjusting the angle of mesh incline. This flexibility in controlling $\tau_{R,unit}$ is advantageous for tailoring the reactor to specific process requirements. The results indicate that only the ZFR can provide sufficient residence time and effective particle-gas mixing at each reaction step to approach reaction equilibrium. This is a critical factor in thermochemical processes where achieving the desired reaction outcomes relies on maintaining equilibrium conditions. In summary, the ZFR is preferred due to its significantly higher $\tau_{R,unit}$, which offers the potential to approach reaction equilibrium. The controlled and tunable $\tau_{R,unit}$ in the ZFR, achieved through obstructions and inclination adjustments, makes it a suitable choice for the TCES-RR.

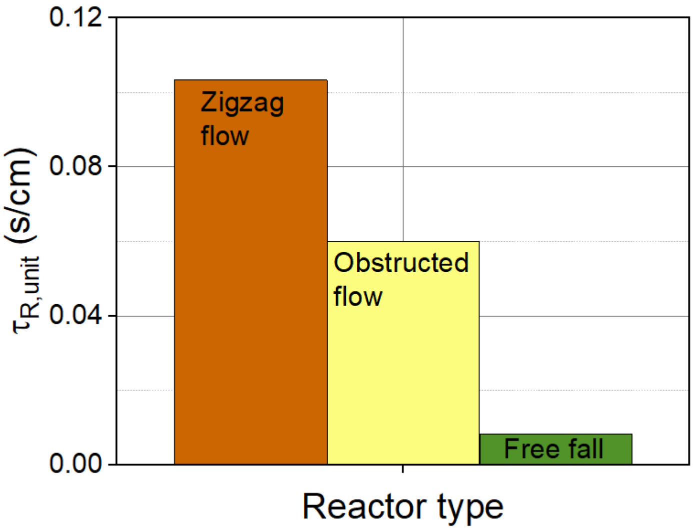

Figure 36. Minimum Residence Time Per Unit Reactor Height ($\tau_{R,unit}$) For the ZFR, the OFR and the Free Falling Reactor

5.4. Zigzag flow reactor concept summary

In the ZFR, depicted in Figure 37a, MO_x particles and gases flow through a vertical, electrically heated, externally vibrated channel. The oxidized particles enter from the top of the channel and flow downwards, while the (inert) gas enters from the bottom of the channel and flows upwards. To prevent particles from free-falling and thus increase τ_R, a series of meshes have been installed inside the channel that restrict their vertical free movement but allow for the uniform upward movement of gas. The meshes are slightly inclined with respect to the horizontal ($\theta \sim 15°$), which, combined with vibration, prevents particles from getting stuck, allowing them to flow downward due to gravity. Each mesh has two sections as shown in Figure 37b. The first section (> 80% of the area) is a particle-opaque fine-mesh with square openings, where the square side (a_{mesh}) is smaller than the smallest diameter of the particles ($d_{part,min}$). The second section, a particle-transparent coarse mesh ($a_{mesh} > d_{part,max}$), provides structural support to the fine mesh and enables particle through-flow. The particle-transparent section of the mesh is placed at opposite ends of adjacent meshes, ensuring particles to follow a zig-zag downward trajectory in the channel. For both meshes the open area fraction is high (~ 40 –50%), minimizing the pressure drop and facilitating crossflow-counterflow particle-gas interaction. Mesh length and inclination control τ_R along the ZFR length and the reduction reaction path. For the purposes of particle flow modeling, this study assumes that under vibration, particles form thin, agitated, dilute particle beds above each mesh, of thickness Δz_{part}.

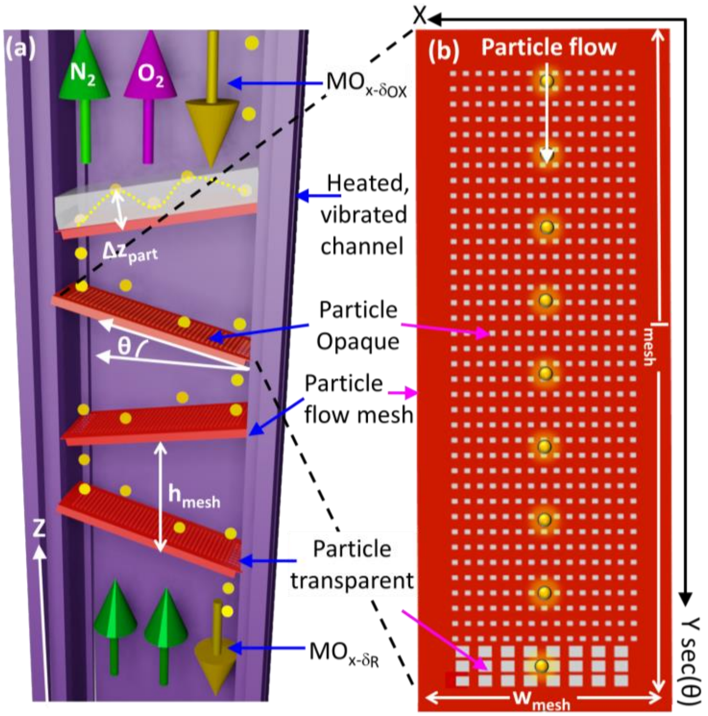

Figure 37. (a) ZFR Cross-Section With Particle and Gas Flow Directions. (B) Enlarged Particle Flow Mesh View. Note Particle Opaque and Particle-Transparent Sections, θ = Incline Angle ~ 15

5.5. First Laboratory Prototype: α-Zigzag Flow Reactor

The ZFR concept was proved using a stainless-steel laboratory prototype (initial experiments determined τ_R) ensuring that the particles spend sufficient time at each mesh. In this experiment, 5 g of CAM28 particles were dropped into a 12-mesh ZFR prototype and monitored the ensuing output flow with a load cell (US Solid precision balance lab scale, readability 0.01 g, linearity ± 0.03 g). In the ZFR context, τ_R is defined as the ratio of the time taken by first particles reaching the load cell ($t_{inlet \rightarrow exit}$), and the total number of meshes (N_{mesh}) $\left(\tau_R = \frac{t_{inlet \rightarrow exit}}{N_{mesh}}\right)$. Limited research on CAM28 kinetics makes it challenging to determine the target value for τ_R. While modeling the heat transfer and diffusion kinetics is possible, accurately estimating O^{2-} ion mobility and surface reaction rates is challenging. Nonetheless, the small Biot number of ~ 75 μm particles (< 0.1) and a high degree of particle-gas mixing suggest that internal heat transfer and O_2-N_2 diffusion kinetics occur rapidly, with characteristic times << 1 s similar to previous work [140]. To account for the unknown O^{2-} ion and surface reaction kinetics this study conservatively estimated a target $\tau_R = 2$ s/mesh. To achieve this τ_R, the ZFR mesh was co-designed l_{mesh} (77 mm), mesh inclination (~15°) and the vibration frequency and intensity.

In the proof-of-concept prototype (Figure 38), thermal reduction took place inside a 75 mm x 25 mm x 600 mm u-channel with 12 meshes of $h_{mesh} = 25$ mm, inclined at $\theta = 15°$. A fine mesh ($a_{mesh} = 50$ μm, 41% open area) and the coarse mesh ($a_{mesh} = 200$ μm, 53% open area) are suitable for $d_{part} = 50$-150 μm. N_2 flowed in the +z direction, counter-cross to the particles. The flow channel and meshes were made of stainless steel 304. External heaters embedded in insulating firebrick heat the channel with MO_x and N_2 to the desired reaction temperature. The heaters led to a maximum reduction temperature ($T_{R,max}$) of 900 ± 10 °C and a reactor outlet temperature ($T_{R,out}$) of 823 ± 15°C. The output particle flow was quenched by indirect air cooling to preserve δ_R and then stored under reduced pO_2. A mass flow controller supplied 2000 sccm ± 0.6% of N_2, while an O_2 probe continuously monitored the exit pO_2. The oxygen sensor used for this experiment was GPR-1500 GB glove box ppm oxygen transmitter (range- 0-25%, accuracy = ± 200 Pa). After the end of the experiment, $\Delta\delta$ of 3 random particle samples (~20 g each) were calculated from their masses post-reduction (m_R) in the ZFR and subsequent reoxidation at 620 °C for 30 min (m_{OX}) using Eq. 31, where M_O is the O molar mass and f_{reac} is the reactive fraction. The unreactive MO_x phase decreases the reduction-caused mass loss and need to be accounted when calculating $\Delta\delta_{OX}$. The CAM28 sample used in this experiment has an $f_{reac} = 0.67$, calculated by comparing the TGA of available CAM28 particles with pure CAM28.

$$\Delta\delta_{OX} = \frac{\frac{m_{OX} - m_R}{m_{OX}}}{f_{reac}\,\frac{M_O}{M_{MO_x}}} \qquad \text{Eq. 31}$$

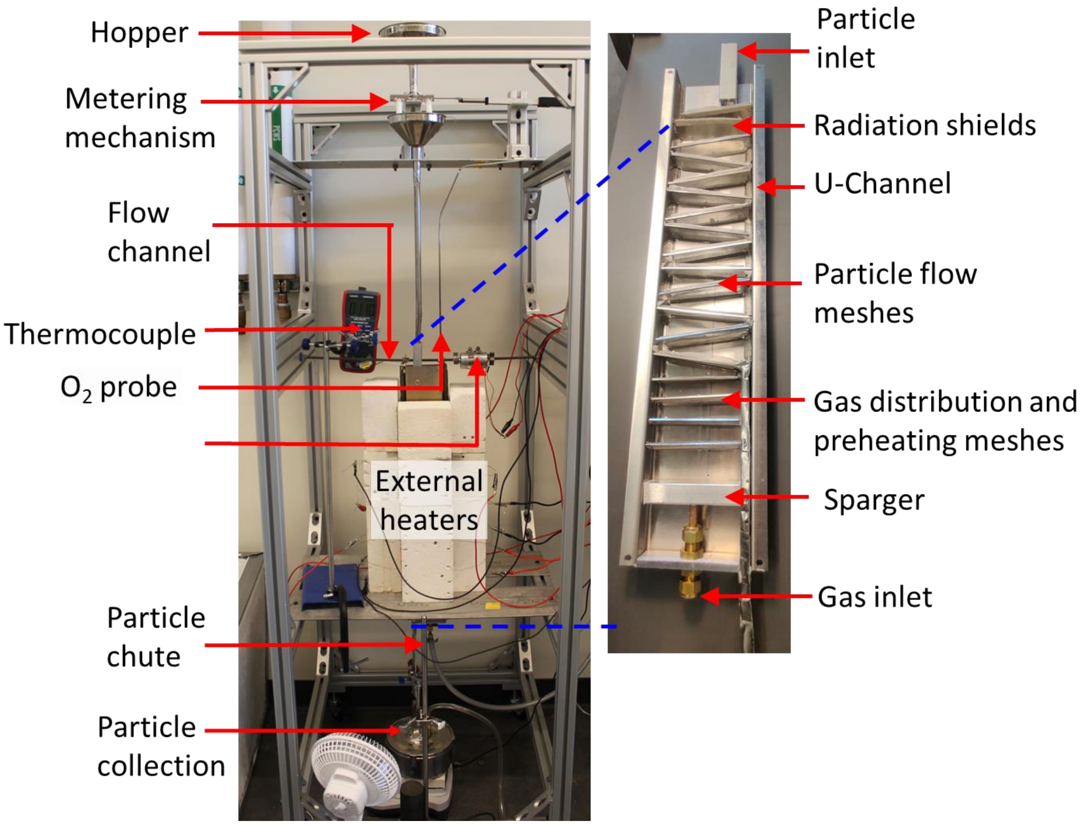

Figure 38. The α-ZFR Laboratory Prototype With Expanded View Of the Flow Channel

5.5.1.α-Zigzag Flow Reactor Operation

This section summarizes the typical operation observed in the first laboratory prototype: the α-ZFR, replicated several times in > 10 h of total runtime. Figure 39 illustrates the type of data collected in the α-ZFR experiment. In the experiment, the CAM28 is supplied at a modulated input (0.016 Hz) with the mean input mass flow rate, $\dot{m}_{CAM28,in}$~ 0.16 g/s. Figure 39 also shows the mean CAM28 output mass flow rate ($\dot{m}_{CAM28,out}$) along with the pO_2 measured near the particle inlet. After an initial transient (~ 1 – 2 min.) a steady $\dot{m}_{CAM28,out}$ ~ 0.16 g/s (= $\dot{m}_{CAM28,in}$) is established. Shortly after observing particles exit the reactor, pO_2 measured near the particle inlet (i.e., N_2 outlet) begins to rise and reaches a steady state ~ 8.5 kPa. The steady state pO_2 modulation frequency equals the CAM28 supply rate frequency (0.016 Hz). After exhausting the particle supply, the particle flow rate drops rapidly, followed by pO_2, which returns to background level at the end of the experiment. The output particle flow transient behavior mirrored in the detected O_2 signal indicates that the O_2 originates from CAM reduction only, validating the equilibrium model assumption. In this experiment, The α-ZFR prototype achieved Ω = 90 Wh/kg, and a $\Delta\delta$ fivefold that of previous TCES work at similar temperatures [96]. For the prototype, the expected $\delta_R = 0.12$ ($T_{R,out}$ = 823 °C, $pO_{2,in}$ =300 Pa) while the observed $\Delta\delta = 0.057 \pm 0.0005$ indicates some potential internal reoxidation due to the presence of local cold spots and/or air ingress.

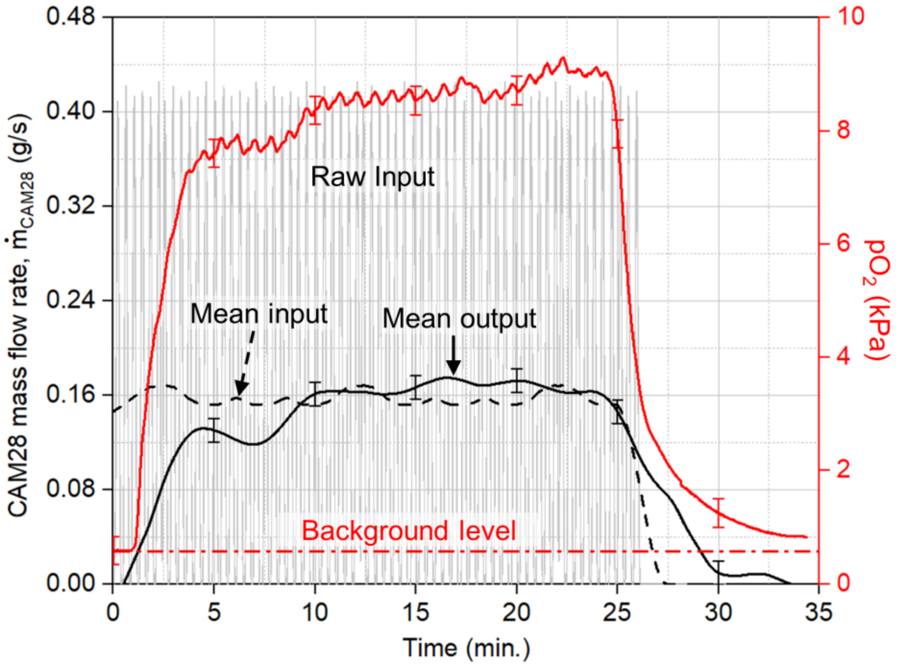

Figure 39. CAM28 Supply Rate (Grey), Overlayed Lowess Smoothed Mean Supply Rate (Black Dotted), Measured Output CAM28 Mass Flow Rate (Black) and pO_2 Measured At Particle Inlet (Red) As a Function Of Time. The pO_2 Measured Closely Follows the Output Particle Flow Indicating That O_2 Originates From the Particles, Proving the ZFR Concept

5.5.2.Effect of CAM28 Supply Rate

Figure 40 illustrates the results of varying the CAM28 supply rates while maintaining the N_2 flow rate (2000 sccm) and temperature profile ($T_{R,max}$ = ~ 905 °C, $T_{R,out}$ = ~ 813 °C). In each case the total amount of CAM28 particles was 250 g, resulting in different lengths of the experiment. For nominal input mass flow rates of ~ 0.16 g/s and ~ 0.24 g/s, the CAM28 exit mass flow rate achieves a flat profile, which is not observed in the case of ~ 0.36 g/s. The pO_2 at the gas exit reached a constant value of ~ 8000 - 9000 Pa for mass flow rates of ~ 0.16 g/s and ~ 0.24 g/s and ~ 12000 - 13000 Pa for the case of ~ 0.36 g/s. The associated reduction extents measured (i) using the pO_2 at the reactor exit, $\Delta\delta_{pO_2}$ (Eq. 32) and (ii) using the reoxidation weight gain of the reduced sample, $\Delta\delta_{OX}$, are shown in Table 7. In Eq. 32, $pO_{2,t}$ is the pO_2 measured at time 't', $pO_{2,0}$ is the pO_2 measured at t = 0, Δt_s is the sampling interval and $\dot{n}_{MO_x}$ is the MO_x molar flow rate.

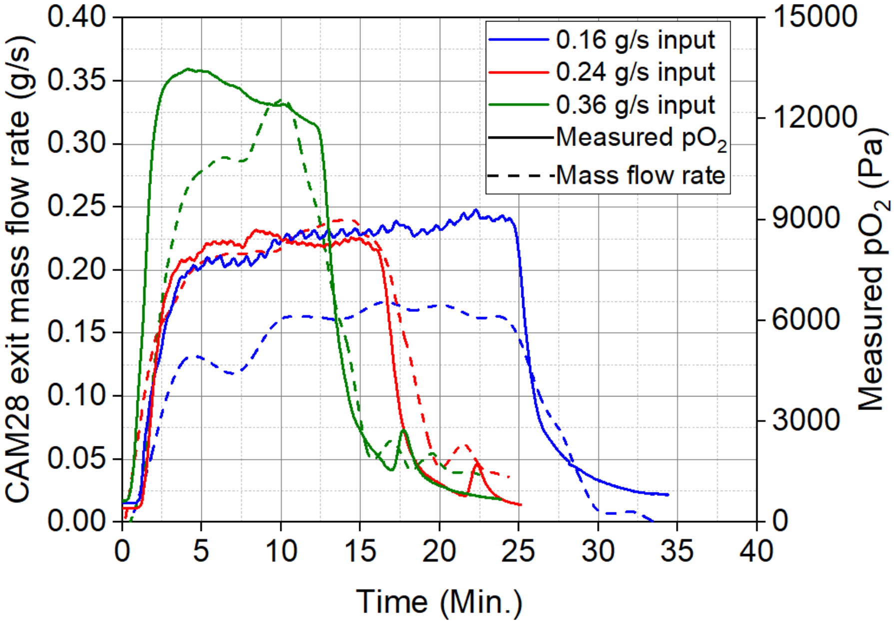

Figure 40. Dependence of the CAM28 Exit Mass Flow Rate (Dashed) and pO_2 (Solid) Measured Near the Particle Inlet On the Input CAM28 Supply Rate.

$$\Delta\delta_{pO_2} = 2\frac{(pO_{2,t} - pO_{2,0}) * \dot{V}_{N_2}\Delta t_s}{\dot{n}_{MO_x}RTtf_{reac}} \qquad \text{Eq. 32}$$

Table 7. $\Delta\delta_{po_2}$ And $\Delta\delta_{ox}$ For Different CAM28 Supply Rates

Input (g/s)	$\Delta\delta_{pO_2}$	$\Delta\delta_{ox}$
0.16	0.165	0.0384
0.24	0.105	0.0364

0.36	0.128	0.0308

Based on Table 7, $\Delta\delta_{pO_2}$ shows no clear trend with input mass flow rates, while $\Delta\delta_{ox}$ decreases with increasing input CAM28 mass flow rates. For the prototype, the expected $\delta_R = 0.12$ ($T_{R,out} = 823$ °C, $pO_{2,in} = 300$ Pa) is higher than the observed $\Delta\delta = 0.057 \pm 0.0005$, which indicates some potential internal reoxidation due to the presence of local cold spots and/or air ingress. As observed in Table 7, there are significant differences between the $\Delta\delta$ obtained from the two techniques. The diagnostic envelope must be improved to pinpoint the source of these discrepancies and to better understand the potential of ZFR for TCES. In the absence of these refinements, which will help reconcile the $\Delta\delta$ results to one another, the reader is cautioned against over interpretation of observed trends. Table 8 summarizes the results of all the α-ZFR runs. In the experiments, $T_{R,max}$ ranged from 850 °C to 950 °C, $pO_2 = 17$ Pa, and the N_2 flow rate = 2000 sccm. Table 8 shows that the ZFR is consistently able to reach $\Omega > 100$ Wh/kg throughout the reactor run time.

Table 8- The CAM28 $\Delta\delta_{ox}$ and Ω Achieved In The ZFR Under Several Maximum Temperatures And CAM28 supply rates

Run	Input particle flow rate (g/s)	Duration (min)	$T_{R,max}$ (°C)	pO_{2_in} (Pa)	$\Delta\delta_{ox}$	Ω (Wh/kg) (for pure CAM28)
1	0.5	60	953	17	0.0487 ± 0.0002	110.20
2	0.5	30	945	17	0.0553 ± 0.0004	113.38
3	0.12	15	945	17	0.0428 ± 0.0002	107.36
4	0.12	25	945	17	0.0434 ± 0.0003	107.65
5	0.16	28	882	17	0.0277 ± 0.0002	73.29
6	0.16	65	875	17	0.0287 ± 0.0005	73.78
7	0.24	30	853	17	0.0267 ± 0.0007	67.71
8	0.24	60	853	17	0.0249 ±	66.84

					0.0005	
9	0.24	40	866	17	0.0311± 0.0003	73.66
10	0.24	80	867	17	0.0309 ± 0.0005	73.56
11	0.16	60	874	17	0.0311 ± 0.0007	73.66
12	0.16	50	874	17	0.0296 ± 0.0003	72.94
13	0.24	25	857	17	0.0242 ± 0.0006	62.68
14	0.16	40	904	17	0.0384 ± 0.0008	85.60
15	0.24	25	904	17	0.0364± 0.0007	84.63
16	0.36	20	904	17	0.0308± 0.0005	81.93
17	0.16	15	904	17	0.0340± 0.0004	83.47

5.6. Second Laboratory Prototype: β-Zigzag Flow Reactor

5.6.1. Challenges Observed In α-Zigzag Flow Reactor And Corresponding β-Zigzag Flow Reactor Upgrades

The α-ZFR prototype successfully demonstrated the concept with some limitation observed, indicating opportunities to expand its performance and capabilities. Learning from the experience of the α-ZFR, an improved prototype which is denoted as the β-ZFR was manufactured to overcome the earlier limitations and allow for long term continuous operation. The main challenges observed during α-ZFR experiments were:

i. Too coarse equilibrium temperature gradient approximation

The heaters used in α-ZFR required an upgrade could not approximate the equilibrium temperature profile accurately enough, for the CAM28 reaction path to be considered an approximation of the equilibrium path. The temperature also did not reach the intended limit of 950 °C decreasing the reduction extent further. Due to insufficient spacing for the heater coils in the firebrick heater slots, their longevity during the α-ZFR experiments, the heater coils in the α-ZFR heater had low longevity requiring regular replacements

5.6.2.Heater and Temperature Detection Upgrades

To address the temperature related issues, in the β-ZFR design, special attention was paid to the heater design. Figure 41a shows the α-ZFR external heaters and Figure 41b shows the β-ZFR external heater and one layer of the insulating firebrick heaters. As a part of this upgrade, insulating firebrick layers were manufactured using CNC machining. The heater coils loaded on alumina rods heat the front and back walls of the outer shell of the β-ZFR. The heater coil placement (two near the particle exit, one or zero elsewhere), concentrates the majority of reactor power near the particle exit. Radiation shields are used to minimize radiation heat loss. This update was made to improve the equilibrium temperature gradient and increase the output energy storage density.

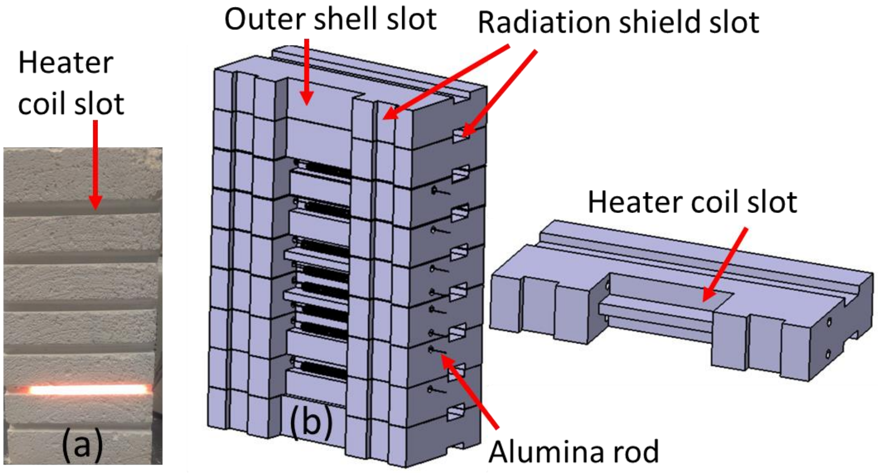

Figure 41. (a) Snapshot Of the External Heater Used In the α-ZFR, (b) CAD Model Details Of the Heaters Used In the β-ZFR

In Figure 42. the mean experimental temperature profile of the five thermocouples is displayed, alongside the corresponding δ evolution as predicted by the equilibrium model. Measuring the temperature in the x and z directions within the ZFR, under the gas flow in the z direction enhances the accuracy of Δδ predictions generated by the equilibrium model. To get the experimental δ predictions, the equilibrium model is modified to yield δ based on the experimental temperature and pO_2 profiles. To facilitate these measurements, the β-ZFR is equipped with a mesh slot that can accommodate up to five thermocouples, strategically positioned at different heights along the reaction path. These thermocouples are also laterally spaced along the width of the reactor, enabling a comprehensive temperature profile to be obtained both along the reaction path (x direction) and in the vertical direction (z direction). In a particular experiment highlighting the capabilities of these thermocouples, prior to the introduction of particles, all five thermocouples are systematically moved along the reaction path, and temperature readings are recorded. The β-ZFR uses external heaters and operates under a 500 sccm N_2 flow. The upgraded firebrick heaters improved the match between the equilibrium and experimental temperature gradient (Figure 42). The lengthy T-drop observed in the α-ZFR, along with lower maximum temperature (α-900 °C, β-978 °C), limits is reduction extent and Ω. The data shows that the lateral temperature deviation is notably higher, reaching approximately 40 °C, at the first mesh compared to the last mesh, where the deviation is less than 1 °C on account of the last mesh being least disturbed by the surrounding room temperature. This significant temperature variation across the width of the reactor highlights the importance of capturing detailed temperature profiles for a more accurate Δδ prediction of by the equilibrium model.

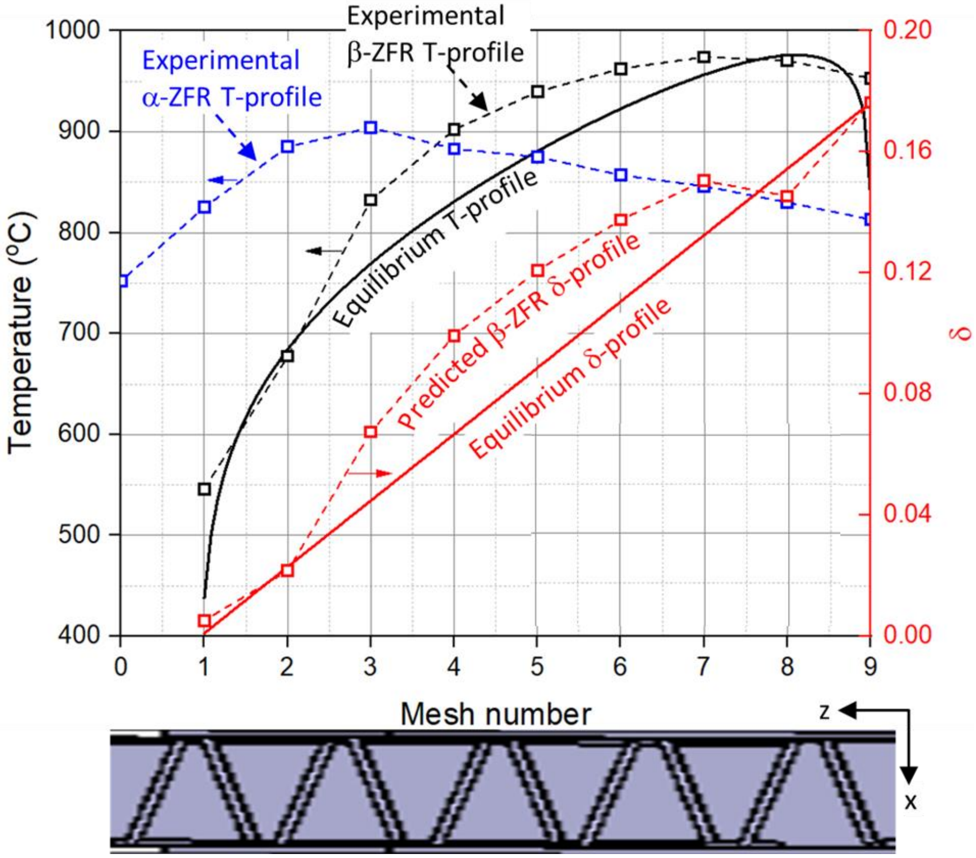

Figure 42. Comparison Of the Experimental Temperature Profiles From the α-ZFR And the β-ZFR Prototypes With the Equilibrium Temperature Profile

The next four challenges need to be understood in their entirety to understand the significance of incorporated upgrades

ii. Elimination of air ingress and N_2 loss from the semi-permanent side seams: The semi-permanently sealed bottom reactor seam is a point of particle loss from the reactor. The limited availability of CAM28 particles makes it critical to eliminate any reasons for particle loss.

iii. Elimination of air ingress and N_2 loss from the semi-permanent side seams: The semi-permanent seams on the sides and bottom of the reactor lead to oxygen ingress into the reactor decreasing the minimum pO_2 in the reactor and decreasing the reduction extent.

iv. Lack of in-operando temperature and pO_2 gradient measurement. α-ZFR only had one oxygen probe that measured pO_2 of the exiting gas at the reactor inlet. The probe was located at the reactor corner, thereby not being a reliable approximation of the pO_2 in the middle of the reactor. Furthermore α-ZFR did not measure in-operando reactor temperature during the experiment which made it difficult to reliably compare the α-ZFR with the theoretical estimations.

v. Mismatch between $\Delta\delta$ from pO_2 and from gravimetric measurements: The $\Delta\delta_{pO_2}$ and $\Delta\delta_{ox}$ values do not match. Primary suspected reasons are the oxygen ingress from reactor seam, local cold spots along the reaction path and reoxidation after the particle exit.

To address these issues, the following upgrades were incorporated in the β-ZFR design

5.6.3. Flow Channel and Mesh Upgrade

Figure 43 (left) shows a snapshot of the β-ZFR with attached temperature and O_2 probes. A mesh shelf (Figure 43 right) inserted into an outer rectangular channel replaces the earlier u-channel and semi-permanently sealed door (Figure 38). This modification addresses the N_2 loss/air ingress along the reactor length. The mesh shelf contains two vertical rectangular strips with slots to hold the mesh stands (Figure 44). The mesh stands, with spotwelded coarse and fine meshes, attach to the mesh shelf using loading tabs at the required inclination (~ 15°). Slots in the mesh stands allow attachment of up to nine temperature and O_2 probes each. The slots allow probe position adjustment for comprehensive in-operando temperature and pO_2 measurements along the reactor length. The outer rectangular channel with attached vibration motor suspends from a spring rod to prevent vibration transfer to other subsystems. While the outer rectangular shell is made of stainless steel 304, the mesh stand, and the mesh shelves are made of stainless steel 309 for better corrosion resistance at T > 900 C.

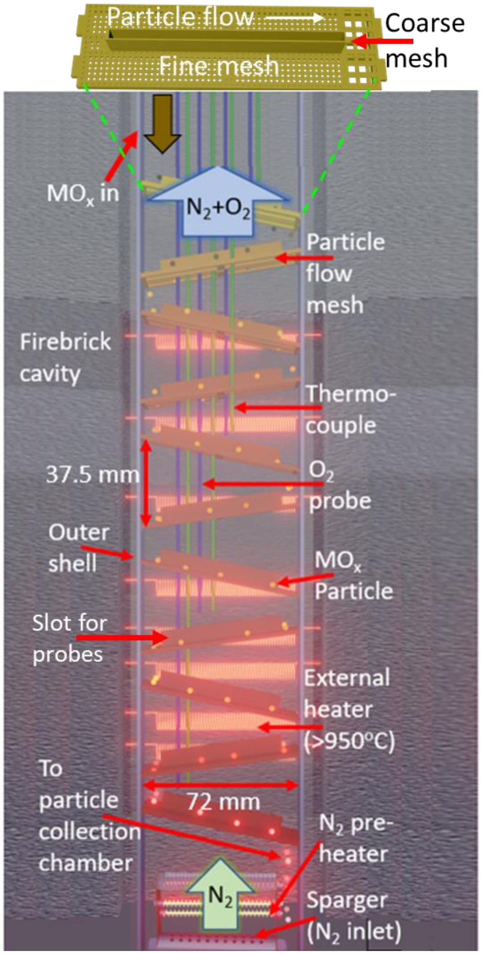

Figure 43. (Left) β-ZFR CAD Model Showing the Reaction Path and the Particle Flow Mesh

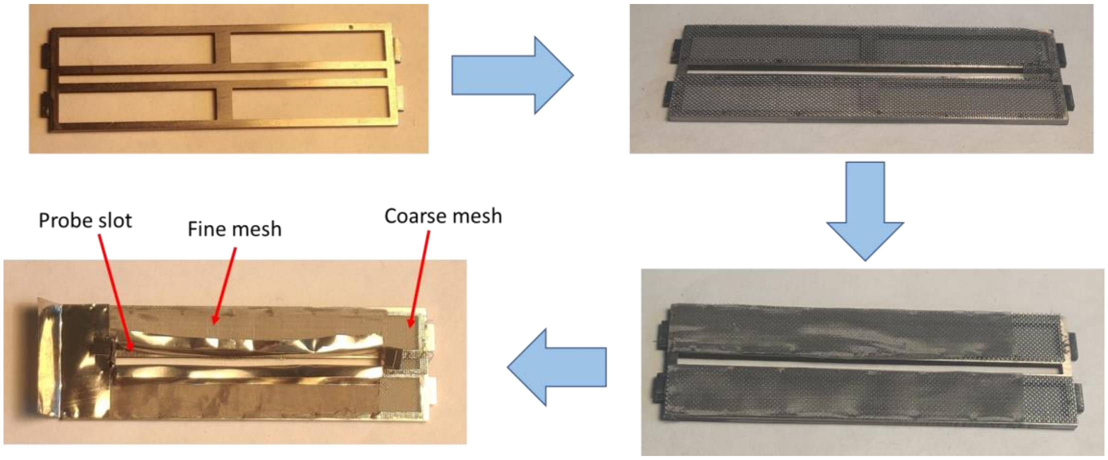

Figure 44. Process Of Fabricating the β-ZFR Mesh. One Layer Of Fine Mesh Covers One Layer Of Structural Coarse Mesh Before Spotwelding the Stainless Steel Spill Protecting Flow Guides.

5.6.4. Intermediate Support

This versatile subsystem was added to improve the β-ZFR performance and overcome several limitations of the α-ZFR. The intermediate support (Figure 45a)) stays between the reactor and the load cell, flexibly coupled to both. Significant care was taken to ensure a leak-free gas flow through the flexible coupling. The reactor, the intermediate support and the load cell are each supported independently to dampen the vibrations from the reactor to the load cell. Multiple probes attached to the intermediate support (Figure 45b)) monitor the O_2 concentration at locations between the particle exit and the particle collection chamber. These O_2 probes are used to confirm that the reactor is sufficiently purged prior to testing.

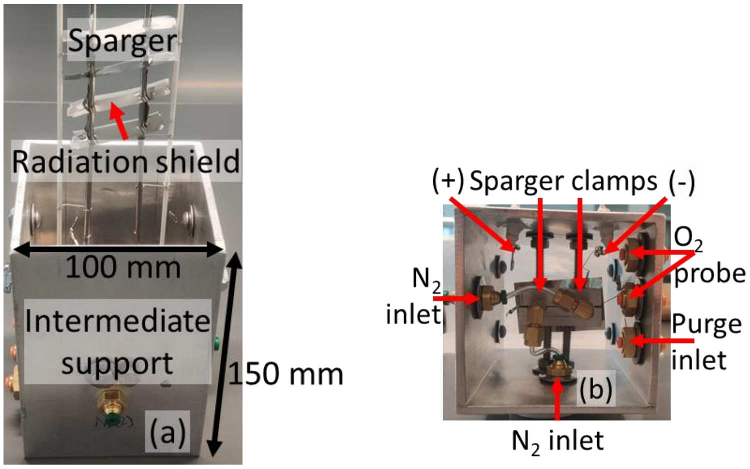

Figure 45. (a) Snapshot Of the Intermediate Support and (b) Bottom View Of the Intermediate Support With All the Features.

5.6.5. Sparger and N_2 Preheater

The sparger (Figure 46a) supplies N_2 to the particle flow channel and is located ~25 mm below the last particle flow mesh. Three preheater coils (Figure 46b) loaded on alumina rods preheat the incoming N_2 before particle interaction. A layer of stainless steel foil and fine mesh protects the preheater coils from contacting the CAM28 particles. Power is supplied to the preheater coils through alumina insulated power lines, and N_2 through the gas supply lines, both attached to the intermediate support. Special attention was paid to understanding the ZFR particle flow. The ideal particle path, which can be disrupted by the non-uniform vibration motor output, follows the zigzag mesh setup without any leakage from the mesh boundaries. The spilt particles can circumvent the zigzag mesh setup and end up in the particle collection with significantly lower residence time. The lower residence time for leaked particles brings into question the approach to thermal and chemical equilibrium vital to the success of the ZFR. To prevent this disruption of the flow path, flow guides are added (Figure 46a) to the particle flow mesh. The mesh top guides prevent particle-spill from the mesh front and back while the mesh bottom guides prevent particle entry into the probe slot during inter-mesh particle transfer. A layer of fine mesh is also attached to the mesh sides to prevent particle-spill (not shown in Figure 46).

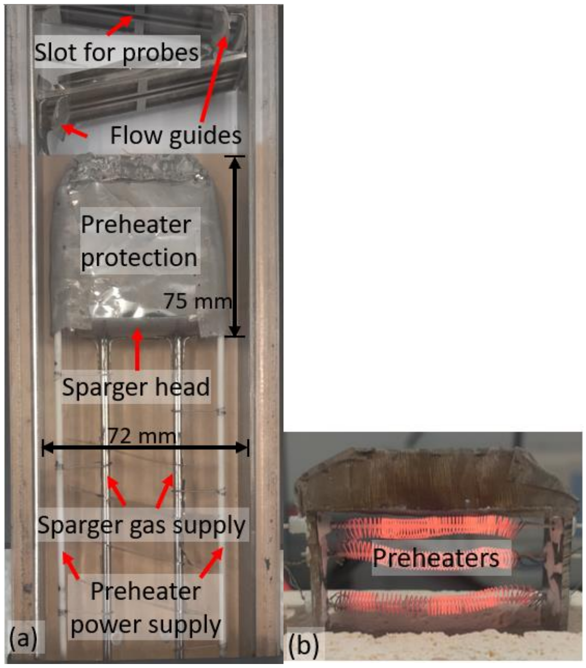

Figure 46. (a) Snapshot Of the Particle Flow Mesh and Sparger, (B) Snapshot Of the N_2 Preheaters

5.6.6.Oxygen Sampling

Contrary to the α-ZFR, Figure 49(left) shows the β-ZFR;s capability to accommodate up to four oxygen probes at different reactor heights within the mesh probe slot. The EZO-O_2 embedded oxygen sensor (range = 0-42%, accuracy = ±10 Pa) is used for β-ZFR pO_2 measurements along the reactor length. Figure 49(right) shows the experimental result of purging the reactor under 500 sccm N_2 flow rate. According to Figure 49(Right), he pO_2 slowly decreases from its initial value ~10% to 10 Pa in ~ 16 min. After the pO_2 reaches 10 Pa, there is no further change in pO_2 as it represents the sensitivity limit of the O_2 sensor. The markedly lower pO_2 along the β-ZFR path (10 Pa) compared to the α-ZFR (300 Pa) is expected to improve the reduction extent and Ω.

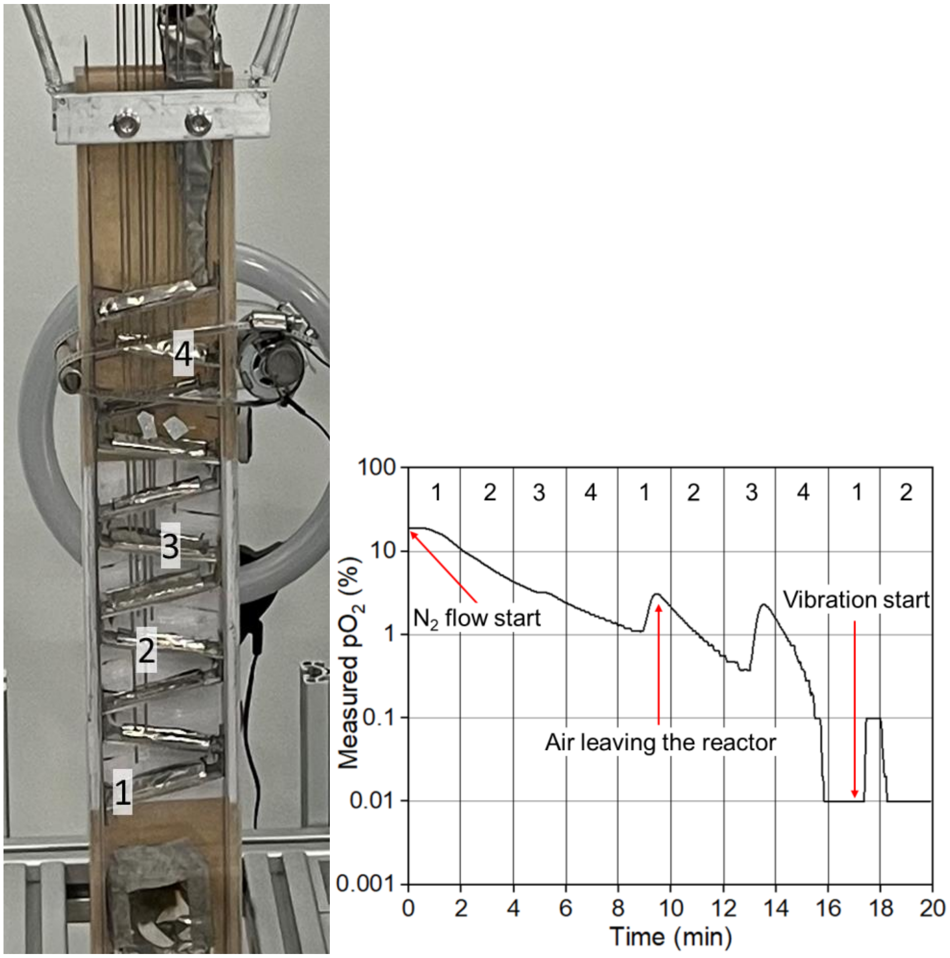

Figure 47. (Left) Four Oxygen Probes Located At Different Reactor Heights Inside the Probe Slot and (Right) Purging Oxygen Out Of the β-ZFR Prototype

5.6.7. β-ZFR Operation

Figure 48 (top) presents data from a β-ZFR experiment involving CAM28. CAM28 input mass flow rate: 0.12 g/s. $T_{R,max}$ = 974 ± 1 °C (7th mesh), $T_{R,out}$ = 953 ± 3 °C (9th mesh), pO_2 along the entire reaction path: 10 Pa before the start of particle flow, total N_2 flow rate (including buffer gas) = 1000 sccm, $\lambda \sim 20$. Measurements by four thermocouples on different meshes and one O_2 probe at the particle inlet record in-situ temperature and pO_2 throughout the experiment. The CAM28 output mass flow rate stabilizes at ~0.12 g/s after the initial transient. Figure 48 (top) illustrates that adding particles affects mesh temperatures differently, the first and fourth meshes experience decreased temperatures compared to no particle flow conditions, the eighth and ninth meshes see temperature increases post-particle flow initiation. Particle flow acts as a heat transfer fluid due to thermal contact with all ZFR meshes, causing these temperature changes. Initially, pO_2 follows particle flow transient, reaching a steady state of ~3-5 kPa. However, in this experiment, a seal failure prevented pO_2 from returning to pre-particle flow levels, as observed in the α-ZFR. During the experiment, $\Delta\delta_{OX} = 0.057$, and $\Delta\delta_{pO_2} = 0.053$, as measured in the first 8 minutes of particle flow, before the seal failure.

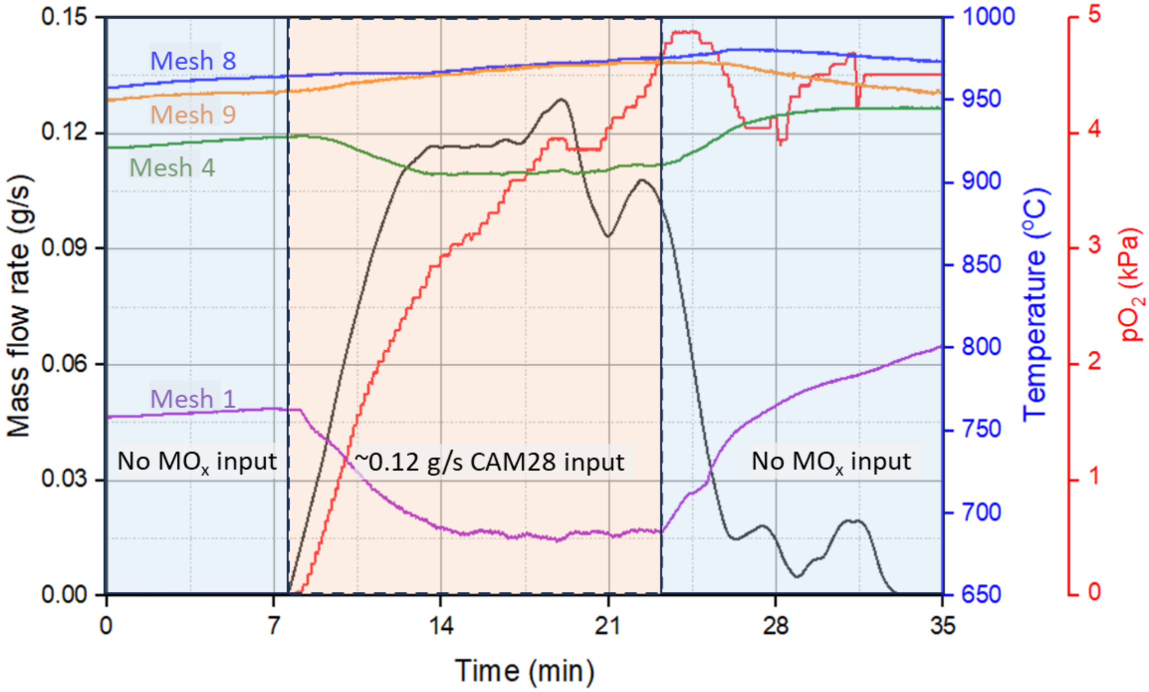

Figure 48. The CAM28 Output Mass Flow Rate, pO_2 Measured At the Particle Inlet And the Temperature Measured Near 4 Particle Flow Meshes As a Function Of Time.

5.7. Reactor Material and Particle Degradation

Analyzing the reactor degradation with multiple operational cycles is essential to establish the long term operability of the ZFR. The biggest degradation risk to the ZFR is the severe operating temperature for a stainless steel 304 sheet metal and meshes. After just one operational cycle at T > 800 °C (1 h.) a Cr_2O_3 passivation layer appears on the surface (Figure 49). This passivation layer significantly reduces further degradation of the stainless steel parts and can be scraped off the surface to reveal an untainted stainless steel layer

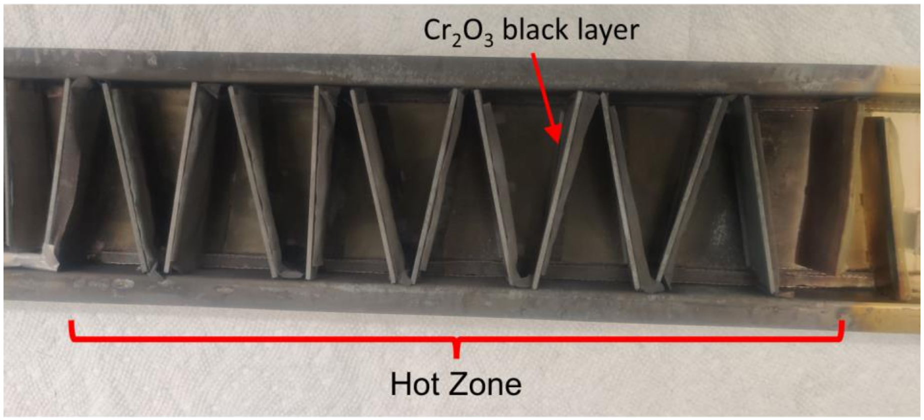

Figure 49. Snapshot Of the Chromium Oxide (Cr_2O_3) Passivation Surface Layer That Appears On the Stainless Steel Parts After Operation At T > 800 °C.

Appearance of the Cr_2O_3 passivation layer does not affect the ZFR operation because all the electronic components, which are the most sensitive to temperature rise, are located further away from the reactor hot zone. Electronic parts located closer to the hot zone, like the vibration motor, are externally cooled reducing the effect of temperature rise. This Cr_2O_3 layer significantly reduces the tensile strength of thin stainless steel sheets (< 100 μm), like the ones used in the meshes, making them vulnerable to tears. No tears or degradation signs, apart from the Cr_2O_3 layer, were observed after 11 h. of CAM28 particle flow in the α- ZFR.

Analyzing the CAM28 particles for signs of degradation is essential to establishing the long term operability of the CAM28. Thus, XRD analysis is performed on the available particles. The aim of this experiment was to compare the spectra of the samples selected each from the pre and post five redox cycled CAM28. This comparison is expected to:

i. Confirm the presence of unreactive phases in the sample detected during earlier analyses

ii. Identify the impact of five redox cycles on the crystalline structure

iii. Detect the presence of Cr_2O_3 impurities arising from the *in-operando* scaling of the oxidized stainless steel reactor.

5.7.1. X-Ray Diffraction Spectroscopy Analysis Of CAM28 Particles

Figure 50 shows the XRD spectra of CAM28 particles pre and post five redox cycles along with the characteristic peaks of the $Ca(MnO_3)$ (perovskite), $CaMn_2O_4$ (spinel) and Cr_2O_3 (rhombohedral) phases. The spinel phases observed in Figure 50 is the unreactive phase that leads to $f_{reac} < 1$. Comparison of the XRD spectra pre and post five redox cycles, reveals no apparent change in the crystalline structure of particles with every characteristic peak for perovskite and spinel phase present. The XRD analysis also shows none of the characteristic peaks of the Cr_2O_3 (rhombohedral) phase. This only confirms that Cr_2O_3 is not present in the selected samples. This, by itself, does not confirm or deny the presence of Cr_2O_3 in total CAM28 sample.

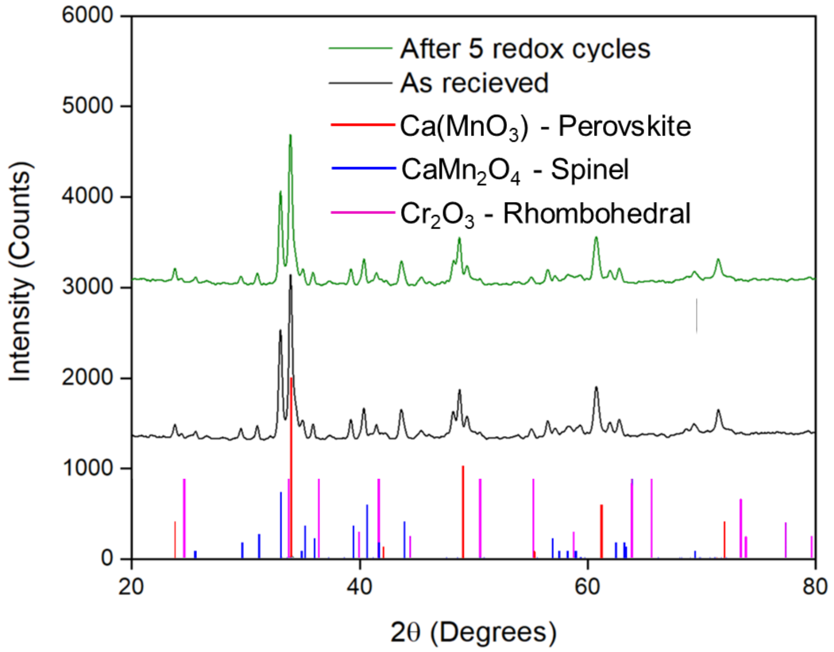

Figure 50. X-Ray Diffraction Spectra Of the CAM28 Particles As Received And After 5 Redox Cycles. Also Shown Are the Reference Spectra Of $Ca(MnO_3)$ Perovskite Phase, $CaMn_2O_4$ Spinel Phase And the Cr_2O_3 Rhombohedral Phase.

5.7.2.Scanning Electron Microscopy Analysis Of CAM28 Particles

Particle shape and morphology affect the particle flow. A change in particle morphology and shape could indicate particle attrition and would prove detrimental to long term operation. Thus, after the XRD analysis the SEM analysis of the CAM28 samples pre and post five redox cycles is performed. The aim of this experiment was to visualize the available CAM28 particles and observe their morphology and shape. The CAM28 images are also compared to sand, used as a representative particle in the earlier experiments. This analysis is expected to reveal:

i. The difference in shape of the sand and CAM28 particles in regard to their interchangeability in terms of flow properties

ii. The validity of the diffusion model assumption of spherical particles and

iii. The relative presence of fines ($d_p < 50$ μm) in the CAM28 sample as received, compared to post 5 redox cycles (fines sieved out of a 50 μm mesh).

Figure 51 shows the SEM images of CAM28 particles pre redox cycling (Figure 51a), post 5 redox cycles (Figure 51b) and sand (Figure 51 inset). The images reveal that CAM28 particles are significantly more spherical compared to sand particles. This increases the CAM28 fluidity compared to sand thus limiting the applicability of sand for comparable flow experiments. The images also support the diffusion model assumption of spherical particles. Figure 51a shows that, as received, the CAM28 sample contained significantly more fines agglomerated around larger particles compared to Figure 51b, where the fines have been removed by sieving through a 50 μm mesh. The peculiar donut shaped particles present in both the samples are an artifact of the particle manufacturing process. There is no visible change in the particle morphology after 5 redox cycles. An electron dispersive spectroscopy (EDS) needs to be performed to identify compositional changes and the presence of impurities.

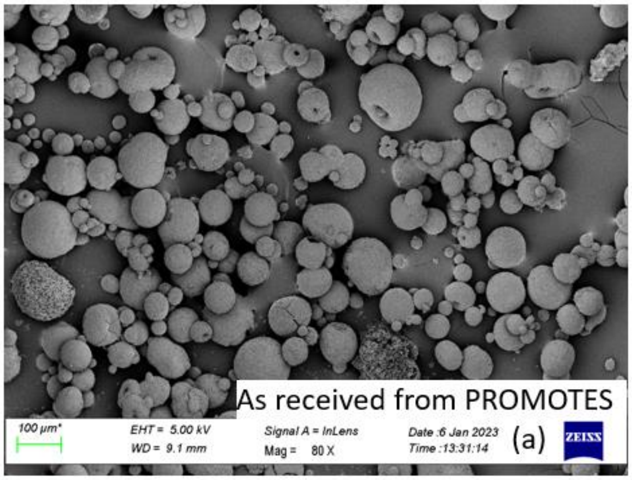

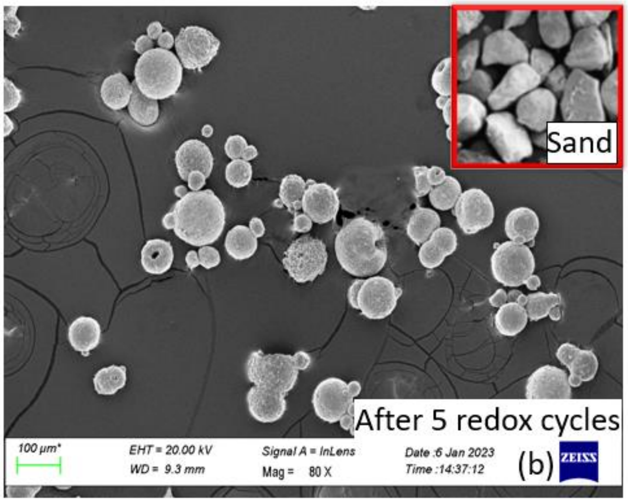

Figure 51. Scanning Electron Microscopy Images Of the Experimental CAM28 Sample (a) As Received, (b) After 5 Redox Cycles.

5.7.3. Electron Dispersive Spectroscopy of CAM28 Particles

Along with SEM, EDS analysis was performed on the particle samples from pre and post five redox cycle experiments. The aim of this experiment was to identify the elemental composition of the particles and observe their distribution on the particle surface. Figure 52 and Figure 53 show the SEM images of particles (Figure 52a and Figure 53a), EDS images showing a layered, element wise color composition (Figure 52b and Figure 53b), Ca distribution (Figure 52c and Figure 53c), Mn distribution (Figure 52d and Figure 53d), O distribution (Figure 52e and Figure 53e) and Al distribution (Figure 52f and Figure 53f) for pre and post 5 redox cycles, respectively, on the particle surface. The images show that while Ca and O are distributed uniformly on the particle surface, Al accumulates in the surface voids created by Mn in both cases. The crack in the particle observed in Figure 53a could indicate potential particle attrition during redox cycling. More work is required to understand and quantify the CAM28 particle degradation.

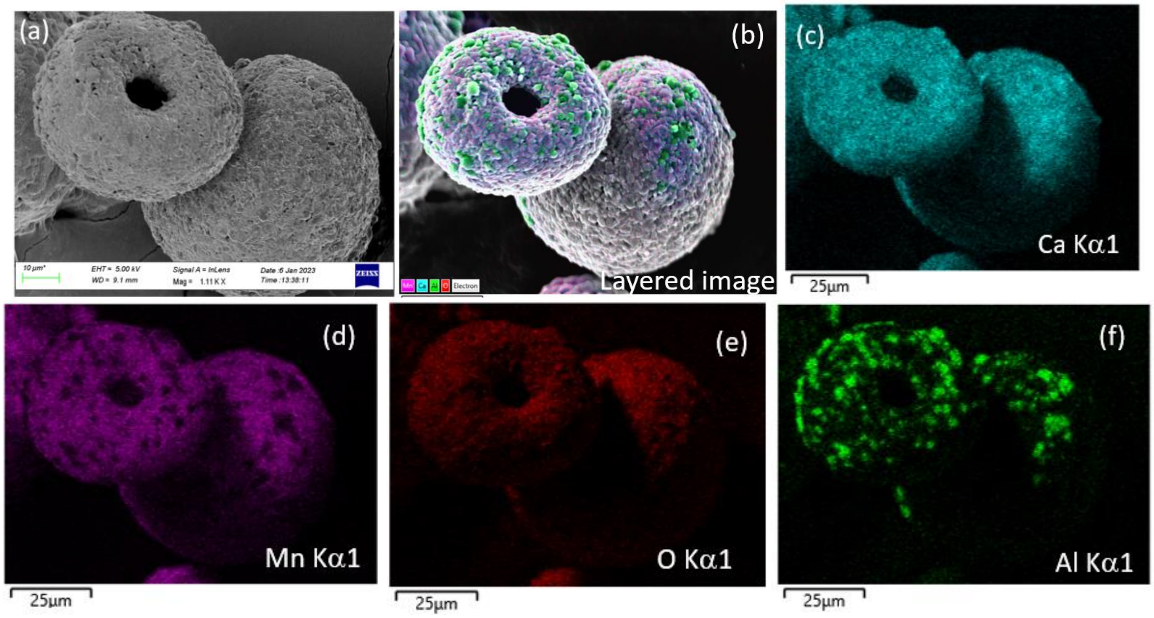

Figure 52. SEM Image Of a CAM28 Particle (a) Pre 5 Redox Cycles, (b) EDS Image Showing a Layered, Element Wise Color Composition, (c) Ca Distribution, (d) Mn Distribution (e) O Distribution, (f) Al Distribution.

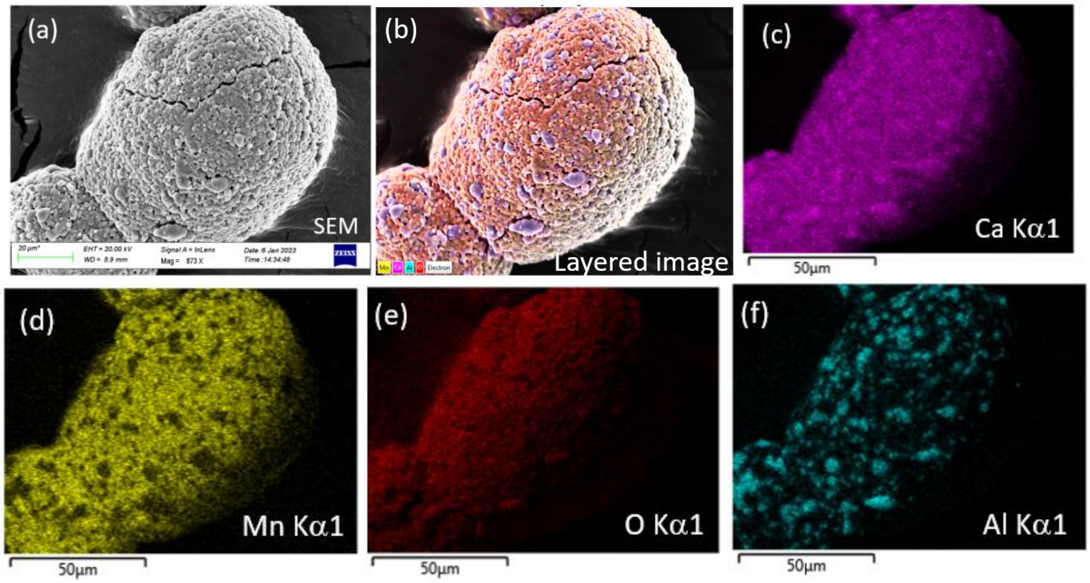

Figure 53. SEM Image Of a CAM28 Particle (a)Post 5 Redox Cycles, (b) EDS Image Showing a Layered Element Wise Color Composition, (c) Ca Distribution, (d) Mn Distribution (e) O Distribution, (f) Al Distribution.

Comparing the CAM28 atomic % in the particles with the theoretically predicted CAM28 atomic % (Table 9), it is apparent that there is not a significant difference between the experimental values pre and post 5 redox cycles to make any conclusions about the particle degradation. Interestingly the results shows that the elemental distribution in the selected CAM28 sample is not uniform, likely due to the presence of different crystalline structures as observed in the XRD.

Table 9- Shows The Comparison Of Theoretical CAM28 Atomic% With The EDS Results Obtained From The Particle Surface Pre And Post 5 Redox Cycles

Element	CAM28 Atomic %		
	Theoretical	Pre redox cycling	Post five redox cycles
Ca	20	20.5	18.9
Mn	16	21.6	16.7
Al	4	4.3	5.7
O	60	53.6	58.7

6. ZIGZAG FLOW REACTOR TECHNO-ECONOMICS

After gaining confidence that the ZFR shows potential at the laboratory scale, a techno-economic model was developed to estimate the ZFR levelized cost of storage (LCOS). The intended application for the ZFR is grid-scale energy storage (Figure 6). The following section evaluates the scaling properties of the ZFR and estimates the cost of operating the ZFR at grid-scale.

6.1. Techno-Economic Model Description

6.1.1. Scaled ZFR Model With Associated Storage Bin

In this model, particles that are thermochemically reduced by the grid-scale ZFR are stored in a storage container. Here, the objective of this analysis is to understand the scaling of cost parameters like the heat loss, LCOS and reactor and storage size as a function of stored energy and reactor power. The ZFR scales along its depth and by stacking multiple simultaneously operating flow channels along the width. In the scaled ZFR, multiple parallel operating flow channels stack along its width (w_{FS}) to achieve significantly higher power levels (Figure 54). All the flow channels radiatively share heat with each other during operation. N_2 divides equally among the flow channels separated by a solid wall and different streams do not mix during the process. An insulating cavity surrounds all the channels from top and sides minimizing the heat loss to the surroundings. The gas velocity in each flow channel is $v_T/2$.

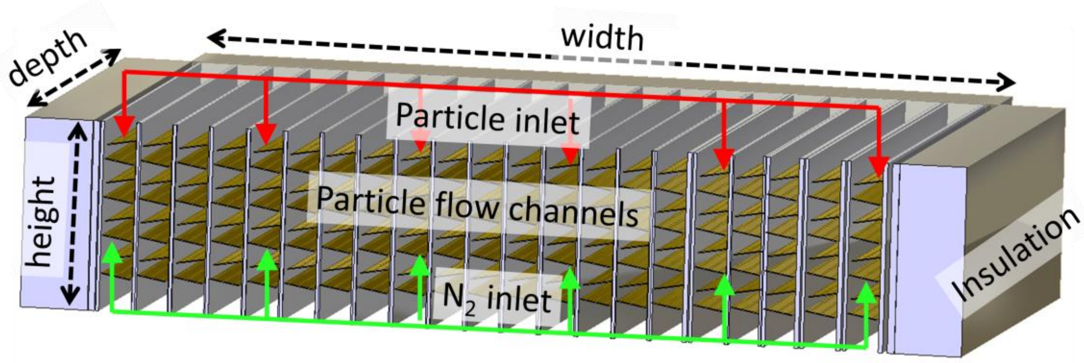

Figure 54. Cross Section Of the Grid Scale ZFR. The ZFR Scales Along Its Depth And By Stacking Multiple Simultaneously Operating, Internally Heated Particle Flow Channels Along the Width.

6.1.2.Model formulation

As the particles thermally reduce the ZFR stores both sensible and chemical energy in the oxide particles. Eq. 33 shows the total output power in a single flow channel ($P_{total,chan}$), where N_{chan} is the number of flow channels in the scaled ZFR and $\dot{m}_{MO_x}$ is the total input mass flow rate.

$$P_{total,chan} = \frac{\dot{m}_{MO_x}}{N_{chan} M_{CAM28}} \left(C_{P,MO_x} \left(T_{R,out} - T_{in} \right) + \Delta\delta\Delta h \right) \qquad \text{Eq. 33}$$

Eq. 34 shows the total fabrication material cost of a single ZFR flow channel ($C_{1\ chan\ reac}$). In Eq. 34, m_1 and C_1 are the mass and unit material cost of the flow channel and $m_{ins,1}$ and $C_{ins,1}$ are the are the mass and unit material cost of standalone unit insulation.

$$C_{1\ chan\ reac} = m_1 C_1 + m_{ins,1} C_{ins,1} \qquad \text{Eq. 34}$$

Thus, Eq. 35 shows the unit cost of the scaled ZFR with multiple flow channels per unit stored energy ($C_{perMW,s}$), where $C_{reac,ins,s}$ is the total cost of the scaled ZFR with insulation.

$$C_{perMW,s} = \frac{C_{reac,ins,s}}{P_{reac}} \qquad \text{Eq. 35}$$

The storage bin (Figure 55) is assumed to be a stainless steel 304 equilateral cylinder with an internal lining of refractory firebrick (10 cm thick, k = 0.5 W/mK, T_{max} = 1482 °C). The MO_x (CAM28) particles (d_p = 250 μm) are stored at $T = T_{store}$ and $\delta = \delta_{store}$. The storage bin is filled with N_2 to maintain reduced pO_2 with a ullage space (ull) = 10% of cylinder volume. One central and lowest layer of particles (both highlighted in red) are considered to be at $T = T_{R,out}$ for heat loss calculations for their respective directions and the ambient temperature (T_{amb}) = 300 K. Eq. 36 determines the storage bin diameter (d_{store}). In Eq. 36, f_{pack} is the packing fraction of spheres (0.635).

$$d_{store} = \left(\frac{4(1+ull)m_{CAM28}}{\pi f_{pack}\rho_{MO_x}}\right)^{\frac{1}{3}} \qquad \text{Eq. 36}$$

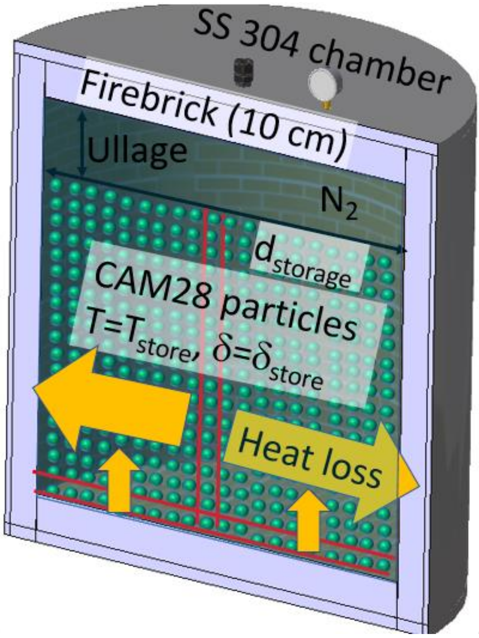

Figure 55. Schematic Of the Storage Bin For Reduced Particles. The Storage Container Is a Stainless Steel Vessel With Firebrick Lining On the Inner Walls.

Eq. 37 determines the total heat lost from this storage bin in the x-y-z directions ($Q_{loss,store}$) in the holding time t_{hold}

$$Q_{loss,store} = t_{hold}\left(\frac{T_{R,out} - T_{amb}}{R_{net}} + \left(\frac{1}{\frac{1}{k_{PB}} + \frac{1}{k_{SS}} + \frac{1}{k_{ins}} + \frac{1}{k_{N_2}}}\right) 2\pi \left(\frac{d_{store}}{2}\right)^2 \frac{T_{R,out} - T_{amb}}{d_{store} + t_{ss} + t_{ins}}\right) \quad \text{Eq. 37}$$

where d_{store} is the storage container diameter, t_{ss} and t_{ins} are the wall and the insulation thickness respectively, and k_i is the thermal conductivity of species 'i' and R_{net} is the total thermal resistance including the particle bed.

Table 10 shows all the equations used in evaluating the ZFR LCOS.

Table 10- Summary Of the Model Equations Used In Evaluating the TCES Levelized Cost Using the Scaled ZFR

Single channel analysis		
$m_{ins} = \rho_{FB} A_{cross,ins} t_{ins}$	mass of one channel insulation	Eq. 38
$C_{ins} = C_{FB,kg} m_{ins}$	Cost of one channel insulation	Eq. 39
$m_{mesh,m^2} = A_{mesh,closed} t_{mesh} \rho_{reac}$	Mesh mass per m²	Eq. 40
$m_{mesh,total} = N_{mesh} m_{mesh,m^2} d_{reac} w_{reac}$	Total mesh mass in one channel	Eq. 41
$P_{chem,chan} = \frac{\dot{m}_{MO_x} C_{P,mox}}{N_{chan} M_{CAM28}} \Delta\delta\Delta H_{MO_x}$	Total chemical power output	Eq. 42
$P_{sense,chan} = \frac{\dot{m}_{MO_x} C_{P,mox}}{N_{chan}} (T_{R,out} - T_{OX})$	Total sensible power output	Eq. 43
$P_{total,chan} = P_{chem,chan} + P_{sense,chan}$	Total power output	Eq. 44
$PD_{chan} = \frac{P_{total,chan}}{Vol_{reac}}$	One channel power density	Eq. 45

$P_{loss} = 2\frac{k_{FB}}{t_{ins}}\left(A_{side} + A_{front,back}\right)\left(T_{ins,SIW} - T_{out}\right) + A_{top}\left(T_{ins,STW} - T_{out}\right)$	Power loss from one channel	Eq. 46
$loss_{\%} = 100\frac{P_{loss}}{P_{total}}$	% power loss from one channel	Eq. 47
	Scaled ZFR analysis	
$P_{reac} = \frac{Q_{storage}}{t_{store}}$	Target reactor power	Eq. 48
$\Delta\delta = f(pO_{2,in}, T_{R,out})$	Output reduction extent	Eq. 49
$Q_{store,mole} = C_{P,mox}M_{CAM28}\left(T_{R,out} - T_{in}\right) + \Delta\delta\Delta H_{MO_x}$	Energy stored per mole MO_x	Eq. 50
$\dot{m}_{MO_x} = \frac{M_{CAM28}P_{reac}}{Q_{store,mole}}$	MO_x mass flow rate	Eq. 51
$\dot{V}_{N_2,300K,total} = \frac{\dot{m}_{MO_x}\lambda\Delta\delta RT}{M_{CAM28}P}$	Total required N_2 flow rate	Eq. 52
$N_{chan} = \frac{\dot{V}_{N_2,300K,total}}{\dot{V}_{N_2,300K}}$	Number of channels	Eq. 53
$w_{reac,s} = N_{chan}w_{reac}$	Scaled reactor width	Eq. 54
$Vol_{reac,s} = w_{reac,s}d_{reac}h_{reac}$	Scaled reactor volume	Eq. 55
$A_{side,s} = d_{reac}h_{reac}$	Scaled reactor y-z area	Eq. 56
$A_{front,s} = w_{reac,s}h_{reac}$	Scaled reactor x-z	Eq. 57
$A_{top,s} = w_{reac,s}d_{reac}$	Scaled reactor x-y area	Eq. 58
$Vol_{ins,s} = t_{ins}(2\left(A_{front,s}+A_{side,s}\right) + A_{top,s}$	Scaled reactor insulation volume	Eq. 59
$m_{ins,s} = Vol_{ins,s}\rho_{FB}$	scaled reactor insulation mass	Eq. 60
$C_{ins,s} = m_{ins,s}C_{FB,kg}$	scaled insulation cost	Eq. 61
$P_{loss,s} = 2\frac{k_{FB}}{t_{ins}}\left(A_{side,s} + A_{front,s}\right)\left(T_{ins,SIW} - T_{out}\right) + A_{top,s}\left(T_{ins,STW} - T_{out}\right)$	scaled power loss	Eq. 62

$P_{reac} = \frac{Q_{storage}}{t_{store}}$	Target reactor power	Eq. 63
$\Delta\delta = f(pO_{2,in}, T_{R,out})$	Output reduction extent	Eq. 64
$Q_{store,mole} = C_{P,mox}M_{CAM28}\left(T_{R,out} - T_{in}\right) + \Delta\delta\Delta H_{MO_x}$	Energy stored per mole MO_x	Eq. 65
$\dot{m}_{MO_x} = \frac{M_{CAM28}P_{reac}}{Q_{store,mole}}$	MO_x mass flow rate	Eq. 66
$Vol_{reac,ins,s} = Vol_{reac,s} + Vol_{ins,s}$	Reactor volume including insulation	Eq. 67
$m_{reac,ins,s} = m_{ins,s} + N_{chan}m_{chan}$	Reactor + insulation mass	Eq. 68
$C_{reac,ins,s} = C_{ins,s} + N_{chan}C_{chan}$	Reactor + insulation cost	Eq. 69
$C_{MW,s} = \frac{C_{reac,ins,s}}{P_{reac}}$	Reactor + insulation cost per MW	Eq. 70
$\dot{V}_{N_2,300K,total} = \frac{\dot{m}_{MO_x}\lambda\Delta\delta RT}{M_{CAM28}P}$	Total required N_2 flow rate	Eq. 71

Single channel cost analysis

$m_{1\ chan\ reac} = m_{chan} + m_{ins}$	mass of one channel reactor	Eq. 72
$C_{1\ chan\ reac} = C_{chan} + C_{ins}$	cost of one channel reactor	Eq. 73
$C_{perMW} = \frac{C_{1\ chan\ reac}}{P_{total,chan}}$	Cost of one channel reactor per MW	Eq. 74
$m_{ins} = \rho_{FB}A_{cross,ins}t_{ins}$	mass of one channel insulation	Eq. 75
$C_{ins} = C_{FB,kg}m_{ins}$	Cost of one channel insulation	Eq. 76
$m_{mesh,m^2} = A_{mesh,closed}t_{mesh}\rho_{reac}$	Mesh mass per m^2	Eq. 77
$m_{mesh,total} = N_{mesh}m_{mesh,m^2}d_{reac}w_{reac}$	Total mesh mass in one channel	Eq. 78
$m_{wall,front} = 2A_{front/back}t_{wall}\rho_{reac}$	front and back wall mass	Eq. 79
$m_{wall,side} = 2A_{side}t_{wall}\rho_{reac}$	side wall mass	Eq. 80

$m_{chan} = m_{mesh,total} + m_{wall,front} + m_{wall,side}$	one channel mass	Eq. 81
$C_{chan} = m_{chan}C_{reac}$	one channel cost	Eq. 82
$P_{chem,chan} = \frac{\dot{m}_{MO_x}C_{P,mox}}{N_{chan}M_{CAM28}}\Delta\delta\Delta H_{MO_x}$	Total chemical power output	Eq. 83
$P_{sense,chan} = \frac{\dot{m}_{MO_x}C_{P,mox}}{N_{chan}}\left(T_{R,out} - T_{in}\right)$	Total sensible power output	Eq. 84
$P_{total,chan} = P_{chem,chan} + P_{sense,chan}$	Total power output	Eq. 85
$PD_{chan} = \frac{P_{total,chan}}{Vol_{reac}}$	One channel power density	Eq. 86
$P_{loss} = 2\frac{k_{FB}}{t_{ins}}\left(A_{side} + A_{front,back}\right)\left(T_{ins,SIW} - T_{out}\right) + A_{top}(T_{ins,STW} - T_{out})$	Power loss from one channel	Eq. 87
$loss_{\%} = 100\frac{P_{loss}}{P_{total}}$	% power loss from one channel	Eq. 88
$w_{reac,s} = N_{chan}w_{reac}$	Scaled reactor width	Eq. 89
$Vol_{reac,s} = w_{reac,s}d_{reac}h_{reac}$	Scaled reactor volume	Eq. 90
$A_{side,s} = d_{reac}h_{reac}$	Scaled reactor y-z area	Eq. 91
$A_{front,s} = w_{reac,s}h_{reac}$	Scaled reactor x-z	Eq. 92
$A_{top,s} = w_{reac,s}d_{reac}$	Scaled reactor x-y area	Eq. 93
$Vol_{ins,s} = t_{ins}(2\left(A_{front,s}+A_{side,s}\right) + A_{top,s}$	Scaled reactor insulation volume	Eq. 94
$m_{ins,s} = Vol_{ins,s}\rho_{FB}$	scaled reactor insulation mass	Eq. 95
$C_{ins,s} = m_{ins,s}C_{FB,kg}$	scaled insulation cost	Eq. 96
$P_{loss,s} = \frac{k_{FB}(}{t_{ins}}2\left(A_{side,s} + A_{front,s}\right)\left(T_{ins,SIW} - T_{out}\right) + A_{top,s}(T_{ins,STW} - T_{out})$	scaled power loss	Eq. 97
Storage container		
$Vol_{CAM28} = \frac{m_{CAM28}}{f_{pack}\rho_{MO_x}}$	CAM28 particle volume to	Eq. 98

	meet the demand	
$\mathrm{Vol_{store}} = (1 + \mathrm{ull})\mathrm{Vol_{CAM28}}$	Storage volume	Eq. 99
$\mathrm{d_{store}} = \left(\frac{4\mathrm{Vol_{store}}}{\pi}\right)^{\frac{1}{3}}$	Storage diameter	Eq. 100
$\mathrm{R_{PB}} = \frac{\log\left(\frac{\mathrm{d_{store}}}{\mathrm{d_{part}}}\right)}{2\pi \mathrm{d_{store}} \mathrm{k_{PB}}}$	Particle bed thermal resistance	Eq. 101
$\mathrm{R_{SS}} = \frac{\log\left(\frac{\frac{\mathrm{d_{store}}}{2} + \mathrm{t_{ss}}}{\frac{\mathrm{d_{store}}}{2}}\right)}{2\pi \mathrm{d_{store}} \mathrm{k_{ss}}}$	Stainless steel thermal resistance	Eq. 102
$\mathrm{Vol_{SS}} = \pi\left(\left(\frac{\mathrm{d_{store}}}{2} + \mathrm{t_{ss}}\right)^2 - \left(\frac{\mathrm{d_{store}}}{2}\right)^2\right)\mathrm{d_{store}} + \pi \mathrm{d_{store}}^2 \mathrm{t_{ss}}$	Stainless steel storage cylinder volume	Eq. 103
$\mathrm{m_{SS}} = \mathrm{Vol_{SS}} \rho_{\mathrm{SS}}$	Mass SS required for storage	Eq. 104
$\mathrm{C_{SS}} = \mathrm{m_{SS}} \mathrm{C_{SS,kg}}$	Cost of storage SS	Eq. 105
$\mathrm{C_{CAM28}} = \mathrm{m_{CAM28}} \mathrm{C_{CAM28,kg}} \mathrm{C_{CAM28,mult}}$	Cost of required CAM28	Eq. 106
$\mathrm{R_{ins}} = \frac{\log\left(\frac{\frac{\mathrm{d_{store}}}{2} + \mathrm{t_{ss}} + \mathrm{t_{ins}}}{\frac{\mathrm{d_{store}}}{2}}\right)}{2\pi \mathrm{d_{store}} \mathrm{k_{ins}}}$	Insulation thermal resistance	Eq. 107
$\mathrm{R_{net}} = \mathrm{R_{ins}} + \mathrm{R_{PB}} + \mathrm{R_{SS}}$	Net thermal resistance	Eq. 108
$\dot{\mathrm{Q}}_{\mathrm{loss,store}} = \frac{\mathrm{T_{R,out}} - \mathrm{T_{amb}}}{\mathrm{R_{net}}} + \left(\frac{1}{\frac{1}{\mathrm{k_{PB}}} + \frac{1}{\mathrm{k_{SS}}} + \frac{1}{\mathrm{k_{ins}}} + \frac{1}{\mathrm{k_{N_2}}}}\right) 2\pi \left(\frac{\mathrm{d_{store}}}{2}\right)^2 \left(\frac{\mathrm{T_{R,out}} - \mathrm{T_{amb}}}{\mathrm{d_{store}} + \mathrm{t_{ss}} + \mathrm{t_{ins}}}\right)$	Storage heat loss	Eq. 109

$\dot{Q}_{loss,total} = \dot{Q}_{loss,store}\left(t_{hold} + \frac{t_{discharge} + t_{charge}}{2}\right) + P_{loss,s}t_{store}$	Total heat loss including reactor	Eq. 110
$loss_{\%,store} = 100\frac{\dot{Q}_{loss,store}}{Q_{storage}}$	% loss from storage	Eq. 111
$T_{wall,in} = T_{R,out} - \dot{Q}_{loss,store}R_{PB}$	Storage inner wall temperature	Eq. 112
$Vol_{ins,store} = \pi\left(\left(\frac{d_{store}}{2} + t_{ss} + t_{ins}\right)^2 - \left(\frac{d_{store}}{2} + t_{ss}\right)^2\right)\frac{d_{store}}{2} + 2\pi\left(\frac{d_{store}}{2}\right)^2 t_{ins}$	Volume of storage insulation	Eq. 113
$m_{ins,store} = Vol_{ins,store}\rho_{FB}$	Mass of storage insulation	Eq. 114
Reactor-storage system level sizing and costs		
$V_{N_2,annual} = \dot{V}_{N_2,300K}N_{cycles,annual}$	Annual N_2 volume	Eq. 115
tcycle= tcharge+thold+tdischarge	Total cycle time	Eq. 116
$N_{cycles,annual} = 8760\ \frac{t_{discharge}}{t_{cycle}}$	Annual number of cycles	Eq. 117
$C_{ins,store} = m_{ins,store}C_{FB,kg}$	Cost of storage insulation	Eq. 118
$C_{cap} = C_{SS} + C_{ins,store} + 1.1C_{CAM28} + C_{ins,s} + C_{chan}N_{chan}$	Capital costs	Eq. 119
$C_{op} = V_{N_2,annual}C_{N_2}$	Operational costs	Eq. 120
$C_{rep} = 0.02\left(C_{cap} - 1.1C_{CAM28}\right)$	Replacement costs	Eq. 121
$C_{total} = (1 + r) * (C_{cap} + C_{op} + C_{rep})$	Total costs	Eq. 122
$LCOS = \frac{C_{total}}{Q_{storage}N_{cycles,annual}}$	Levelized cost of TCES	Eq. 123
$LCOS_{op} = \frac{C_{op}}{Q_{storage}N_{cycles,annual}}$	Operational cost of TCES	Eq. 124
$LCOS_{cap} = \frac{C_{cap}}{Q_{storage}N_{cycles,annual}}$	Capital cost of TCES	Eq. 125

$\mathrm{LCOS_{CAM28}} = \dfrac{\mathrm{C_{CAM28}}}{\mathrm{Q_{storage} N_{cycles,annual}}}$	Unit cost of CAM28	Eq. 126
$\mathrm{LCOS_{storage}} = \dfrac{\mathrm{C_{SS} + C_{ins,store}}}{\mathrm{Q_{storage} N_{cycles,annual}}}$	Unit cost of storage	Eq. 127
$\mathrm{LCOS_{reac}} = \dfrac{\mathrm{C_{ins,s} + C_{chan} N_{chan}}}{\mathrm{Q_{storage} N_{cycles,annual}}}$	Unit reactor cost	Eq. 128
$\mathrm{LCOS_{rep}} = \dfrac{\mathrm{C_{rep}}}{\mathrm{Q_{storage} N_{cycles,annual}}}$	Unit replacement cost	Eq. 129
$\mathrm{LCOS_{interest}} = \dfrac{\mathrm{r * (C_{cap} + C_{op} + C_{rep})}}{\mathrm{Q_{storage} N_{cycles,annual}}}$	Unit interest cost	Eq. 130

6.2. Results

6.2.1. Scaled ZFR Sizing Considerations

The scaled ZFR design assumes Inconel 625 and insulating firebrick construction. Considering ten meshes per channel, Figure 56 shows the dependence of the ZFR fabrication cost per unit power on the ZFR power and $T_{R,out}$. $C_{MW,S}$ decreases with an increase in the ZFR power. Due to the radiatively coupled flow channels, at larger sizes the ZFR becomes more economical with insulation only needed on the outer walls. A steep initial $C_{MW,S}$ decrease with increasing ZFR power, levels off at ~ 10 MW, indicating no further benefit in increasing ZFR power. C_{MW} also decreases with decrease in $T_{R,out}$. As $T_{R,out}$ decreases, the ZFR size increases (decreasing $C_{MW,S}$) to accommodate the decrease in Ω. The result in Figure 56 shows that the unit cost of reactor is <$25/kW for the entire range of reactor power and $T_{R,out}$. Table 11 shows the constant parameters for calculation of the ZFR scaling costs. The corresponding cost of the falling particle receiver ($125/kW [101]) is up to 5 times higher than the grid scale ZFR cost in spite of adding particle flow obstructions. This result emphasizes the affordability of scaling the ZFR.

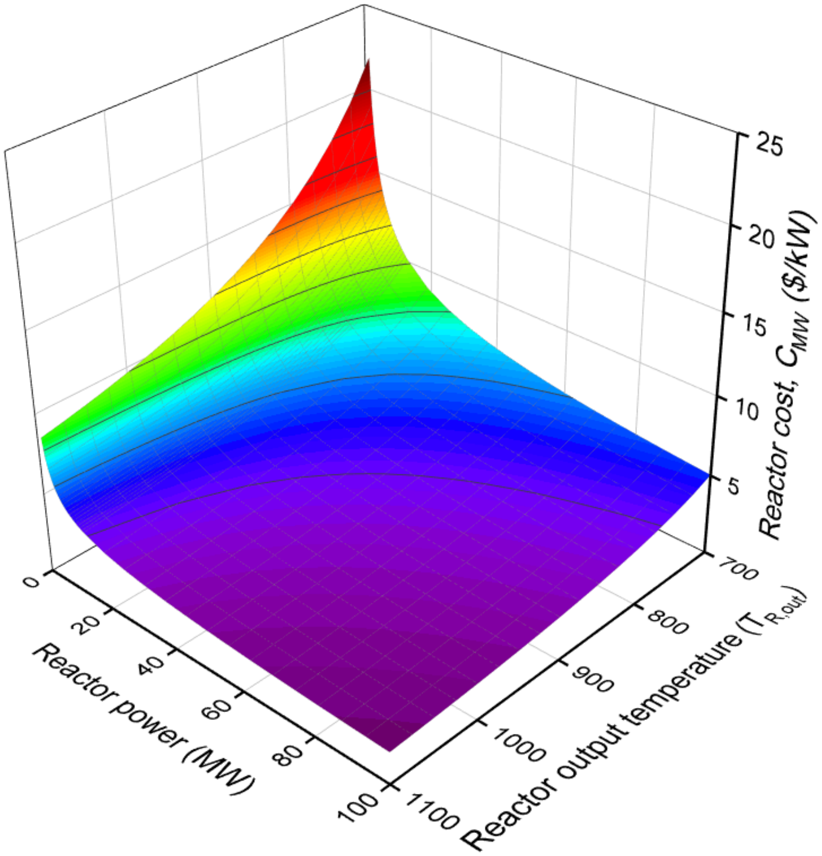

Figure 56. Dependence Of C_{MW} (10^3 $/MW) On the ZFR Power And $T_{R,out}$. C_{MW} Decreases As the ZFR Size Increases. Due To This, C_{MW} Decreases With Increase In the ZFR Power, Tapering Out At ~ 10 MW And With Decrease In $T_{R,out}$.

Table 11 – Constants For the ZFR Fabrication Cost Scaling Calculation

Parameter	Value
Reactor height	35 cm
Width - one channel	7.5 cm
Depth - one channel	100 cm
Particle diameter	250 μm
Sweep ratio	1.5
$\Delta\delta$	0.2
Inlet pO_2 of inert gas	500 Pa
Inconel cost	$43/kg [141]
Mesh open area	50%
Mesh thickness	200 μm
Front and back wall Thickness	500 μm
Firebrick cost	$1.11/kg [142]
Insulation thickness	10 cm

Figure 57a shows that the d_{store} increases with increase in storage capacity (due to increased m_{CAM28}) and decreases with increase in storage temperature (due to increased storage density). Figure 57b shows the daily heat loss (< 0.9%) as a fraction of the stored energy is independent of the storage temperature. At the same time, the daily heat loss decreases by 75% with an increase in the storage capacity from 10 to 100 MWh. Both of these results can be explained by the excellent insulating properties of the metal oxide particles (~ 0.1 W/mK). As the storage capacity increases at a constant $T_{R,out}$ and δ_R, m_{CAM28} increases, improving the overall insulation and reducing the heat loss.

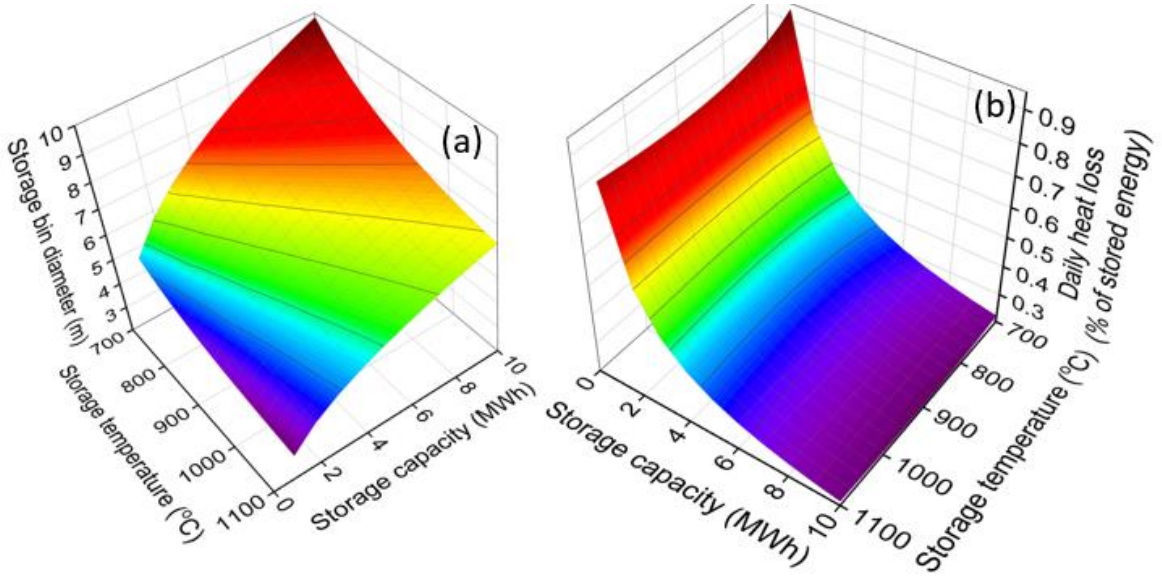

Figure 57. (a) Dependence Of the Storage Bin Diameter On the Total Storage Capacity And Storage T, (B) Dependence Of the Daily Heat Loss As a Percentage Of Stored Energy On the Total Storage Capacity And Storage T.

6.2.2.Levelized Cost Of Storage

LCOS (Eq. 130) is defined as the sum of capital costs (Eq. 119), annual operational costs (Eq. 120), annual replacement costs (Eq. 121), MO_x- 10%, parts-2% and annual interest rate (r = 6%) normalized to the total annual discharged energy. The values for annual MO_x and parts replacement and r, are inspired from the values mentioned in Gorman et al. [49]. The capital costs consist of the reactor, storage bin, insulation and CAM28 material and fabrication costs, and operational cost consisting of N_2 costs. For a total storage capacity = 100 MWh, charge/discharge duration = 8 h. and hold duration = 24 h., thee LCOS decreases by 76% (22 ¢/MWh to 6.2 ¢/MWh) when the storage temperature increases from 700 °C to 1100 °C (Figure 58). This decrease results from the significant improvement in Ω at higher temperature. The highest fraction of LCOS are capital costs (>80%), the highest fraction of which are due to CAM28 costs (>95%) (Figure 58b). This cost distribution gives the freedom to add sufficient design redundancies, without significantly affecting the LCOS. The high CAM28 fraction highlights the prominence of MO_x cost on LCOS. This result also suggests that it is worthwhile to increase the cost of the reactor or inert gas if there is a significant decrease in the cost of the metal oxide or operate the reactor at a lower temperature. One drastic improvement in the distribution of costs among the selected components is the markedly lower fraction of reactor and storage bin in the LCOS compared to Gorman et al.'s predictions (Figure 3) [49]. It is suspected that the much smaller reactor cost prediction for the scale ZFR is the primary reason for this difference. The ZFR is a more scalable concept than the SR3 and therefore can be optimized to minimize the fabrication costs, a luxury not afforded to SR3. The LCOS predicted with the scaled ZFR ranges from the lower end of the LCOS of currently available technologies, to 50% of the minimum LCOS in Figure 2 indicating a major step forward meeting the DOE's goal of affordable multi-day energy storage.

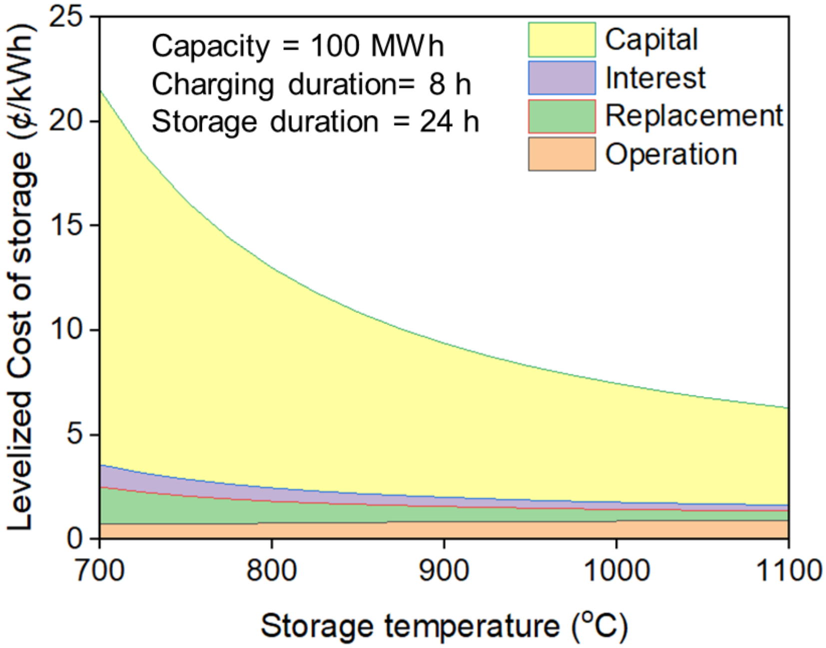

Figure 58. LCOS and Its Components Vs. Storage Temperature. The Capital Costs Make Up the Largest Fraction Of the LCOS. All Other Costs Add Up To <20% Of LCOS.

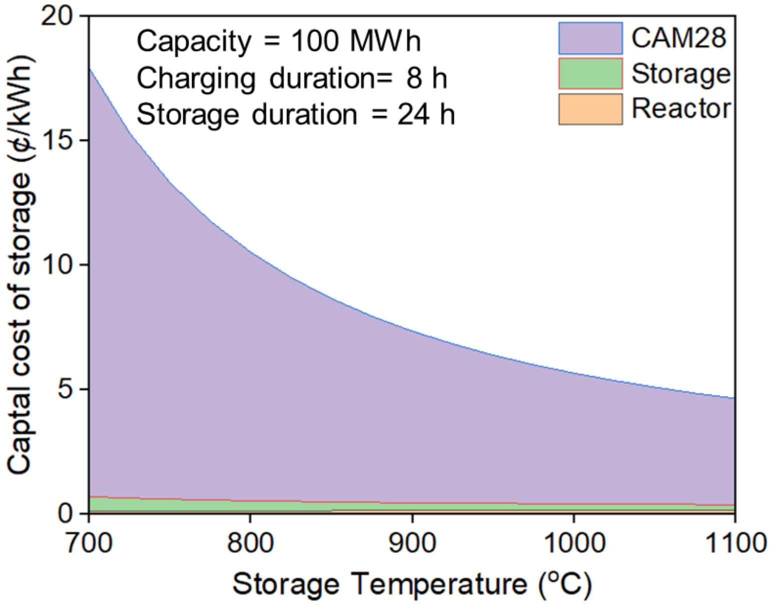

Figure 59. Capital Costs and Its Components Vs. Storage Temperature. The CAM28 Material Costs Dominate The Capital Costs. Reactor and Storage Fabrication Costs Add Up To <5% Of the Capital Costs

7. CONCLUSIONS

The text discusses a study on thermochemical energy storage and reactor design, emphasizing the growing interest in energy storage, particularly for renewable sources like solar, as a means to address temporal resource variability. While various energy storage technologies are available for short-duration storage demands (less than 10 h.), the options become scarcer for longer storage periods. The most cost-effective technologies for multi-day storage applications (ranging from 10 to 100 h.) currently include lead-acid batteries, pumped storage hydropower, and diabatic compressed air energy storage. However, these technologies are not without their challenges, including issues related to sizing, geography, and disposal, especially in the case of lead-acid batteries.

The study aims to provide solutions through reduction reactors to significantly enhance the state of the art in Thermochemical Energy Storage (TCES). The broader objective is to find pathways to meet the US Department of Energy's goal of reducing the levelized cost of electricity (LCOE) from utility solar to 5 ¢/kWh by 2030, representing a 50% reduction compared to 2021.

The research questions addressed in this study, after a thorough review of the field's current state, include:

i. Can a practical reduction reactor approach the theoretical TCES capabilities of redox materials?

ii. What process parameters are critical to achieving cost-effective grid-scale thermochemical energy storage with "ideal" materials?

iii. What is the impact of repeated thermal and redox cycling on the storage density of materials with known properties, and what are the effects on the reactor?

The previously studied reactor concepts indicate that the obstructed flow reactor (OFR), where the free fall of particles under gravity is obstructed using engineered mechanical obstructions, provides a scalable reactor design with sufficient control over particle residence time (τ_R). Chapter 2 also elucidated the relationship between the reduction extent (δ), temperature and oxygen partial pressure (pO_2), as well as the relationship between δ and the reduction enthalpy (Δh). This relationship forms the basis of the equilibrium model for the discrete reactor provided in Chapter 3.

Chapter 3 of this study provides an analytical model that identifies a distinctive discretization of the continuous equilibrium curve. This discretization minimizes exergy destruction for the specified boundary conditions, allowing for an approach toward equilibrium along the reaction path. From a reactor perspective, the study examines the primary process parameters influencing Thermochemical Energy Storage (TCES) costs, specifically: (i)the sweep ratio (λ) and $pO_{2,in}$ (associated with N_2-related costs).$T_{R,max}$ (driving reactor material costs), $T_{R,out}$ and δ_R (impacting storage container costs) and the energy storage density, Ω (influencing the metal oxides costs). Analyzing the interplay among these factors reveals several cost-related trade-offs. The tradeoffs converge at a recommended set of operating conditions: oxidized particle temperature = 550 °C, Maximum reduction temperature = 1100 °C, sweep ratio = 1.5 and inlet pO_2 of sweep gas = 3.24 kPa, resulting in reactor output temperature = 1100 °C, output reduction extent = 0.191 and the energy storage density Ω = 203 Wh/kg, to maximize the number cost minimization avenues. It is worth noting that contrary to a prevalent assumption in the thermochemical community, excessively high temperatures and ultra-pure N_2 are not necessary to achieve significant Ω values. Additionally, increasing the number of δ steps taken by metal oxides from the reactor inlet to the outlet reduces exergy destruction and enhances the reaction's proximity to chemical equilibrium along the reaction path but increase the cost of control.

Chapter 4 introduces a mass transfer model, indicating that reactor power densities of approximately 10 MW/m^3 are achievable with carefully selected combinations of reactor dimensions and operating conditions. A trade-off is observed between the mass transfer coefficient, ΔpO_2 between the particle surface and its surroundings, and power density, which influences the overall costs. The primary control variables for O_2-N_2 diffusion model, vN_2 and d_{part} when increased, lead to increase in Π, while simultaneously increasing $\Delta pO_2/pO_{2,out}$ which pushes the reaction away from chemical equilibrium.

Chapter 5 introduces the Zigzag Flow Reactor (ZFR) as a potential reduction reactor for thermochemical energy storage. It provides a comparison of particle-gas mixing and residence time between the ZFR and other reactor concepts from the literature, highlighting the ZFR's unique combination of effective particle-gas mixing and tunable residence time. Two ZFR prototypes, α-ZFR and β-ZFR, are developed, to prove the ZFR concept. The β-ZFR achieved up to six times $\Delta\delta$ compared to any previous TCES reduction reactors with CAM28. The β-ZFR also achieved Ω~130 Wh/kg under laboratory conditions. The reduction extent obtained from two independent measurements, one ex-operando and one in-operando, corroborate with each other in the β-ZFR experiments validating the reduction reaction mass conservation. The degradation study do not show visible signs of particle degradation over 5 redox cycles. No consistent trend of δ degradation is seen in the experimental results either.

Chapter 6 presents a techno-economic model to estimate the levelized cost of thermochemical energy storage with a scaled ZFR. The ZFR's scalability and negligible daily heat loss from the reactor-storage system make it suitable for multi-day energy storage applications. Reactor costs constitute only a tiny portion of the levelized cost of storage, emphasizing the affordability of scaling the ZFR. The techno-economic model results show that the grid scale ZFR can meet the DOE’s goal of affordable multi-day energy storage.

REFERENCES

[1] World Energy Investment 2023, OECD, 2023. doi:10.1787/e0e92e98-en.

[2] S. Erdogan, U.K. Pata, S.A. Solarin, Towards carbon-neutral world: The effect of renewable energy investments and technologies in G7 countries, Renew. Sustain. Energy Rev. 186 (2023) 113683. doi:10.1016/J.RSER.2023.113683.

[3] China now has 30 CSP projects with thermal energy storage underway, Solarpaces.Org. (2022). https://www.solarpaces.org/china-now-has-30-csp-projects-with-thermal-energy-storage-underway/.

[4] M. Ramzan, K.R. Abbasi, H.A. Iqbal, T.S. Adebayo, What's at Stake? The empirical importance of government revenue and debt and renewable energy for environmental neutrality in the US economy, Renew. Energy. 205 (2023) 475–489. doi:10.1016/j.renene.2023.01.071.

[5] U.K. Pata, A.E. Caglar, M.T. Kartal, S. Kılıç Depren, Evaluation of the role of clean energy technologies, human capital, urbanization, and income on the environmental quality in the United States, J. Clean. Prod. 402 (2023) 136802. doi:10.1016/j.jclepro.2023.136802.

[6] S. Ullah, R. Luo, M. Nadeem, J. Cifuentes-Faura, Advancing sustainable growth and energy transition in the United States through the lens of green energy innovations, natural resources and environmental policy, Resour. Policy. 85 (2023) 103848. doi:10.1016/j.resourpol.2023.103848.

[7] Concentrating Solar-Thermal Power | Department of Energy, Energy.Gov. (2021). https://www.energy.gov/eere/solar/concentrating-solar-thermal-power.

[8] Generation 3 Concentrating Solar Power Systems (Gen3 CSP, Energy.Gov. (2021). https://www.energy.gov/eere/solar/generation-3-concentrating-solar-power-systems-gen3-csp.

[9] DOE Breaks Ground on Concentrating Solar Power Pilot Culminating $100 Million Research Effort _ Department of Energy, Energy.Gov. (2022).

[10] J. Kosowatz, Energy Storage Smooths the Duck Curve, Mech. Eng. 140 (2018) 30–35. doi:10.1115/1.2018-JUN-1.

[11] J. Widén, N. Carpman, V. Castellucci, D. Lingfors, J. Olauson, F. Remouit, M. Bergkvist, M. Grabbe, R. Waters, Variability assessment and forecasting of renewables: A review for solar, wind, wave and tidal resources, Renew. Sustain. Energy Rev. 44 (2015) 356–375. doi:10.1016/j.rser.2014.12.019.

[12] R. Perez, M. David, T.E. Hoff, M. Jamaly, S. Kivalov, J. Kleissl, P. Lauret, M. Perez, Spatial and Temporal Variability of Solar Energy, Found. Trends® Renew. Energy. 1 (2016) 1–44. doi:10.1561/2700000006.

[13] R. Perez, P. Lauret, M. Perez, M. David, T.E. Hoff, S. Kivalov, Solar Resource Variability BT - Wind Field and Solar Radiation Characterization and Forecasting: A Numerical Approach for Complex Terrain, in: R. Perez (Ed.), Springer International Publishing, Cham, 2018: pp. 149–170. doi:10.1007/978-3-319-76876-2_7.

[14] M.S. Javed, J. Jurasz, M. Guezgouz, F.A. Canales, T.H. Ruggles, T. Ma, Impact of multi-annual renewable energy variability on the optimal sizing of off-grid systems, Renew. Sustain. Energy Rev. 183 (2023) 113514. doi:10.1016/j.rser.2023.113514.

[15] B. Tarroja, F. Mueller, S. Samuelsen, Solar power variability and spatial diversification: implications from an electric grid load balancing perspective, Int. J. Energy Res. 37 (2013) 1002–1016. doi:10.1002/er.2903.

[16] O. Schmidt, S. Melchior, A. Hawkes, I. Staffell, Projecting the Future Levelized Cost of Electricity Storage Technologies, Joule. 3 (2019) 81–100. doi:10.1016/j.joule.2018.12.008.

[17] J. Liu, Z. Huang, M. Fan, J. Yang, J. Xiao, Y. Wang, Future energy infrastructure, energy platform and energy storage, Nano Energy. 104 (2022) 107915. doi:10.1016/j.nanoen.2022.107915.

[18] R.B. Schainker, Executive overview: energy storage options for a sustainable energy future, in: IEEE Power Eng. Soc. Gen. Meet. 2004., IEEE, 2004: pp. 2310–2315. doi:10.1109/PES.2004.1373298.

[19] V. Viswanathan, K. Mongird, R. Franks, X. Li, V. Sprenkle, R. Baxter, Grid energy storage technology cost and performance assessment, 2022. https://www.energy.gov/energy-storage-grandchallenge/downloads/2020-grid-energy-storage-technology-cost-and-performance.

[20] I. Pawel, The Cost of Storage – How to Calculate the Levelized Cost of Stored Energy (LCOE) and Applications to Renewable Energy Generation, Energy Procedia. 46 (2014) 68–77. doi:10.1016/j.egypro.2014.01.159.

[21] V. Jülch, T. Telsnig, M. Schulz, N. Hartmann, J. Thomsen, L. Eltrop, T. Schlegl, A Holistic Comparative Analysis of Different Storage Systems using Levelized Cost of Storage and Life Cycle Indicators, Energy Procedia. 73 (2015) 18–28. doi:10.1016/j.egypro.2015.07.553.

[22] L.H. Saw, K. Somasundaram, Y. Ye, A.A.O. Tay, Electro-thermal analysis of Lithium Iron Phosphate battery for electric vehicles, J. Power Sources. 249 (2014) 231–238. doi:10.1016/j.jpowsour.2013.10.052.

[23] L. Jiao, Z. Liu, Z. Sun, T. Wu, Y. Gao, H. Li, F. Li, L. Niu, An advanced lithium ion battery based on a high quality graphitic graphene anode and a Li[Ni0.6Co0.2Mn0.2]O2 cathode, Electrochim. Acta. 259 (2018) 48–55. doi:10.1016/j.electacta.2017.10.155.

[24] I. Bloom, L.K. Walker, J.K. Basco, D.P. Abraham, J.P. Christophersen, C.D. Ho,

Differential voltage analyses of high-power lithium-ion cells. 4. Cells containing NMC, J. Power Sources. 195 (2010) 877–882. doi:10.1016/j.jpowsour.2009.08.019.

[25] J. Schmitt, A. Maheshwari, M. Heck, S. Lux, M. Vetter, Impedance change and capacity fade of lithium nickel manganese cobalt oxide-based batteries during calendar aging, J. Power Sources. 353 (2017) 183–194. doi:10.1016/j.jpowsour.2017.03.090.

[26] P.T. Moseley, D.A.J. Rand, K. Peters, Enhancing the performance of lead–acid batteries with carbon – In pursuit of an understanding, J. Power Sources. 295 (2015) 268–274. doi:10.1016/j.jpowsour.2015.07.009.

[27] P. Ruetschi, Review on the lead—acid battery science and technology, J. Power Sources. 2 (1977) 3–120. doi:10.1016/0378-7753(77)85003-9.

[28] C. Ding, H. Zhang, X. Li, T. Liu, F. Xing, Vanadium Flow Battery for Energy Storage: Prospects and Challenges, J. Phys. Chem. Lett. 4 (2013) 1281–1294. doi:10.1021/jz4001032.

[29] Q. Zheng, X. Li, Y. Cheng, G. Ning, F. Xing, H. Zhang, Development and perspective in vanadium flow battery modeling, Appl. Energy. 132 (2014) 254–266. doi:10.1016/j.apenergy.2014.06.077.

[30] S. Kruk-Gotzman, P. Ziółkowski, I. Iliev, G.-P. Negreanu, J. Badur, Techno-economic evaluation of combined cycle gas turbine and a diabatic compressed air energy storage integration concept, Energy. 266 (2023) 126345. doi:10.1016/j.energy.2022.126345.

[31] J. Zhang, S. Zhou, S. Li, W. Song, Z. Feng, Performance analysis of diabatic compressed air energy storage (D-CAES) system, Energy Procedia. 158 (2019) 4369–4374. doi:10.1016/j.egypro.2019.01.782.

[32] D. Stolten, V. Scherer, Transition to renewable energy systems, 2013. http://dnb.d-nb.de.

[33] J.I. Pérez-Díaz, M. Chazarra, J. García-González, G. Cavazzini, A. Stoppato, Trends and challenges in the operation of pumped-storage hydropower plants, Renew. Sustain. Energy Rev. 44 (2015) 767–784. doi:10.1016/j.rser.2015.01.029.

[34] D. Wu, D. Wang, T. Ramachandran, J. Holladay, A techno-economic assessment framework for hydrogen energy storage toward multiple energy delivery pathways and grid services, Energy. 249 (2022) 123638. doi:10.1016/j.energy.2022.123638.

[35] A. Alzahrani, S.K. Ramu, G. Devarajan, I. Vairavasundaram, S. Vairavasundaram, A Review on Hydrogen-Based Hybrid Microgrid System: Topologies for Hydrogen Energy Storage, Integration, and Energy Management with Solar and Wind Energy, Energies. 15 (2022) 7979. doi:10.3390/en15217979.

[36] Y. Li, H. Dai, Recent advances in zinc–air batteries, Chem. Soc. Rev. 43 (2014) 5257–5275. doi:10.1039/C4CS00015C.

[37] N. Borchers, S. Clark, B. Horstmann, K. Jayasayee, M. Juel, P. Stevens, Innovative zinc-based batteries, J. Power Sources. 484 (2021) 229309. doi:10.1016/j.jpowsour.2020.229309.

[38] A. Berrada, K. Loudiyi, I. Zorkani, System design and economic performance of gravity energy storage, J. Clean. Prod. 156 (2017) 317–326. doi:10.1016/j.jclepro.2017.04.043.

[39] W. Tong, Z. Lu, W. Chen, M. Han, G. Zhao, X. Wang, Z. Deng, Solid gravity energy storage: A review, J. Energy Storage. 53 (2022) 105226. doi:10.1016/j.est.2022.105226.

[40] G. Alva, Y. Lin, G. Fang, An overview of thermal energy storage systems, Energy. 144 (2018) 341–378. doi:10.1016/j.energy.2017.12.037.

[41] G. Sadeghi, Energy storage on demand: Thermal energy storage development, materials, design, and integration challenges, Energy Storage Mater. 46 (2022) 192–222. doi:10.1016/j.ensm.2022.01.017.

[42] J.P. Hoffstaedt, D.P.K. Truijen, J. Fahlbeck, L.H.A. Gans, M. Qudaih, A.J. Laguna, J.D.M. De Kooning, K. Stockman, H. Nilsson, P.T. Storli, B. Engel, M. Marence, J.D. Bricker, Low-head pumped hydro storage: A review of applicable technologies for design, grid integration, control and modelling, Renew. Sustain. Energy Rev. 158 (2022). doi:10.1016/j.rser.2022.112119.

[43] M. Noussan, P.P. Raimondi, R. Scita, M. Hafner, The role of green and blue hydrogen in the energy transition—a technological and geopolitical perspective, Sustain. 13 (2021) 1–26. doi:10.3390/su13010298.

[44] R. Raman, V.K. Nair, V. Prakash, A. Patwardhan, P. Nedungadi, Green-hydrogen research: What have we achieved, and where are we going? Bibliometrics analysis, Energy Reports. 8 (2022) 9242–9260. doi:10.1016/j.egyr.2022.07.058.

[45] S. Shiva Kumar, H. Lim, An overview of water electrolysis technologies for green hydrogen production, Energy Reports. 8 (2022) 13793–13813. doi:10.1016/j.egyr.2022.10.127.

[46] H. Song, S. Luo, H. Huang, B. Deng, J. Ye, Solar-Driven Hydrogen Production: Recent Advances, Challenges, and Future Perspectives, ACS Energy Lett. 7 (2022) 1043–1065. doi:10.1021/acsenergylett.1c02591.

[47] H. Ishaq, I. Dincer, C. Crawford, A review on hydrogen production and utilization: Challenges and opportunities, Int. J. Hydrogen Energy. 47 (2022) 26238–26264. doi:10.1016/j.ijhydene.2021.11.149.

[48] R. Shan, J. Reagan, S. Castellanos, S. Kurtz, N. Kittner, Evaluating emerging long-duration energy storage technologies, Renew. Sustain. Energy Rev. 159 (2022) 112240. doi:10.1016/j.rser.2022.112240.

[49] B.T. Gorman, M. Lanzarini-Lopes, N.G. Johnson, J.E. Miller, E.B. Stechel, Techno-Economic Analysis of a Concentrating Solar Power Plant Using Redox-Active Metal Oxides as Heat Transfer Fluid and Storage Media, Front. Energy Res. 9 (2021) 1–18. doi:10.3389/fenrg.2021.734288.

[50] C. Prieto, P. Cooper, A.I. Fernández, L.F. Cabeza, Review of technology: Thermochemical energy storage for concentrated solar power plants, Renew. Sustain. Energy Rev. 60 (2016) 909–929. doi:10.1016/j.rser.2015.12.364.

[51] M. Deutsch, F. Horvath, C. Knoll, D. Lager, C. Gierl-Mayer, P. Weinberger, F. Winter, High-Temperature Energy Storage: Kinetic Investigations of the CuO/Cu2O Reaction Cycle, Energy and Fuels. 31 (2017) 2324–2334. doi:10.1021/acs.energyfuels.6b02343.

[52] A. Bayon, R. Bader, M. Jafarian, L. Fedunik-Hofman, Y. Sun, J. Hinkley, S. Miller, W. Lipiński, Techno-economic assessment of solid–gas thermochemical energy storage systems for solar thermal power applications, Energy. 149 (2018) 473–484. doi:10.1016/j.energy.2017.11.084.

[53] C. Agrafiotis, A. Becker, M. Roeb, C. Sattler, Exploitation of thermochemical cycles based on solid oxide redox systems for thermochemical storage of solar heat. Part 5: Testing of porous ceramic honeycomb and foam cascades based on cobalt and manganese oxides for hybrid sensible/thermochemical heat s, Sol. Energy. 139 (2016) 676–694. doi:10.1016/j.solener.2016.09.013.

[54] M. Silakhori, M. Jafarian, M. Arjomandi, G.J. Nathan, Thermogravimetric analysis of Cu, Mn, Co, and Pb oxides for thermochemical energy storage, J. Energy Storage. 23 (2019) 138–147. doi:10.1016/j.est.2019.03.008.

[55] A.J. Schrader, H.E. Bush, D. Ranjan, P.G. Loutzenhiser, Aluminum-doped calcium manganite particles for solar thermochemical energy storage: Reactor design, particle characterization, and heat and mass transfer modeling, Int. J. Heat Mass Transf. 152 (2020) 119461. doi:10.1016/j.ijheatmasstransfer.2020.119461.

[56] C. Wieckert, U. Frommherz, S. Kräupl, E. Guillot, G. Olalde, M. Epstein, S. Santén, T. Osinga, A. Steinfeld, A 300 kW Solar chemical pilot plant for the carbothermic production of zinc, J. Sol. Energy Eng. Trans. ASME. 129 (2007) 190–196. doi:10.1115/1.2711471.

[57] S.E.B. Edwards, V. Materić, Calcium looping in solar power generation plants, Sol. Energy. 86 (2012) 2494–2503. doi:10.1016/j.solener.2012.05.019.

[58] I. Ermanoski, N.P. Siegel, E.B. Stechel, A new reactor concept for efficient solar-thermochemical fuel production, J. Sol. Energy Eng. Trans. ASME. 135 (2013) 1–10. doi:10.1115/1.4023356.

[59] A.J. Schrader, G.L. Schieber, A. Ambrosini, P.G. Loutzenhiser, Experimental demonstration of a 5 kWth granular-flow reactor for solar thermochemical energy storage with aluminum-doped calcium manganite particles, Appl. Therm. Eng. 173

(2020) 115257. doi:10.1016/j.applthermaleng.2020.115257.

[60] J.E. Miller, A. Ambrosini, S.M. Babiniec, E.N. Coker, C.K. Ho, H. Al-Ansary, S.M. Jeter, P.G. Loutzenhiser, N.G. Johnson, E.B. Stechel, High Performance Reduction/Oxidation Metal Oxides for Thermochemical Energy Storage (PROMOTES), in: Vol. 1 Biofuels, Hydrog. Syngas, Altern. Fuels; CHP Hybrid Power Energy Syst. Conc. Sol. Power; Energy Storage; Environ. Econ. Policy Considerations Adv. Energy Syst. Geothermal, Ocean. Emerg. E, American Society of Mechanical Engineers, 2016: pp. 1–8. doi:10.1115/ES2016-59660.

[61] B. Wong, Sulfur Based Thermochemical Heat Storage for Baseload Concentrated Solar Power Generation, U.S. Dep. Energy. (2014) 38. https://www.osti.gov/servlets/purl/1165341.

[62] J. Sunku Prasad, P. Muthukumar, F. Desai, D.N. Basu, M.M. Rahman, A critical review of high-temperature reversible thermochemical energy storage systems, Appl. Energy. 254 (2019) 113733. doi:10.1016/j.apenergy.2019.113733.

[63] B. Bulfin, J. Vieten, C. Agrafiotis, M. Roeb, C. Sattler, Applications and limitations of two step metal oxide thermochemical redox cycles; A review, J. Mater. Chem. A. 5 (2017) 18951–18966. doi:10.1039/c7ta05025a.

[64] A.P. Muroyama, A.J. Schrader, P.G. Loutzenhiser, Solar electricity via an Air Brayton cycle with an integrated two-step thermochemical cycle for heat storage based on Co3O4/CoO redox reactions II: Kinetic analyses, Sol. Energy. 122 (2015) 409–418. doi:10.1016/j.solener.2015.08.038.

[65] B.Wong, Thermochemical Heat Storage for Concentrated Solar Power, Thermochemical System Reactor Design for Thermal Energy Storage, 2011.

[66] C. Agrafiotis, M. Roeb, M. Schmücker, C. Sattler, Exploitation of thermochemical cycles based on solid oxide redox systems for thermochemical storage of solar heat. Part 2: Redox oxide-coated porous ceramic structures as integrated thermochemical reactors/heat exchangers, Sol. Energy. 114 (2015) 440–458. doi:10.1016/j.solener.2014.12.036.

[67] G. Karagiannakis, C. Pagkoura, A. Zygogianni, S. Lorentzou, A.G. Konstandopoulos, Monolithic ceramic redox materials for thermochemical heat storage applications in CSP plants, Energy Procedia. 49 (2014) 820–829. doi:10.1016/j.egypro.2014.03.089.

[68] T. Block, M. Schmücker, Metal oxides for thermochemical energy storage: A comparison of several metal oxide systems, Sol. Energy. 126 (2016) 195–207. doi:10.1016/j.solener.2015.12.032.

[69] K.K. Ghose, A. Bayon, A.J. Page, Electronic Structure and High-Temperature Thermochemistry of Oxygen-Deficient BaMO3(M = Ti-Cu) Perovskites, J. Phys. Chem. C. 3 (2020). doi:10.1021/acs.jpcc.0c06369.

[70] R.D. Barcellos, M.D. Sanders, J. Tong, A.H. McDaniel, R.P. O'Hayre,

BaCe0.25Mn0.75O3-: δ - promising perovskite-type oxide for solar thermochemical hydrogen production, Energy Environ. Sci. 11 (2018) 3256–3265. doi:10.1039/c8ee01989d.

[71] G. Avgouropoulos, T. Ioannides, H.K. Matralis, J. Batista, S. Hocevar, CuO–CeO2 Mixed Oxide Catalysts for the Selective Oxidation of Carbon Monoxide in Excess Hydrogen, Catal. Letters. (2001). doi:10.1023/A:1009013029842.

[72] E. Alonso, C. Pérez-Rábago, J. Licurgo, E. Fuentealba, C.A. Estrada, First experimental studies of solar redox reactions of copper oxides for thermochemical energy storage, Sol. Energy. 115 (2015) 297–305. doi:10.1016/j.solener.2015.03.005.

[73] R.B. Diver, J.E. Miller, M.D. Allendorf, N.P. Siegel, R.E. Hogan, Solar thermochemical water-splitting ferrite-cycle heat engines, J. Sol. Energy Eng. Trans. ASME. 130 (2008) 0410011–0410018. doi:10.1115/1.2969781.

[74] M. Pishahang, E. Bakken, S. Stølen, C.I. Thomas, P.I. Dahl, Oxygen non-stoichiometry, redox thermodynamics, and structure of LaFe1 - xCoxO3 - δ, Ionics (Kiel). 19 (2013) 869–878. doi:10.1007/s11581-012-0811-z.

[75] S.P. Scott, D. Mantzavinos, A. Hartley, M. Sahibzada, I.S. Metcalfe, Reactivity of LSCF perovskites, Solid State Ionics. 152–153 (2002) 777–781. doi:10.1016/S0167-2738(02)00327-2.

[76] A. Navrotsky, Energetics and Crystal Chemical Systematic among Ilmenite, Lithium Niobate, and Perovskite Structures, Chem. Mater. 10 (1998) 2787–2793. doi:10.1021/cm9801901.

[77] D.R. Barcellos, F.G. Coury, A. Emery, M. Sanders, J. Tong, A. McDaniel, C. Wolverton, M. Kaufman, R. O'Hayre, Phase Identification of the Layered Perovskite CexSr2- xMnO4 and Application for Solar Thermochemical Water Splitting, Inorg. Chem. 58 (2019) 7705–7714. doi:10.1021/acs.inorgchem.8b03487.

[78] A.A. Emery, J.E. Saal, S. Kirklin, V.I. Hegde, C. Wolverton, High-Throughput Computational Screening of Perovskites for Thermochemical Water Splitting Applications, Chem. Mater. 28 (2016) 5621–5634. doi:10.1021/acs.chemmater.6b01182.

[79] A.H. Bork, E. Povoden-Karadeniz, A.J. Carrillo, J.L.M. Rupp, Thermodynamic assessment of the solar-to-fuel performance of La0.6Sr0.4Mn1-yCryO3-δ perovskite solid solution series, Acta Mater. 178 (2019) 163–172. doi:10.1016/j.actamat.2019.07.022.

[80] A. Bayon, A. de la Calle, K.K. Ghose, A. Page, R. McNaughton, Experimental, computational and thermodynamic studies in perovskites metal oxides for thermochemical fuel production: A review, Int. J. Hydrogen Energy. 45 (2020) 12653–12679. doi:10.1016/j.ijhydene.2020.02.126.

[81] M. Kubicek, A.H. Bork, J.L.M. Rupp, Perovskite oxides-a review on a versatile

material class for solar-to-fuel conversion processes, J. Mater. Chem. A. 5 (2017) 11983–12000. doi:10.1039/c7ta00987a.

[82] N. Gokon, K. Hara, Y. Sugiyama, S. Bellan, T. Kodama, C. Hyun-seok, Thermochemical two-step water splitting cycle using perovskite oxides based on LaSrMnO3 redox system for solar H2 production, Thermochim. Acta. 680 (2019) 178374. doi:10.1016/j.tca.2019.178374.

[83] A.E. Ramos, D. Maiti, Y.A. Daza, J.N. Kuhn, V.R. Bhethanabotla, Co, Fe, and Mn in La-perovskite oxides for low temperature thermochemical CO2 conversion, Catal. Today. 338 (2019) 52–59. doi:10.1016/j.cattod.2019.04.028.

[84] K.J. Albrecht, G.S. Jackson, R.J. Braun, Thermodynamically consistent modeling of redox-stable perovskite oxides for thermochemical energy conversion and storage, Appl. Energy. 165 (2016) 285–296. doi:10.1016/j.apenergy.2015.11.098.

[85] N. Gokon, T. Yawata, S. Bellan, T. Kodama, H.S. Cho, Thermochemical behavior of perovskite oxides based on LaxSr1-x(Mn, Fe, Co)O3-Δ and BaySr1-yCoO3-Δ redox system for thermochemical energy storage at high temperatures, Energy. 171 (2019) 971–980. doi:10.1016/j.energy.2019.01.081.

[86] A.H. McDaniel, A. Ambrosini, E.N. Coker, J.E. Miller, W.C. Chueh, R. O'Hayre, J. Tong, Nonstoichiometric perovskite oxides for solar thermochemical H2 and CO production, Energy Procedia. 49 (2014) 2009–2018. doi:10.1016/j.egypro.2014.03.213.

[87] B.J. Hare, D. Maiti, S. Ramani, A.E. Ramos, V.R. Bhethanabotla, J.N. Kuhn, Thermochemical conversion of carbon dioxide by reverse water-gas shift chemical looping using supported perovskite oxides, Catal. Today. 323 (2019) 225–232. doi:10.1016/j.cattod.2018.06.002.

[88] K.J. Albrecht, G.S. Jackson, R.J. Braun, Evaluating thermodynamic performance limits of thermochemical energy storage subsystems using reactive perovskite oxide particles for concentrating solar power, Sol. Energy. 167 (2018) 179–193. doi:10.1016/j.solener.2018.03.078.

[89] S.M. Babiniec, E.N. Coker, J.E. Miller, A. Ambrosini, Doped calcium manganites for advanced high-temperature thermochemical energy storage, Int. J. Energy Res. 40 (2016) 280–284. doi:10.1002/er.3467.

[90] J.E. Miller, S.M. Babiniec, E.N. Coker, P.G. Loutzenhiser, E.B. Stechel, A. Ambrosini, Modified Calcium Manganites for Thermochemical Energy Storage Applications, Front. Energy Res. 10 (2022) 1–18. doi:10.3389/fenrg.2022.774099.

[91] I. Ermanoski, Cascading pressure thermal reduction for efficient solar fuel production, Int. J. Hydrogen Energy. 39 (2014) 13114–13117. doi:10.1016/j.ijhydene.2014.06.143.

[92] S. Brendelberger, H. von Storch, B. Bulfin, C. Sattler, Vacuum pumping options for

application in solar thermochemical redox cycles – Assessment of mechanical-, jet- and thermochemical pumping systems, Sol. Energy. 141 (2017) 91–102. doi:10.1016/j.solener.2016.11.023.

[93] S. Brendelberger, M. Roeb, M. Lange, C. Sattler, Counter flow sweep gas demand for the ceria redox cycle, Sol. Energy. 122 (2015) 1011–1022. doi:10.1016/j.solener.2015.10.036.

[94] B. Bulfin, F. Call, M. Lange, O. Lübben, C. Sattler, R. Pitz-Paal, I. V. Shvets, Thermodynamics of CeO 2 Thermochemical Fuel Production, Energy & Fuels. 29 (2015) 1001–1009. doi:10.1021/ef5019912.

[95] L. Imponenti, K.J. Albrecht, R. Kharait, M.D. Sanders, G.S. Jackson, Redox cycles with doped calcium manganites for thermochemical energy storage to 1000 °C, Appl. Energy. 230 (2018) 1–18. doi:10.1016/j.apenergy.2018.08.044.

[96] A.J. Schrader, G.L. Schieber, A. Ambrosini, P.G. Loutzenhiser, Experimental demonstration of a 5kW th granular-flow reactor for solar thermochemical energy storage with aluminum-doped calcium manganite particles, n.d.

[97] A. de la Calle, I. Ermanoski, E.B. Stechel, Towards chemical equilibrium in thermochemical water splitting. Part 1: Thermal reduction, Int. J. Hydrogen Energy. (2021). doi:10.1016/j.ijhydene.2021.07.167.

[98] M. Sandlin, S.I. Abdel-Khalik, A study of granular flow through horizontal wire mesh screens for concentrated solar power particle heating receiver applications – Part I: Experimental studies and numerical model development, Sol. Energy. 169 (2018) 1–10. doi:10.1016/j.solener.2018.03.036.

[99] M. Sandlin, S.I. Abdel-Khalik, A study of granular flow through horizontal wire mesh screens for concentrated solar power particle heating receiver applications – Part II: Parametric model predictions, Sol. Energy. 174 (2018) 1252–1262. doi:10.1016/j.solener.2018.04.042.

[100] Z. Ma, G. Glatzmaier, M. Mehos, Fluidized bed technology for concentrating solar power with thermal energy storage, J. Sol. Energy Eng. Trans. ASME. 136 (2014) 1–9. doi:10.1115/1.4027262.

[101] C.K. Ho, A review of high-temperature particle receivers for concentrating solar power, Appl. Therm. Eng. 109 (2016) 958–969. doi:10.1016/j.applthermaleng.2016.04.103.

[102] C. Agrafiotis, D. Thomey, L. de Oliveira, N. Overbeck, V.K. Thanda, M. Roeb, C. Sattler, Solar energy conversion and storage through sulphur-based thermochemical cycles implemented on centrifugal particle receivers, AIP Conf. Proc. 2303 (2020). doi:10.1063/5.0028766.

[103] S. Bellan, E. Alonso, F. Gomez-Garcia, C. Perez-Rabago, J. Gonzalez-Aguilar, M. Romero, Thermal performance of lab-scale solar reactor designed for kinetics analysis

at high radiation fluxes, Chem. Eng. Sci. 101 (2013) 81–89. doi:10.1016/j.ces.2013.06.033.

[104] D. Kunii, T. Chisaki, Introduction, in: D. Kunii, T. Chisaki (Eds.), Rotary React. Eng., Elsevier, Amsterdam, 2008: pp. 1–10. doi:10.1016/B978-044453026-4.50003-7.

[105] Y.A. Cengel, A.J. Ghajar, Heat and Mass Transfer: Fundamentals & Applications, Fifth Edit, McGraw-Hill Education, 2015.

[106] H. Chen, Y. Chen, H.T. Hsieh, N. Siegel, Computational fluid dynamics modeling of gas-particle flow within a solid-particle solar receiver, J. Sol. Energy Eng. Trans. ASME. 129 (2007) 160–170. doi:10.1115/1.2716418.

[107] T. Tan, Y. Chen, Review of study on solid particle solar receivers, Renew. Sustain. Energy Rev. 14 (2010) 265–276. doi:10.1016/j.rser.2009.05.012.

[108] T. Tan, Y. Chen, Z. Chen, N. Siegel, G.J. Kolb, Wind effect on the performance of solid particle solar receivers with and without the protection of an aerowindow, Sol. Energy. 83 (2009) 1815–1827. doi:10.1016/j.solener.2009.06.014.

[109] N.P. Siegel, C.K. Ho, S.S. Khalsa, G.J. Kolb, Development and evaluation of a prototype solid particle receiver: On-sun testing and model validation, J. Sol. Energy Eng. Trans. ASME. 132 (2010) 0210081–0210088. doi:10.1115/1.4001146.

[110] C.K. Ho, J.M. Christian, J. Yellowhair, N. Siegel, S. Jeter, M. Golob, S.I. Abdel-Khalik, C. Nguyen, H. Al-Ansary, On-sun testing of an advanced falling particle receiver system, AIP Conf. Proc. 1734 (2016). doi:10.1063/1.4949074.

[111] P.K. Falcone, J.E. Noring, J.M. Hruby, Assessment of a solid particle receiver for a high temperature solar central receiver system, Energy Procedia. 49 (1985) 398–407.

[112] H. Al-Ansary, A. El-Leathy, Z. Al-Suhaibani, S. Al-Zahrani, S. Jeter, S. Abdel-Khalik, D. Sadowski, M. Golob, Solid particle receiver with porous structure for flow regulation and enhancement of heat transfer, US 2013/0068217 A1, 2013.

[113] T. Lee, S. Lim, S. Shin, D.L. Sadowski, S.I. Abdel-Khalik, S.M. Jeter, H. Al-Ansary, Numerical simulation of particulate flow in interconnected porous media for central particle-heating receiver applications, Sol. Energy. 113 (2015) 14–24. doi:10.1016/j.solener.2014.12.017.

[114] G. Flamant, D. Hernandez, C. Bonet, J.P. Traverse, Experimental aspects of the thermochemical conversion of solar energy; Decarbonation of CaCO3, Sol. Energy. 24 (1980) 385–395. doi:10.1016/0038-092X(80)90301-1.

[115] W. Wu, L. Amsbeck, R. Buck, R. Uhlig, R. Ritz-Paal, Proof of concept test of a centrifugal particle receiver, Energy Procedia. 49 (2014) 560–568. doi:10.1016/j.egypro.2014.03.060.

[116] W. Wu, L. Amsbeck, R. Buck, N. Waibel, P. Langner, R. Pitz-Paal, On the influence

of rotation on thermal convection in a rotating cavity for solar receiver applications, Appl. Therm. Eng. 70 (2014) 694–704. doi:10.1016/j.applthermaleng.2014.03.059.

[117] W. Wu, R. Uhlig, R. Buck, R. Pitz-Paal, Numerical simulation of a centrifugal particle receiver for high-temperature concentrating solar applications, Numer. Heat Transf. Part A Appl. 68 (2015) 133–149. doi:10.1080/10407782.2014.977144.

[118] F. Bai, Y. Zhang, X. Zhang, F. Wang, Y. Wang, Z. Wang, Thermal performance of a quartz tube solid particle air receiver, Energy Procedia. 49 (2014) 284–294. doi:10.1016/j.egypro.2014.03.031.

[119] F. Wang, F. Bai, Z. Wang, X. Zhang, Numerical Simulation of Quartz Tube Solid Particle Air Receiver, Energy Procedia. 69 (2015) 573–582. doi:10.1016/j.egypro.2015.03.066.

[120] Y. Zhang, F. Bai, X. Zhang, F. Wang, Z. Wang, Experimental Study of a Single Quartz Tube Solid Particle Air Receiver, Energy Procedia. 69 (2015) 600–607. doi:10.1016/j.egypro.2015.03.069.

[121] J. Martinek, Z. Ma, Granular flow and heat-transfer study in a near-blackbody enclosed particle receiver, J. Sol. Energy Eng. Trans. ASME. 137 (2015) 1–9. doi:10.1115/1.4030970.

[122] G. Flamant, D. Gauthier, H. Benoit, J.L. Sans, B. Boissière, R. Ansart, M. Hemati, A new heat transfer fluid for concentrating solar systems: Particle flow in tubes, Energy Procedia. 49 (2014) 617–626. doi:10.1016/j.egypro.2014.03.067.

[123] G. Flamant, D. Gauthier, H. Benoit, J.L. Sans, R. Garcia, B. Boissière, R. Ansart, M. Hemati, Dense suspension of solid particles as a new heat transfer fluid for concentrated solar thermal plants: On-sun proof of concept, Chem. Eng. Sci. 102 (2013) 567–576. doi:10.1016/j.ces.2013.08.051.

[124] A.J. Carrillo, J. Moya, A. Bayón, P. Jana, V.A. De La Peña O'Shea, M. Romero, J. Gonzalez-Aguilar, D.P. Serrano, P. Pizarro, J.M. Coronado, Thermochemical energy storage at high temperature via redox cycles of Mn and Co oxides: Pure oxides versus mixed ones, Sol. Energy Mater. Sol. Cells. 123 (2014) 47–57. doi:10.1016/j.solmat.2013.12.018.

[125] J.O. Hill, I.G. Worsley, L.G. Hepler, Thermochemistry and oxidation potentials of vanadium, niobium, and tantalum, Chem. Rev. 71 (1971) 127–137. doi:10.1021/cr60269a006.

[126] A. Ambrosini, T. Garino, T.M. Nenoff, Synthesis and characterization of the double-substituted perovskites LaxSr1-xCo1-yMnyO3-δ for use in high-temperature oxygen separations, Solid State Ionics. 177 (2006) 2275–2279. doi:10.1016/j.ssi.2006.05.023.

[127] S.M. Babiniec, E.N. Coker, J.E. Miller, A. Ambrosini, Investigation of LaxSr1-xCoyM1-yO3-δ (M=Mn, Fe) perovskite materials as thermochemical energy storage media, Sol. Energy. 118 (2015) 451–459. doi:10.1016/j.solener.2015.05.040.

[128] I. Ermanoski, E.B. Stechel, Thermally-driven adsorption/desorption cycle for oxygen pumping in thermochemical fuel production, Sol. Energy. 198 (2020) 578–585. doi:10.1016/j.solener.2020.01.050.

[129] I. Ermanoski, J.E. Miller, M.D. Allendorf, Efficiency maximization in solar-Thermochemical fuel production: Challenging the concept of isothermal water splitting, Phys. Chem. Chem. Phys. 16 (2014) 8418–8427. doi:10.1039/c4cp00978a.

[130] B. Bulfin, A.J. Lowe, K.A. Keogh, B.E. Murphy, O. Lübben, S.A. Krasnikov, I. V. Shvets, Analytical model of CeO2 oxidation and reduction, J. Phys. Chem. C. 117 (2013) 24129–24137. doi:10.1021/jp406578z.

[131] C. Ho, J. Christian, D. Gill, A. Moya, S. Jeter, S. Abdel-Khalik, D. Sadowski, N. Siegel, H. Al-Ansary, L. Amsbeck, B. Gobereit, R. Buck, Technology advancements for next generation falling particle receivers, Energy Procedia. 49 (2014) 398–407. doi:10.1016/j.egypro.2014.03.043.

[132] M. Röger, L. Amsbeck, B. Gobereit, R. Buck, Face-down solid particle receiver using recirculation, J. Sol. Energy Eng. Trans. ASME. 133 (2011) 1–8. doi:10.1115/1.4004269.

[133] C.K. Ho, J.M. Christian, J. Yellowhair, K. Armijo, W.J. Kolb, S. Jeter, M. Golob, C. Nguyen, Performance Evaluation of a High-Temperature Falling Particle Receiver, in: Vol. 1 Biofuels, Hydrog. Syngas, Altern. Fuels; CHP Hybrid Power Energy Syst. Conc. Sol. Power; Energy Storage; Environ. Econ. Policy Considerations Adv. Energy Syst. Geothermal, Ocean. Emerg. E, American Society of Mechanical Engineers, 2016: pp. 1–30. doi:10.1115/ES2016-59238.

[134] G. Xiao, K. Guo, M. Ni, Z. Luo, K. Cen, Optical and thermal performance of a high-temperature spiral solar particle receiver, Sol. Energy. 109 (2014) 200–213. doi:10.1016/j.solener.2014.08.037.

[135] M. Hillert, The compound energy formalism, J. Alloys Compd. 320 (2001) 161–176. doi:10.1016/S0925-8388(00)01481-X.

[136] I.H. Bell, J. Wronski, S. Quoilin, V. Lemort, Pure and Pseudo-pure Fluid Thermophysical Property Evaluation and the Open-Source Thermophysical Property Library CoolProp, Ind. Eng. Chem. Res. 53 (2014) 2498–2508. doi:10.1021/ie4033999.

[137] R. Ghotkar, E.B. Stechel, I. Ermanoski, R.J. Milcarek, Hybrid Fuel Cell—Supercritical CO2 Brayton Cycle for CO2 Sequestration-Ready Combined Heat and Power, Energies. 13 (2020) 5043. doi:10.3390/en13195043.

[138] C. Murphy, Y. Sun, W. Cole, G. Maclaurin, C. Turchi, M. Mehos, C. Murphy, Y. Sun, W. Cole, G. Maclaurin, C. Turchi, M. Mehos, The Potential Role of Concentrating Solar Power within the Context of DOE's 2030 Solar Cost Targets, NREL Tech. Rep. - NREL/TP-6A20-71912. (2019) 137. https://www.nrel.gov/docs/fy19osti/71912.pdf.

[139] M. Sandlin, S.I. Abdel-Khalik, A study of granular flow through horizontal wire mesh screens for concentrated solar power particle heating receiver applications – Part I: Experimental studies and numerical model development, Sol. Energy. 169 (2018) 1–10. doi:10.1016/j.solener.2018.03.036.

[140] C.N.R. Rao, S. Dey, Solar thermochemical splitting of water to generate hydrogen, Proc. Natl. Acad. Sci. U. S. A. 114 (2017) 13385–13393. doi:10.1073/pnas.1700104114.

[141] M.L. Bell, K. Ebisu, R.D. Peng, J. Walker, J.M. Samet, S.L. Zeger, F. Dominici, Seasonal and Regional Short-term Effects of Fine Particles on Hospital Admissions in 202 US Counties, 1999–2005, Am. J. Epidemiol. 168 (2008) 1301–1310. doi:10.1093/aje/kwn252.

[142] High Heat Hardbrick FireBrick Straights 2.5", (n.d.). https://www.sheffield-pottery.com/LVHHD-HIGH-HEAT-Fire-Brick-STRAIGHTS-2-5-p/lvhhd.htm#:~:text=Our Price%3A %242.89&text=All questions are subject to store approval.

APPENDIX A

NUMERICAL VERIFICATION OF THE ANALYTICAL MASS TRANSFER MODEL

The numerical model developed in Chapter 5 to estimate the steady state pO_2 distribution in the reactor concepts, can be used to verify the trends shown in Figure 26. The only changes made here, compared to the previous analysis on MO_x-N_2 mixing, is setting $\theta = 0$ (applicable for both the ZFR and the OFR) and reducing the number of steps to 2. Four layers of 100 μm particles serve as static O_2 sources. Inlet pO_2 of N_2 is 10 Pa and the $pO_{2,surf}$ at 1^{st} and 2^{nd} step is 100 Pa and 1000 Pa, respectively. The objective of this analysis is to verify some of the predictions of the analytical diffusion model under these conditions which represent the typical steady state reactor operation. According to Figure 60, $pO_{2,out}$ and t_{BL} both decrease with increase in vN_2 at constant d_{part}. Furthermore, $pO_{2,out} = pO_{2,surf}$ when $t_{BL} = \frac{1}{2}$(distance between consecutive particles), which is equivalent to the assumption $a_{cell} = 2t_{BL}+d_{part}$ used in the analytical diffusion model. Figure 60 verifies several trends seen in Figure 26 and adds more confidence in the analytical mass transfer model results.

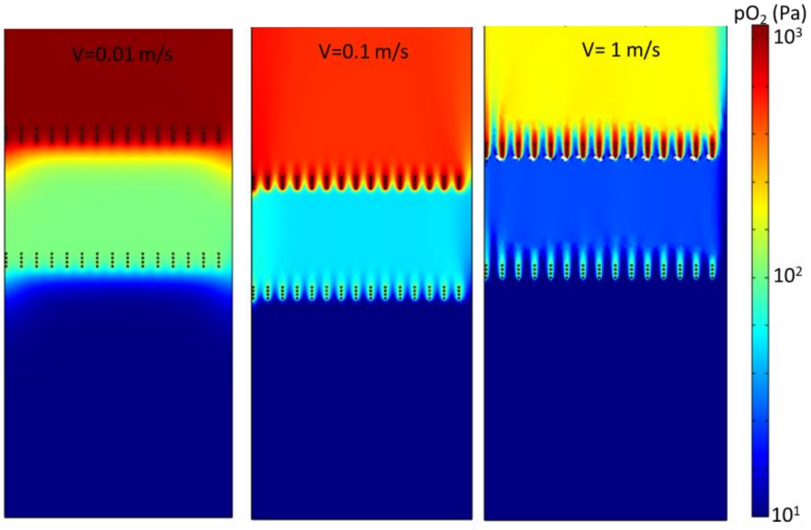

Figure 60. Steady State pO_2 Distribution Under Different Inlet vN_2 With Two Reaction Steps. Model Results Are Representative Of Both the OFR And the ZFR.

APPENDIX B

NUMERICAL MODEL CONSIDERATIONS FOR THE COARSE MESH SIZING

The ZFR incorporates inclined meshes arranged within a rectangular U-channel. These meshes are inclined at a slight angle (15°). The mesh used is particle-opaque with an opening diameter of 50 µm and a 43% open area. This choice is made to accommodate particles in the size range of 50 µm to 150 µm. To facilitate particle movement, a 2 mm gap is present at the end of each mesh, guiding particles along the mesh. Additionally, coarser meshes with an opening diameter of 180 µm and a 31% open area are used to prevent the compression of the inert gas, which could otherwise create jets in the gaps. Given the rectangular channel configuration of the ZFR, a central rectangular cross-section is utilized as a 2-D representation of the meshes in the CFD (Computational Fluid Dynamics) flow model. Figure 61 displays the geometry and boundary conditions for the CFD model of the ZFR.

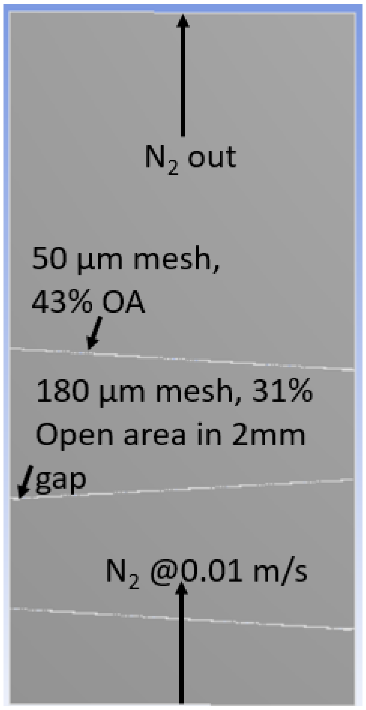

Figure 61. Cross Section Of the 2-D Cross Sectional Geometry Used In the ZFR CFD Model

The mesh for the CFD model is shown in Figure 62. This mesh contains 157389 nodes and 155110 nodes with an average element quality of 0.7.

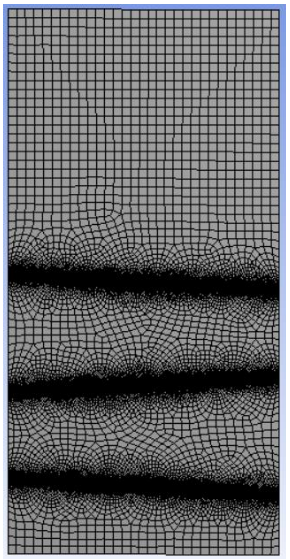

Figure 62. Mesh Used In the ZFR CFD Model

A k-ε turbulence model is used to visualize the flow pattern in the model. Similar to IFR, contours of v_{N2} are enough to understand the particle-gas interaction in the model since the particle-particle interaction are ignored similar to IFR CFD analysis. The velocity streamlines for ZFR. Figure 63a shows that using the 180 μm mesh helps in distributing the supplied gas evenly throughout the reactor. On the other hand, adding a coarser mesh (300 μm) increases the open area of the end gap thereby squeezing more gas through this opening (Figure 63b). Removing the coarse mesh completely, squeezes a large portion of the gas through the 2 mm end gap affecting the laminar flow assumption. This squeezing could cause particle fluidization as well as an inefficient use of the supplied inert gas. The fine and coarse meshes must be sized such that the total area open to the gas flow, in the coarse mesh section must be equal in the fine mesh section. This will ensure a uniform gas flow rate along the reactor cross section.

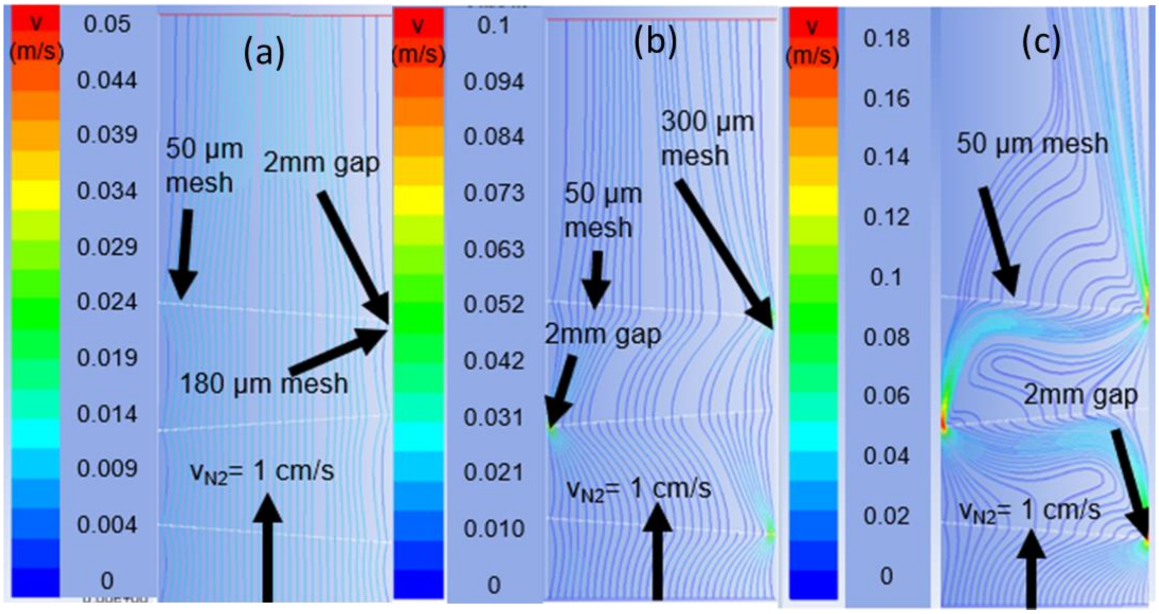

Figure 63. N_2 Velocity Streamlines From the ZFR CFD Model For 50 µm Fine Mesh, vN_2 = 1 cm/s and A Coarse Mesh With a_{mesh} = (a) 180 µm, (b) 300 µm and (c) No Coarse Mesh In The 2 mm End Gap